

## AN ABSTRACT OF THE DISSERTATION OF

Arielle L Clauser for the degree of Doctor of Philosophy in Materials Science presented on March 19 2021.

Title: Platinum Nanoparticles in Transition Alumina: An Atomic Resolution Study of Interfaces

Abstract approved:

---

Melissa K. Santala

The phases of transition alumina are scientifically interesting due to their high specific surface area, favorable acid/ base characteristics, and chemical and hydrothermal stability which make this metallic oxide a prime candidate for use as a support for metallic nanoparticles (NPs) in heterocatalysis. Interactions at alumina/Pt interfaces are important for catalysis, but poorly understood due to the microstructural complexity of transition alumina and challenges associated with characterization of interfaces. The goal of this work is to compare experimentally determined atomic-level structural information from aberration-corrected scanning transmission electron microscopy (STEM) with density functional theory (DFT) based structural models and quantum mechanical STEM image simulations to characterize the chemistry and atomic-level structure of Pt/ $\gamma$  and Pt/ $\theta$ -interfaces.

In this work, dense transition-alumina layers are formed using high-energy ion implantation to amorphize near surface layers of  $\alpha$ -alumina wafers which are then recrystallized into the desire alumina form via thermal annealing. Self-implanted

alumina wafers are used to determine viability of producing oriented  $\gamma$ -alumina layers. Pt-implanted alumina is processed to produce Pt/ $\gamma$ -alumina and Pt/ $\theta$ -alumina interfaces in the form of faceted Pt NPs embedded in alumina. Conventional transmission electron microscopy (TEM), image-corrected TEM, and x-ray diffraction (XRD) are used to characterize the microstructure of  $\gamma$ -alumina and Pt/transition-alumina systems. The recrystallization of amorphized alumina occurs epitaxially to the  $\alpha$ -alumina with parallel alignment close-packed O planes of  $(0006)_\alpha$  and  $(111)_\gamma$  or  $(\bar{2}01)_\theta$ . Faceted Pt NPs possess a  $(111)_{Pt}||[(111)_\gamma; [1\bar{1}0]_\gamma]||[1\bar{1}0]_{Pt}$  orientation in  $\gamma$ -alumina and a  $(\bar{2}01)_\theta ||[(111)_{Pt}; [132]_\theta]|| [1\bar{1}0]_{Pt}$  orientation in  $\theta$ -alumina. In both systems the NPs are primarily bound by  $\{111\}$ Pt facets. Probe-corrected STEM was used to collect atomic resolution images of the faceted interfaces to determine the structure and chemical terminations of  $\gamma$ - and  $\theta$ -alumina at the interfaces. This is facilitated by comparison of the experimental images to quantum mechanical scanning (S)TEM simulations of density functional theory (DFT) based model structures. Oxygen termination of the alumina is found to be the dominant chemical termination for both  $(111)_\gamma||[(111)_{Pt}]$  and  $(\bar{2}01)_\theta||[(111)_{Pt}]$  interfaces.

©Copyright by Arielle L. Clauser  
March 19, 2021  
All Rights Reserved

Platinum Nanoparticles in Transition Alumina: An Atomic Resolution Study of  
Interfaces

by  
Arielle L. Clauser

A DISSERTATION

submitted to

Oregon State University

in partial fulfillment of  
the requirements for the  
degree of

Doctor of Philosophy

Presented March 19, 2021  
Commencement June 2021

Doctor of Philosophy dissertation of Arielle L. Clauser presented on March 19, 2021

APPROVED:

---

Major Professor, representing Materials Science

---

Associate Dean for Graduate Programs, College of Engineering

---

Dean of the Graduate School

I understand that my dissertation will become part of the permanent collection of Oregon State University libraries. My signature below authorizes release of my dissertation to any reader upon request.

---

Arielle L. Clauser, Author

## ACKNOWLEDGEMENTS

This work was supported, in part, by the National Science Foundation through Grant No. 1610507. TEM was performed at the Oregon State University Electron Microscope Facility which is supported by NSF MRI Grant No. 1040588 , the Murdock Charitable Trust, and the Oregon Nanoscience and Micro-Technologies Institute. Aberration-corrected TEM imaging was performed at the at the Center for Advanced Materials Characterization at the University of Oregon. Probe-corrected STEM was performed at the National Center for Electron Microscopy (NCEM) part of the Molecular Foundry at Lawrence Berkeley National Laboratory (LBNL). Work at the Molecular Foundry was supported by the Office of Science, Office of Basic Energy Sciences, of the US Department of Energy (contract no. DE-AC02–05CH11231). A.L.C. acknowledges funding from the Department of Energy SCGSR program which supported travel to LBNL.

## CONTRIBUTION OF AUTHORS

Zachary D. McClure assisted with collecting x-ray diffraction (XRD) data in Chapter 2 and Chapter 3. Dr. Jim Ciston assisted in scheduling and experimentation at the National Center for Electron Microscopy (NCEM). During this visit the atomic resolution images used in Chapter 4 were collected. He assisted in editing Chapter 3 and facilitated the remote TEAM 1 session used to collect atomic resolution images in Chapter 5. Dr. Raquel Giulian performed the Rutherford backscatter spectroscopy and ion implantation of the materials used and analyzed in Chapters 3, 4 and 5. Dr. Colin Ophus was the overseeing advisor during a summer appointment at NCEM. He specializes in computation transmission electron microscopy and developed the Prismatic algorithm used in Chapters 4 and 5. He aided in editing Chapter 3. Dr. Kofi Oware Sarfo completed the DFT experiments referenced in Chapters 3, 4 and 5. He was a primary collaborator in the implanted alumina project and provided the computational thermodynamic calculations. Dr. Líney Árnadóttir assisted in writing and editing Chapters 3, 4, and 5. She was Dr. Oware-Sarfo's thesis advisor and provided guidance and insight for computational studies. Dr. Melissa K. Santala assisted in editing all chapters and, she collected XRD and conventional TEM data used in Chapter 5.

## TABLE OF CONTENTS

	<u>Page</u>
1. Chapter 1 Introduction .....	1
1.1. Historical Overview of Catalysis .....	1
1.1.1. Metal/Metal Oxide Catalyst Systems.....	2
1.1.2. Alumina as a catalyst .....	3
1.1.3. Noble Metals supported by Alumina .....	4
1.1.4. Platinum Interfaces with $\alpha$ -alumina .....	5
1.2. The Formation and Structures of Aluminum Oxide Polymorphs .....	7
1.3. Overview of Select Methods of Studying Catalysts .....	11
1.3.1. Model Catalyst Systems.....	11
1.3.2. Ion Implantation.....	11
1.3.3. Transmission Electron Microscopy as a Tool for Studying Heterocatalysts .....	12
Chapter 1 References .....	18
2. Preliminary Experimental Studies .....	24
2.1. Formation of dense $\gamma$ -alumina via “self-implantation” .....	24
2.1.1. Processing and characterization of self-implanted sapphire: Methods.	25
2.1.2. Self-implanted sapphire: Results and discussion.....	26
2.2. Preliminary characterization studies on Pt-implanted sapphire .....	32
2.2.1. Processing and characterization of Pt-implanted sapphire: Methods ...	32
2.2.2. Preliminary characterization of Pt-implanted sapphire: Results.....	34
Chapter 2 References .....	42
3. Orientation and morphology of Pt nanoparticles in $\gamma$ -alumina processed <i>via</i> ion implantation and thermal annealing .....	43
4. Characterization of the atomic -level structure of (111) Pt/ $\gamma$ -alumina interfaces.....	60
4.1. Introduction .....	61
4.1.1. Producing NPs in $\gamma$ -alumina via ion implantation .....	63
4.1.2. Structural Models of $\gamma$ -alumina.....	64
4.1.3. Structural Model of the Pt/ $\gamma$ -alumina Interface .....	66

## TABLE OF CONTENTS (Continued)

4.2.	Experimental .....	67
4.3.	Results and discussion.....	69
4.3.1.	Comparison of $\gamma$ -alumina to Smrčok and Zhou models .....	70
4.3.2.	The structure of the (111) Pt/ $\gamma$ -alumina interface .....	75
4.4.	Conclusions .....	79
	Chapter 4 References .....	80
5.	Structure of interfaces of Pt nanoparticles in $\theta$ -alumina.....	84
5.1.	Introduction .....	85
5.2.	Methods.....	86
5.2.1.	Experimental methods .....	86
5.2.2.	Image simulation.....	88
5.3.	Results and Discussion.....	89
5.4.	Conclusions .....	98
	Chapter 5 References .....	99
6.	Concluding Remarks.....	101
6.1.	Viability of the Processing Method.....	101
6.2.	Platinum Nanoparticles in $\gamma$ -Alumina .....	102
6.3.	Platinum Nanoparticles in $\theta$ -Alumina.....	102
	Common Bibliography .....	104
A.	Appendix .....	114

## LIST OF FIGURES

<u>Figure</u>	<u>Page</u>
Figure 1 A cubic spinel crystal structure present in different variants of alumina .....	9
Figure 2 A [110] <sub>γ</sub> equivalent zone-axis view of a δ-alumina crystal structure.....	9
Figure 3 Monoclinic θ-alumina .....	10
Figure 4 XRD patterns for “self-implanted” sapphire wafers .....	27
Figure 5 Bright field TEM image of self-implanted sapphire .....	30
Figure 6 TEM BF and DF image pair with [110] and [211] diffraction patterns .....	31
Figure 7 XRD patterns for alumina wafers implanted with a Pt dose of $1 \times 10^{16} \text{ cm}^{-2}$	35
Figure 8 Pt-implanted layer with a dose of $1 \times 10^{16} \text{ Pt/cm}^2$ TEM image and [110] <sub>Pt</sub> diffraction pattern.....	37
Figure 9 XRD patterns for wafers implanted with $5 \times 10^{16} \text{ Pt}^+/\text{cm}^2$ .....	39
Figure 10 BF TEM images collected during and after in situ TEM annealing of $5 \times 10^{16} \text{ Pt cm}^{-2}$ .....	41
Figure 11 RBS spectrum of $1 \times 10^{17} \text{ Pt/cm}^2$ wafers .....	48
Figure 12 XRD of sapphire wafers implanted with $1 \times 10^{17} \text{ Pt cm}^{-2}$ .....	49
Figure 13 BF TEM images of the $5 \times 10^{16} \text{ Pt/cm}^2$ wafer and simulated diffraction patterns.....	51
Figure 14 Aberration-corrected phase-contrast HRTEM .....	54
Figure 15 The Zhou and Smrcok models for γ-alumina .....	65
Figure 16 HRSTEM HAADF and BF image of γ-Al <sub>2</sub> O <sub>3</sub> .....	69
Figure 17 A HAADF and BF image pair of a unit cell of alumina from Figure 16 with γ-alumina simulations. ....	71
Figure 18 Drift-corrected (a) BF and (b) HAADF pair of Pt NPs in γ-alumina viewed on a [211] zone axis. ....	72
Figure 19 Detail from Figure 18 with DFT models and simulations.....	73

## LIST OF FIGURES (Continued)

Figure 20 Drift-corrected HAADF and BF STEM image pair of a Pt NP in $\gamma$ -alumina with DFT model and simulated interface imaged along the $[110]_{\text{Pt}}$ zone-axis.....	76
Figure 21 Detail of a (111)Pt/ $\gamma$ -alumina interface boxed in Figure 18. ....	77
Figure 22 RBS data of implanted wafers. The inset gives the Pt distribution as a function of depth from the sapphire surface. ....	87
Figure 23 XRD data for (a) as-implanted sapphire and after (b) 250h at 1000°C in air. ....	90
Figure 24 Bright field TEM images of the sapphire in cross-section.....	92
Figure 25 Drift-corrected STEM (a) HAADF and (b) BF image pair of Pt NPs in $\theta$ -alumina.....	93
Figure 26 Simulated BF STEM images of the Pt- $\theta$ interface with overlaid DFT models.....	94
Figure 27 Detail from the Figure 25 HAADF image with analysis and DFT simulations.....	95

## LIST OF TABLES

<u>Table</u>	<u>Page</u>
Table 1 Transition phases of alumina $\theta$ and $\delta$ share planes with similar d-spacings..	36
Table 2 Atomic positions for the Zhou and Smrčok defected spinel $\gamma$ -alumina models. .....	66
Table 3 Pt and $\gamma$ -Al <sub>2</sub> O <sub>3</sub> lattice parameters .....	74
Table 4 Measured distance between the terminating layer of Pt and the layer of O closest to the interface for the five DFT models and the experimental images .....	97

## LIST OF APPENDICES

<u>Appendix</u>	<u>Page</u>
A. Appendix .....	114

## DEDICATION

I dedicate this monument to my own ego to my parents, and younger brother.

They are my tether to stability and lightheartedness when my world becomes stormy and small.

I am grateful to the people who drank with me, fed me, and cared for me during graduate school, I hope their presence continues to enrich my life for many years to come. I am eagerly looking forward to seeing the distant friends my heart has longed for and resuming postponed plans.

To my advisor in undergrad and my advisor today.

And finally to my three black beasts.

## **1. Chapter 1 Introduction**

### **1.1. Historical Overview of Catalysis**

Improving the rate, selectivity, and efficiency at which chemical reactions occur saves time, money and reduces environmental costs. Increasing the rate of chemical reactions through the addition of an unconsumed agent is called catalysis. This phenomenon is harnessed and applied to finely filter exhausts [1], manufacture petrochemicals [2], synthetic materials [3], convert biomass feedstocks [4], and synthesize fine chemicals [5]. Good catalyst systems are determined by the selectivity, activity, and stability relative to the catalyzed reaction. Improved catalyst systems can reduce the cost of technology by lowering the energetic barrier to important reactions. Increased accessibility to new technologies, including solar cells [6] and cleaner fuels [7], are a direct consequence of reducing energetic requirements for reactions with catalysts.

The term catalysis was proposed by Jöns Jakob Berzelius in 1835. Berzelius described catalysts as having “the property of exerting on other bodies an action which is very different from chemical affinity. By means of this action, they produce decomposition in bodies and form new compounds into the composition of which they do not enter.”[8] This implies a substance that assisted or improved a reaction without being consumed or reacted in the meantime. Before Paul Sabatier won the 1912 Nobel Prize in chemistry for proving the principle with Ni and hydrogenated ethylene, Wilhelm Ostwald had proposed that catalysts did not induce a reaction but accelerated a reaction through the formation of intermediate compounds [9]. These principles have become the frame work for a number of modern processes including the conversion of CO<sub>2</sub> to methanol [10]. This process can be used to recycle problematic CO<sub>2</sub> emissions and assist in global depollution. However catalysts see use in even the most mundane aspects of human consumption for example, nickel catalysts are used during the production of margarine and other

high fat dairy products as ethane adsorbates [11], underscoring the motivation for study of these useful systems.

### 1.1.1. Metal/Metal Oxide Catalyst Systems

Metal nanoparticles (NPs) supported by metal oxides are commonly used in hetero-catalysis. Metal oxide catalyst systems were popular as early as the mid-1950s and used in oxidation and acid/base reactions. Efficient catalyst systems reduce the overall energy required for a reaction to occur. A fundamental understanding of the structure of these systems and the relationship to their catalytic functions is required to improve these systems and produce more efficient heterocatalysts that reduce overall energy costs respectively. Metal oxides such as  $\text{Al}_2\text{O}_3$ ,  $\text{TiO}_2$ , and  $\text{SiO}_2$  are often used in catalysis to support catalytically-active metal nanoparticles. Transition metals, specifically, noble metals are resistant to chemical degradation at high temperatures and are known for their catalytic abilities. Metal-oxide-supported noble metals, such as Pt on alumina, are good candidates for catalyst processes that require high temperature functionality in corrosive environments.

Both selectivity and reactivity depend on the size of catalyst particles [12]. Ultimately interactions between the oxide support and metallic nanoparticles at the interface can impact the rate of catalysis and the efficacy of the system. Morphology, orientation, composition, and interfacial interaction all contribute to how well these systems perform. Porous metal oxides like the metastable transition aluminas have large surface areas covered in catalytically active sites that have made them widely used in catalysis and their study fundamentally interesting to the scientists who research catalysis [13]. Strong-metal support interactions (SMSI) can change the catalytic ability of metal-oxide supported metallic nanoparticles by changing the occupancy of atoms in the d-orbital [14, 15]. Both the metal oxide supports, and the supported NPs possess

catalytic sites and are combined to create heterocatalyst systems that hybridize and improves specific reaction reactivity through SMSIs.

### 1.1.2. Alumina as a catalyst

The 1960 work produced by Pines and Haag, *Alumina: Catalyst and Support, its intrinsic Acidity and Catalytic activity* [16], found that calcined alumina hydrate heated at an optimum temperature of 600 to 700°C exhibited better catalytic activity than alumina hydrate treated at higher and lower temperatures in fact they found “the low isomerization activity of the alumina calcined at 400 and 900°C is not due to a smaller surface area...the qualitative change of the alumina surface on thermal treatment appears to be much more pronounced than a change in area.” This work proposed that this improved surface behavior was attributed to a change in Lewis acid sites on the surface of alumina leading the way to understanding that there must be some type of structural evolution that must occur to the alumina hydrate in this temperature range that facilitates the increase of these sites. Work has been done since, showing that alumina developed within these temperature ranges do possess structures that lead to increased Lewis acid site formation [2, 17].

Alumina is widely recognized as a catalyst and catalyst support due to certain intrinsic properties. Gamma-alumina in particular has seen heavy use as a support for noble metal NPs because of increased surface area that occurs during dehydration combined with and increased number of Lewis acid sites [18]. These sites are responsible for one of the most important intrinsic properties of alumina catalysts, intrinsic acidity. The dehydroxlation of OH<sup>-</sup> saturated alumina ores that occurs during calcination allows exposed surfaces to become uncoordinated and unsaturated, thus creating an electron pair acceptor sites [19]. The feasibility of pure alumina as a catalyst has been studied with respect to the isomerization and dehydration of organic compounds such as cyclohexene and alcohols like butanol [16]. It was determined that a large

number of high acid sites were present on pure alumina. The intrinsic porosity associated with transition alumina results in a large surface area material dense with Lewis acid sites, which is also useful in catalytic systems.

### 1.1.3. Noble Metals supported by Alumina

Noble metals, specifically those in the Pt metal catalyst group (Pt, Pd, Rh), are used in automotive catalytic converters. Gamma-alumina is used as support for these metals that transform  $\text{N}_2\text{O}$  and CO into safe gases through oxidation. Catalytic activity of alumina can be fine-tuned by adding supported metallic nanoparticles [20]. This creates a strong interaction that causes the suppression of certain catalytic abilities like the adsorption of  $\text{H}_2$  and CO with the addition of Group VIII noble metals. The cause of SMSI have been attributed to two possible atomic interactions the first involved metal-metal bonding of a supported NP ( $\text{Pt}^{4+}$ ,  $\text{Ir}^{4+}$ ,  $\text{Co}^{4+}$ ) that involves covalent sharing of  $d$  orbitals the second explanation for SMSI is related to the formation of intermetallic compounds like  $\text{TiPt}_3$  that possess Lewis-acid-base sites [14]. Pt NP supported by  $\gamma$ -alumina is an important system that has found use in the petrochemical industry. Hydrogenation/dehydrogenation of hydrocarbons occurs in the presence of Pt NPs, this combined with the rearrangement of the hydrocarbon skeleton due to the high number of acid sites present in alumina make the Pt-alumina system fundamentally important to study [21].

In this work, the catalytic efficiency will not be measured, but the atomic-level structure of planar interfaces of Pt with two transition alumina polymorphs ( $\gamma$ -alumina and  $\theta$ -alumina) are investigated using a model system of Pt nanoparticles embedded in dense layers of  $\gamma$  and  $\theta$  transition alumina.

#### 1.1.4. Platinum Interfaces with $\alpha$ -alumina

This work focuses on the characterization of the interfacial relationships and atomic level structure of interfaces between Pt and  $\gamma$ - and  $\theta$ -alumina, for which there is limited experimental work. Interfaces between Pt and  $\alpha$ -alumina have been studied more extensively in terms of interfacial energies, orientation relationships, and atomic structure and provide added context for this work. In the 1970s, McLean and Hondros measured the interfacial energies in the Pt/Al<sub>2</sub>O<sub>3</sub> system at 1400°C; Pt\Al<sub>2</sub>O<sub>3</sub> and Al<sub>2</sub>O<sub>3</sub>\air had surface energies of  $10.5 \times 10^{13}$  and  $7.7 \times 10^{13}$  J m<sup>-2</sup>, respectively [22]. In the early 1990s, diffusion bonded interfaces between sapphire and polycrystalline  $\alpha$ -alumina with Pt were studied by DeGraef *et al.* to determine the bonding and structure of the interfaces [23]. They found the lattice mismatch for Pt and Al<sub>2</sub>O<sub>3</sub> was 0.98% down the [100]<sub>Pt</sub> and 1.06% down the perpendicular [010]<sub>Pt</sub> direction for the  $[\bar{1}010]_{\alpha} \parallel [110]_{Pt}$ ;  $(1\bar{2}10)_{\alpha} \parallel (011)_{Pt}$  orientation relationship. They also found amorphous regions of Al<sub>2</sub>O<sub>3</sub> occasionally occurred locally in areas where the epitaxial fit was imperfect. The epitaxial relationship between Pt films grown on (0001) sapphire were studied using electron microscopy by Ramanathan *et al.*, and the primary orientation relationship possessed two variants rotated 60° around the [111]<sub>Pt</sub> zone axis in a  $(111)_{Pt} \parallel (0001)_{\alpha}$ ;  $[110]_{Pt} \parallel [\bar{1}010]_{\alpha}$  orientation relationship [24]. The presence of extensive twinning between these two rotational variants results in a mazed-bicrystal structure of the Pt film. The  $(111)_{Pt} \parallel (0001)_{\alpha}$ ;  $[110]_{Pt} \parallel [\bar{1}010]_{\alpha}$  orientation relationship has also been observed in coherent Pt precipitates formed using Pt<sup>+</sup> ion implanted  $\alpha$ -alumina [25-27].

Both experimental and theoretical studies have been performed Pt on (0001)  $\alpha$ -alumina. The (0001) plane is a thermodynamically stable surface [28] and is part of the equilibrium (Wulff) shape [29, 30] of  $\alpha$ -alumina and it may have different surface terminations. A study

combining density functional theory (DFT) and aberration-corrected transmission electron microscopy of a  $(111)_{\text{Pt}}\parallel(0001)_{\alpha}$  interface found that the DFT model with an oxygen-terminated interface provided the best fit to experimental data. In a DFT study on CO adsorption on Pt supported by  $\alpha$ -alumina by Yourdshahyan et al., the (0001) surfaces were modeled as Al-Al-O, Al-O-Al or O-Al-Al terminated [31] where the first atom indicated is closest to the Pt atoms at the interface. The O-Al-Al and Al-Al-O surfaces are polar and they found the non-polar Al-O-Al surface is the most energetically favored. However, they also found the surface most energetically favored with respect to adsorption of single Pt atoms was oxygen terminated.

The amount of CO adsorption that occurs in a catalytic Pt/ $\alpha$ -alumina system can be attributed to the interfacial structure of Pt on alumina. Three types of adsorption for CO on Pt and alumina have been reported [32] these are the Griffith mode, Pauling mode, and Yeager mode. In the Griffith mode  $\text{O}_2$  molecules are present above metal cations. The Pauling mode adsorb through a single Pt-O bond and the Yeager mode occurs when  $\text{O}_2$  bridges over two Pt atoms with O-O bonds parallel to Pt-Pt bonds and is also known as ‘bridge mode.’ DFT studies have been performed to determine that for  $\alpha\text{-Al}_2\text{O}_3$  Pt surfaces that Yeager and bridge mode adsorption are preferred with respect to activation of  $\text{O}_2$  molecules [33]. This 1:1 relationship for Pt and O in  $\alpha$ -alumina relates to the available bonding sites on clean alumina surfaces. On an  $\text{Al}_2\text{O}_3$  surfaces that is clean of residual hydroxyls groups, Lewis acid sites are present at electron poor Al atoms, Lewis base sites are electron rich sites that are present at O atoms, Pt, Pd and Ni all require a bonding sites on the surface and facilitate electron sharing between Lewis acid and base sites when bonded to alumina [34, 35].

The Pt/ $\gamma\text{-Al}_2\text{O}_3$ / $\alpha\text{-Al}_2\text{O}_3$  system has been studied using atomic force microscopy as route to understand the structure of Pt on high-surface-area  $\gamma$ -alumina by Okumura *et al.* In this work,

Pt was vacuum deposited on the surface of  $\gamma$ -alumina developed from  $\text{Al}^+$  and  $\text{O}^-$  ion implanted  $\alpha$ -alumina. Annealing at  $800^\circ\text{C}$  in oxidative atmospheres caused the thin films of Pt deposited on  $\gamma$ -alumina to be converted to finely dispersed particles whereas Pt on  $\alpha$ -alumina formed larger faceted islands [36], highlighting an effective difference between  $\alpha$ - and  $\gamma$ -alumina phases in the support of Pt NPs.

## 1.2. The Formation and Structures of Aluminum Oxide Polymorphs

Alpha-alumina ( $\alpha\text{-Al}_2\text{O}_3$ ), or corundum, is the most thermodynamically stable phase of  $\text{Al}_2\text{O}_3$ , yet there are several metastable phases of  $\text{Al}_2\text{O}_3$  that can develop depending on the precursor utilized. Linus Pauling and Sterling Hendricks first proposed a rhombohedral crystal lattice  $D_{3d}^6$ , or  $R\bar{3}C$ , for corundum in 1925 using spectrographic Laue methods [37]. The structure of  $\alpha$ -alumina may be considered as the hexagonal close packing of oxygen planes that comprise the  $(0001)_\alpha$  plane that is interlayered with octahedrally coordinated  $\text{Al}^{3+}$  ions. In order to maintain stoichiometry so that only  $2/3$  of available octahedral interstices are occupied [38]. Alpha-alumina has seen many uses as a technical ceramic due to its excellent thermal properties; its melting point can range 2310 K to 2329 K.

There are many metastable, transition alumina forms. In this work,  $\gamma$ -alumina and  $\theta$  alumina are formed by thermally annealing amorphized  $\alpha$ -alumina. Amorphous alumina passes through an irreversible series of metastable phases at increasing temperatures before reaching the ultimate stable  $\alpha\text{-Al}_2\text{O}_3$  phase. The phase transition path is as follows; amorphous  $\text{Al}_2\text{O}_3 \rightarrow \gamma\text{-Al}_2\text{O}_3 \rightarrow \delta\text{-Al}_2\text{O}_3 \rightarrow \theta\text{-Al}_2\text{O}_3 \rightarrow \alpha\text{-Al}_2\text{O}_3$ . The  $\gamma$ - through  $\alpha$ -alumina part of the series are observed during the calcination of boehmite ore [39]. Alpha-alumina often forms at temperatures between  $1100\text{-}1150^\circ\text{C}$ ,  $\theta$ -alumina forms at  $1000\text{-}1100^\circ\text{C}$  [40]. There is some ambiguity concerning the temperatures at which the  $\delta$  and  $\gamma$  phases form, with some reporting  $\delta$ -alumina forming above

700-900°C and  $\gamma$ -alumina forming between 500-800°C [41]. In addition, these transition phases can exist concurrently.

Gamma-alumina is the first phase of alumina that forms during the dehydration of boehmite ore, as well as during the thermal annealing of amorphous  $\text{Al}_2\text{O}_3$ . Several structural models have been proposed for  $\gamma$ -alumina. The Zhou and Snyder model for  $\gamma$ -alumina was proposed in 1991 and is a cubic spinel type unit cell ( $Fd\bar{3}m$ ) where a sublattice made of oxygen atoms is imperfectly occupied by aluminum in spinel and “quasi-spinel” positions [42]. The highest occupancy positions of an alumina cubic spinel sublattice is shown in Figure 1 down the [111], [110], and [211] zone-axis. Paglia and coworkers used well-crystalline boehmite calcined between 500-900°C and found a  $P\bar{4}m2$  tetragonal structure for  $\gamma$ -alumina with a cation coordination of ~69%  $\text{Al}_o$  and ~31%  $\text{Al}_t$  [43]. More recently Smrčok proposed a refined version of the Zhou and Snyder spinel unit cell, but proposed the partial occupancy of non-spinel sites [44]. Yet other models of  $\gamma$ -alumina are still widely cited and used for surface density functional theory (DFT) calculations which have small unit cells with no partial Al occupancy, such as the Digne model [45] which is based on a separate molecular dynamics study by Krokidis which investigated intermediary structures during the collapse of boehmite ore during calcination [46]. The Krokidis structure determines an equilibrium structure for  $\gamma$ -alumina to have 25-31%  $\text{Al}_t$  with vacant Al sites placed at random in the unit cell.

Delta-alumina is the next polymorph of alumina in the transformation series after  $\gamma$ -alumina. It has been extensively studied by Kovarik et al., who have proposed a complex structure for  $\delta$ -alumina consisting of the intergrowth of small structural units. One variant of Kovarik's  $\delta$  structure is shown in Figure 2. In this work 37.5% of Al present were found in tetrahedral sites ( $\text{Al}_t$ ) and

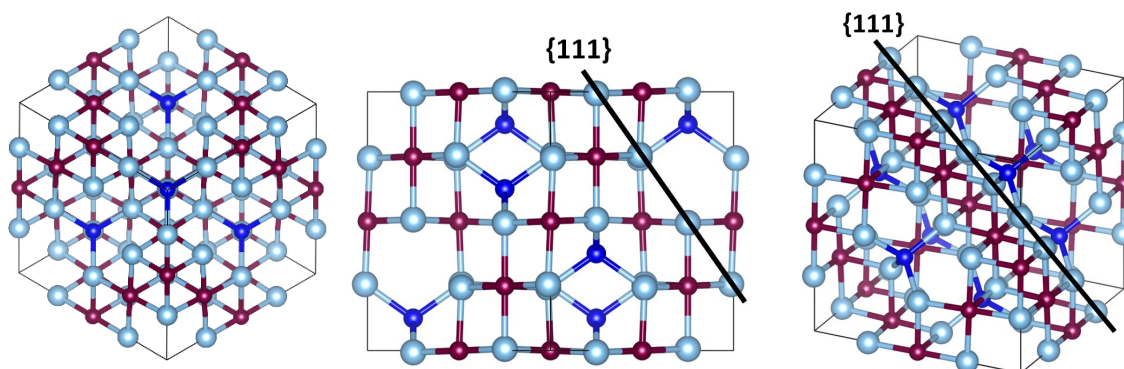


Figure 1 A cubic spinel crystal structure present in different variants of alumina

*Light blue balls are associated with an oxygen cubic sublattice, dark blue balls are tetrahedral aluminum positions, and dark red balls are octahedral aluminum viewed down the (left)  $[111]$  (middle)  $[110]$  (right)  $[211]$  zone axis*

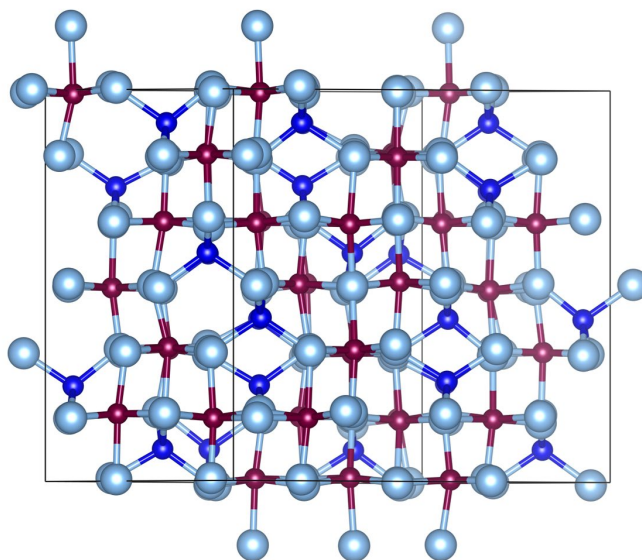


Figure 2 A  $[110]_{\gamma}$  equivalent zone-axis view of a  $\delta$ -alumina crystal structure

*Kovarik's variant 2  $\delta$ -alumina structure where light blue balls are oxygen, dark blue balls are tetrahedral aluminum positions, and dark red balls are octahedral aluminum*

the other 62.5% were found in octahedral positions ( $Al_o$ ) [47]. Previous work on  $\gamma$ -alumina proposes tetragonal and orthorhombic crystal structures with a  $P2_12_12_1$  or  $P2_12_12$  space groups, primarily constructed of a supercell of three spinel blocks [48].

Theta alumina, shown in Figure 3, is the final metastable phase in the amorphous to  $\alpha$ - $Al_2O_3$  transformation path and most stable of the transition alumina ( $\gamma$ ,  $\delta$ , and  $\theta$ ). There is more agreement on the structure of  $\theta$ -alumina than upon  $\gamma$  or  $\delta$ -alumina. The observation of this phase dates back to as early as 1950 [49]. It is monoclinic and 50% of the  $Al^{3+}$  is located in tetrahedral sites, the other 50% is located in octahedral positions [42].

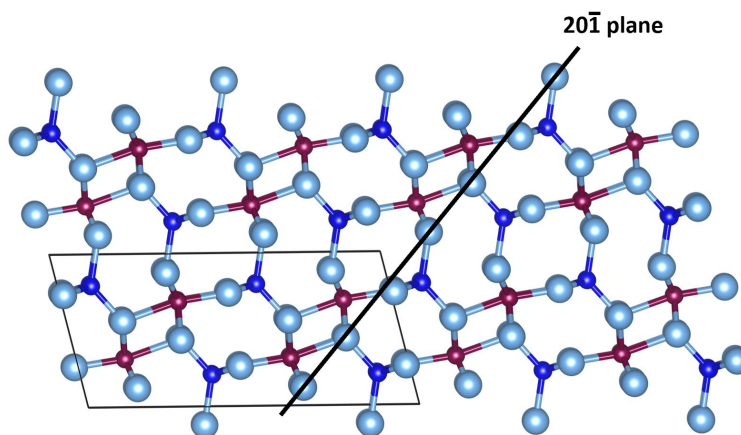


Figure 3 Monoclinic  $\theta$ -alumina

*Reppelin's model for  $\theta$ -alumina, the  $(20\bar{1})$  plane is the crystallographic successor to cubic close packed  $(111)_\gamma$  planes in the  $\gamma \rightarrow \alpha$  phase transition. Light blue balls are associated with an oxygen sublattice, dark blue balls are tetrahedral aluminum positions, and dark red balls are octahedral aluminum*

## **1.3. Overview of Select Methods of Studying Catalysts**

### **1.3.1. Model Catalyst Systems**

Model catalyst systems have been used to study hetero catalyst materials that are difficult to normally study [50]. Single crystal metals have been used as model catalyst systems [51, 52], however single metal models fail to address the complexity of heterocatalyst systems where the support as well as the single crystal metal interact and both contribute to catalyst functionality. Model systems of oxide-supported metals have been developed in order to study the catalytic behavior of small clusters of metal particles with respect to size and morphology in the forms of oxide films with metal clusters deposited on the surface [53]. Oxides implanted with metal ions offer a novel way to study the interfacial relationships between metal NPs and oxides that are robust under high energy examination such as that which occurs using transmission electron microscopy [54-56]. A model system processed using ion implantation of Pt into single crystal alumina and further processed by thermal annealing is used in this work and the processing is described in Chapters 3 and 4, but some general background on ion implantation and characterization of heterocatalysts is given in the following sections.

### **1.3.2. Ion Implantation**

Ion implantation was first developed during the 1940s when scientists working on the Manhattan project were developing a mass analyzer to separate uranium isotopes during the development of the first atomic bombs [57]. Ion implantation of enables doping of virtually any element and modification of surface properties of crystalline wafers. This process is a non-equilibrium method and can be used to generate material systems that are not naturally occurring or common. This includes the creation of nanorods [58], Si implanted light emitting diodes, super conducting nanocrystals as well as traditional semiconductor chip devices [59].

Ion implantation works by using an ion source to initially produce ions that are accelerated electrostatically to an increased energy level, these are then accelerated through a separation magnet. The accelerated ions are used to bombard and modify a target material. The depth at which ions can penetrate the implanted substrate and the accumulated implantation damage is dependent on the mass of the dopant ion, energy used to accelerate the dopant ion, the mass of the target atoms, the angle of implantation, the crystallographic orientation of the target, and the temperature at which the implantation occurs. Software, called the Stopping and Range of Ions in Matter (SRIM) [60], has been developed by J. Zeigler and coworkers to estimate the depth and distribution different implantation parameters will create. Ion implantation causes damage to the target when ions collide with the crystalline structure and cause point defects. Enough of this type of damage can cause the complete amorphization of a surface or sub-surface layer of the target.

Amorphized layers of material can be annealed to create epitaxially grown structures with respect to the underlying crystalline material. This type of processing method has been used in  $\text{SrTiO}_3$  and  $\text{CaTiO}_3$  studies [56]. The epitaxial growth of  $\gamma$ -alumina from amorphized single crystal  $\alpha$ -alumina was shown to be possible in work by Yu, using x-ray diffraction and TEM to study the effect of ion beam bombardment [61]. This method was shown to be effective in promoting the growth of epitaxial transition alumina from  $\alpha$ -alumina and allowed the microstructure to be tuned by varying implantation parameters, including precipitation metallic NPs [62].

### 1.3.3. Transmission Electron Microscopy as a Tool for Studying Heterocatalysts

Transmission electron microscopy (TEM) enables a spatially resolved characterization of hetero-catalysts, including the atomic resolution structural characterization of the interfaces.

TEM imaging studies are complementary to spectroscopic characterization techniques which only provide a partial picture with respect to atomic structure and an averaged view of structural data. X-ray spectroscopy (XPS) and nuclear magnetic resonance provide data that characterize atomic interactions of the entire material system that is probed. In situ XPS has been used to study the surface properties of many catalytic systems [63]. Pt-Re NPs supported on carbon have been probed with XPS to determine the reaction pathways and subsequent acid site concentration and strength for this system [64]. Other x-ray-based spectroscopic methods have seen a wide application with respect to studying catalytic systems including x-ray absorption (XAS) and x-ray absorption near-edge spectroscopy (XANES) [65]. These spectroscopic methods are valuable tools used to understand averaged structural information, but the TEM studies presented here provide important complementary information including imaging of interfaces in revealing their spatially resolved structure. Electron energy loss spectroscopy (EELS) has also been used to probe the bonding states of Pt on alumina [66] and of Fe Fischer Tropsch catalysts [67], but this work focuses on structural characterization through atomic resolution imaging.

TEM can be used to collect electron diffraction patterns, as well atomic resolution phase contrast images. High-resolution TEM (HRTEM) images are phase-contrast images, generated using parallel illumination of the specimen with coherent source of electrons. The Phase-contrast results from local phase shifts of the electron wavefunction as the electron beam is transmitted through the sample. Constructive and destructive interference of the electrons scattered by a weak phase object (in this case an electron transparent sample) creates an image of the sample on a detector. The intensities of these types of atomic-resolution images are not directly interpretable (meaning positions occupied by atoms do not have a consistent relative intensity) due changes in observed intensity with defocus of the objective,  $\Delta f$ , and specimen thickness. The

result is that high or low intensity regions do not necessarily correspond to the positions of atomic columns or the absence of material, but rather are areas of constructive waveform interference.

The contrast transfer function,  $H(\mathbf{u})$  is used to describe how the specimen is translated into the image in real space through the reciprocal lattice vector  $\mathbf{u}$  [68].

$$H(\mathbf{u}) = A(\mathbf{u})E(\mathbf{u})B(\mathbf{u})$$

where  $A(\mathbf{u})$  is the aperture function which refers to the limits imposed on spatial frequencies greater than the objective aperture,  $E(\mathbf{u})$  is the envelope function which limits frequencies similar to  $A(\mathbf{u})$  due to restrictions imposed by the electron lens itself, and  $B(\mathbf{u})$  is the aberration function, which describes the aberrations of the TEM's objective lens.

The aberration function may be written as:

$$B(\mathbf{u}) = \exp(i\chi(\mathbf{u}))$$

where  $\chi(\mathbf{u})$  relates the image dependence on  $\Delta f$ , electron wavelength  $\lambda$ , and  $C_s$ , the spherical aberration of the objective lens with is an innate imperfection of electron lenses. Minimizing  $C_s$  using aberration correction improves the resolution achievable during imaging, it is important to recognize that defocus still plays a large part in the resolution of the image even under perfect imaging ( $C_s=0$ ) conditions

$$\chi(\mathbf{u}) = \pi\Delta f\lambda u^2 + \frac{1}{2}\pi\Delta C_s\lambda^3 u^4$$

The phase of the electron wave may be backed out using exit wave reconstructions from a series of images of known defocus. The weak phase object approximation (WPOA) simplifies the specimen function  $f(x,y)$  to

$$f(x, y) = 1 - i\sigma V_t(x, y)$$

where  $\sigma$  is the interaction constant and  $V_t$  is the projected potential of electrons passing through the specimen. One implication is that only the imaginary portion of  $B(\mathbf{u})$  contributes to intensity and thus  $B(\mathbf{u})$  can be simplified into

$$B(\mathbf{u}) = 2 \sin \chi(\mathbf{u})$$

The WPOA relates the total intensity of a collected HRTEM image to  $H(\mathbf{u})$  through the transfer function,  $T(\mathbf{u})$ :

$$T(\mathbf{u}) = 2A(\mathbf{u})\sin\chi(\mathbf{u})$$

The transfer function is important because it demonstrates that there is an oscillating relationship between spatial frequencies transmitted and  $\chi(\mathbf{u})$ . This shows that defocus ( $\Delta f$ ) and phase aberration ( $C_s$ ) cause a phase shift of  $\pm \frac{\pi}{2}$ . Under specific defocus values the beam is shifted  $+\frac{\pi}{2}$  and atoms appear bright, when the beam is shifted  $-\frac{\pi}{2}$  atoms appear dark. This means that identification of atomic positions of atomic resolution HRTEM images must be done using processes like exit-wave reconstructions, in order to determine the phase of the electrons exiting the specimen.

Another approach to imaging materials at atomic resolution is by scanning TEM (STEM), in which a fine probe is rastered over a sample, similar to scanning electron microscopy (SEM). In STEM, the ultimate resolution depends on the size and quality of the electron probe, rather than on the performance of the objective lens. High angle annular dark field (HAADF) STEM images are directly interpretable, in that areas of higher intensity correspond to regions where the electron probe interacted with more mass while transiting the sample, and it can also achieve atomic resolution. In HAADF imaging, local image intensity is determined by the number of electrons that have scattered at high angles due to Rutherford scattering from the sample. Rutherford scattering occurs when charged particles are elastically scattered due to

Coulombic interactions with an atom. The scattering cross section ( $\sigma_R$ ) derived by Ernest Rutherford for high angle scattering from the nucleus where  $\theta$  is the scattered angle,  $\Omega$  is the solid angle,  $e$  is the electron charge,  $Z$  is the atomic number,  $E_0$  is electron energy in eV, and  $\epsilon_0$  is the dielectric constant, is given by [68]

$$\sigma_R(\theta) = \frac{e^4 Z^2}{16(4\pi\epsilon_0 E_0)^2} \frac{d\Omega}{\sin^4 \frac{\theta}{2}}$$

When electrons are scattered mainly through interaction with atoms' electron clouds low angle coherent scattering occurs, when electrons interact with the electron nucleus they are scattered at high angles incoherently. This interaction that causes high angle scattering is the reason contrast of HAADF images is element dependent.

As the name suggests, HAADF detectors are annular in shape with a cut out in the center. Only electrons scattered at wide angles (75 - 150 mrad) are collected, but low angle Bragg diffracted electrons are not collected. This means there is little contrast arising from constructive and destructive interference due to coherent Bragg scattering to complicate interpretation of intensities in the images. HAADF imaging is sometimes referred to as "Z-contrast" imaging due to intensities of the images being related to atomic number and number of atoms in the atomic column. STEM image simulation can still be used to aid in the interpretation of STEM images and validate experimental conclusions by revealing the origin of intensities observed experimentally. Image simulation provides a way to quantify STEM images and can be used to calculate information about the number of atoms present in atomically resolved columns and deal with issues that can be caused by dynamical scattering [69-71]. The multislice algorithm is a widely used simulation treatment for TEM images that was initially proposed by Cowley and Moodie [72]. In chapters 5 and 6, a faster, modern approach was used to simulate STEM images

under a variety of conditions using Prismatic, an image simulation software developed by C. Ophus [73].

There have been many studies of  $\gamma$ -alumina and  $\gamma$ -alumina-supported metal NPs using TEM and STEM, e.g. [74-76]. Neutron magnetic resonance studies combined with STEM and DFT have shown that the “the O-terminated PtO (101) structure on the surface of (100)  $\gamma$ -Al<sub>2</sub>O<sub>3</sub> was the most thermodynamically stable structure” of the various structure they simulated to optimize tetragonal PtO [77]. More recently, infrared spectroscopy, TEM and NMR were used to characterize the active sites and relationships between Pt and  $\gamma$ -alumina, coordinatively unsaturated Al<sup>+3</sup>O<sub>5</sub> sites were found to be responsible for nitrogen activation in  $\gamma$ -Al<sub>2</sub>O<sub>3</sub> [78]. Currently, there is still ambiguity with respect to the structure of interfacial Pt particles on transition alumina. The following studies seek to determine the characteristic atomic structure of Pt interfaces of NPs in transition alumina using a combination of advanced transmission electron microscopy techniques and modern image simulations of DFT-calculated interfacial structures for a model material system of Pt-implanted alumina.

The DFT models of different chemical terminations associated with the experimentally determined orientation relationships of  $\gamma$ -alumina and platinum [79] and  $\theta$ -alumina and platinum were calculated by collaborator, Kofi Oware Sarfo, advised by Líney Árnadóttir. As described in detail in Chapter 3, the  $\gamma$ -alumina/Pt interfacial relationship that was observed, (111)<sub>Pt</sub>|| (111) <sub>$\gamma$</sub>  [110]<sub>Pt</sub>|| [110] <sub>$\gamma$</sub>  was used to guide DFT calculations.

## Chapter 1 References

- [1] J. Kašpar, P. Fornasiero, and N. Hickey, "Automotive catalytic converters: current status and some perspectives," *Catalysis Today*, vol. 77, no. 4, pp. 419-449, 2003, doi: 10.1016/s0920-5861(02)00384-x.
- [2] M. A. Alabdullah *et al.*, "A Viewpoint on the Refinery of the Future: Catalyst and Process Challenges," *ACS Catalysis*, vol. 10, no. 15, pp. 8131-8140, 2020, doi: 10.1021/acscatal.0c02209.
- [3] N. Kornienko, J. Z. Zhang, K. K. Sakimoto, P. Yang, and E. Reisner, "Interfacing nature's catalytic machinery with synthetic materials for semi-artificial photosynthesis," *Nature Nanotechnology*, vol. 13, no. 10, pp. 890-899, 2018, doi: 10.1038/s41565-018-0251-7.
- [4] T. Letcher, *Comprehensive Renewable Energy*. London, UNITED KINGDOM: Elsevier, 2012.
- [5] H. Cong and J. A. Porco, "Chemical Synthesis of Complex Molecules Using Nanoparticle Catalysis," *ACS Catalysis*, vol. 2, no. 1, pp. 65-70, 2012, doi: 10.1021/cs200495s.
- [6] V. Balzani, G. Pacchioni, M. Prato, and A. Zecchina, "Solar-driven chemistry: towards new catalytic solutions for a sustainable world," *Rendiconti Lincei. Scienze Fisiche e Naturali*, vol. 30, no. 3, pp. 443-452, 2019, doi: 10.1007/s12210-019-00836-2.
- [7] T. G. Kaufmann, A. Kaldor, G. F. Stuntz, M. C. Kerby, and L. L. Ansell, "Catalysis science and technology for cleaner transportation fuels," *Catalysis Today*, vol. 62, no. 1, pp. 77-90, 2000, doi: 10.1016/s0920-5861(00)00410-7.
- [8] J. J. Berzelius, "Årsberöttelsen om framsteg i fysik och kemi," *Royal Swedish Academy of Sciences*, 1835.
- [9] X.-M. Hu and K. Daasbjerg, "Molecular catalyst converts carbon dioxide to methanol," *Nature*, vol. 575, no. 7784, pp. 598-599, 2019, doi: 10.1038/d41586-019-03563-8.
- [10] J. Wisniak, "The History of Catalysis. From the Beginning to Nobel Prizes," *Educación Química*, vol. 21, no. 1, pp. 60-69, 2010, doi: 10.1016/s0187-893x(18)30074-0.
- [11] E. Lodyga-Chruscinska, A. Sykula-Zajac, and D. Olejnik, "Determination of nickel in Polish brands of margarines," *Food Addit Contam Part B Surveill*, vol. 5, no. 4, pp. 251-4, 2012, doi: 10.1080/19393210.2012.702287.
- [12] M. Arai, "Particle size effect and structure sensitivity in catalysis by supported metal catalysts," *JOURNAL OF CHEMICAL ENGINEERING OF JAPAN*, vol. 30, no. 6, pp. 1123-1125, 1997, doi: 10.1252/jcej.30.1123.
- [13] B. K. Singh, S. Lee, and K. Na, "An overview on metal-related catalysts: metal oxides, nanoporous metals and supported metal nanoparticles on metal organic frameworks and zeolites," *Rare Metals*, vol. 39, no. 7, pp. 751-766, 2019, doi: 10.1007/s12598-019-01205-6.
- [14] S. J. Tauster and S. C. Fung, "Strong Metal-Support Interactions: Occurrence among the binary oxides of group IIA-VB," *Journal of Catalysis*, vol. 55, pp. 29-35, 1978.
- [15] S. J. Tauster, S. C. Fung, and R. L. Garten, "Strong Metal-Support Interactions. Group 8 Noble Metals Supported on TiO<sub>2</sub>," *Journal of the American Chemical Society*, vol. 100, pp. 170-175, 1978.
- [16] H. Pines and W. O. Haag, "Alumina: Catalyst and Support. I. Alumina, its Intrinsic Acidity and Catalytic Activity 1," vol. 82, no. 10, pp. 2471-2483, 1960, doi: 10.1021/ja01495a021.

- [17] H. Knozinger, "Acid and Basic Properties of Aluminas in relation to their properties as catalysts and supports," *Catalysis by Acids and Bases*, pp. 111-125, 1985.
- [18] G. R. Jenness, M. A. Christiansen, S. Caratzoulas, D. G. Vlachos, and R. J. Gorte, "Site-Dependent Lewis Acidity of  $\gamma$ -Al<sub>2</sub>O<sub>3</sub> and Its Impact on Ethanol Dehydration and Etherification," *The Journal of Physical Chemistry C*, vol. 118, no. 24, pp. 12899-12907, 2014, doi: 10.1021/jp5028349.
- [19] D. Coster, A. L. Blumenfeld, and J. J. Fripiat, "Lewis Acid Sites and Surface Aluminum in Aluminas and Zeolites: A High-Resolution NMR Study," *The Journal of Physical Chemistry*, vol. 98, no. 24, pp. 6201-6211, 1994, doi: 10.1021/j100075a024.
- [20] Y. Kanda, T. Kobayashi, Y. Uemichi, and M. Sugioka, "Catalytic Performance of Noble Metals Supported on Alumina-modified Silica Gel for Hydrodesulfurization Reaction," *Journal of Japan Petroleum Institute*, vol. 2, pp. 49-56, 2006.
- [21] E. Yang *et al.*, "Acidic effect of porous alumina as supports for Pt nanoparticle catalysts in n-hexane reforming," *Catalysis Science & Technology*, vol. 8, no. 13, pp. 3295-3303, 2018, doi: 10.1039/c8cy00776d.
- [22] M. McLean and E. D. Hondros, "A study of grain boundary grooving at the platinum/alumina interface," *Journal of Materials Science*, vol. 6, pp. 19-24, 1971.
- [23] M. D. Graef, B. J. Dalgleish, M. R. Turner, and A. G. Evans, "Interfaces between alumina and platinum: Structure, bonding and fracture resistance," *Acta metall. mater.*, vol. 40, pp. S333-S344, 1992.
- [24] S. Ramanathan, B. M. Clemens, P. C. McIntyre, and U. Dahmen, "Microstructural study of epitaxial platinum and Permalloy/platinum films grown on (0001) sapphire," *Philosophical Magazine A*, vol. 81, 8, pp. 2073-2094, 2001, doi: 10.1080/0141861001002898.
- [25] E. Alves, R. C. Da Silva, O. Conde, M. F. Da Silva, and J. C. Soares, "Formation of coherent precipitates of platinum in sapphire," *Nuclear Instruments and Methods in Physics Research Section B: Beam Interactions with Materials and Atoms*, vol. 148, no. 1-4, pp. 1049-1053, 1999, doi: 10.1016/s0168-583x(98)00706-x.
- [26] C. Ophus, M. K. Santala, M. Asta, and V. Radmilovic, "Structure and phase transitions at the interface between  $\alpha$ -Al<sub>2</sub>O<sub>3</sub> and Pt," *Journal of Physics: Condensed Matter*, vol. 25, p. 232202, 2013.
- [27] M. K. Santala, "On Orientation Relationships and Morphologies of Platinum Precipitates in Sapphire," Ph.D., Materials Science and Engineering, University of California, Berkeley, 2009.
- [28] X.-G. Wang, A. Chaka, and M. Scheffler, "Effect of the Environment on  $\alpha$ -Al<sub>2</sub>O<sub>3</sub>(0001) Surface Structures," *Physical Review Letters*, vol. 84, no. 16, pp. 3650-3653, 2000, doi: 10.1103/physrevlett.84.3650.
- [29] J. H. Choi *et al.*, "Equilibrium shape of internal cavities in sapphire," *Journal of the American Ceramic Society*, Article vol. 80, no. 1, pp. 62-68, Jan 1997. [Online]. Available: <Go to ISI>://A1997WF89600007
- [30] M. Kitayama and A. M. Glaeser, "The Wulff shape of alumina. III. Undoped alumina," *Journal Of The American Ceramic Society*, vol. 85, no. 3, pp. 611-22, 2002.
- [31] Y. Yourdshahyan, V. R. Cooper, A. M. Kolpak, and A. M. Rappe, "Catalytic behavior at the nanoscale: CO adsorption on Al<sub>2</sub>O<sub>3</sub> supported Pt clusters," in *SPIE*, Bellingham, WA, T. Lian, Ed., 2003, vol. 5223, pp. 223-231.
- [32] P. N. Ross and J. Lipkowski, *Electrocatalysis*. Wiley-VCH, Inc., 1998, p. 199.

- [33] S. Nigam and C. Majumder, "ORR viability of alumina-supported platinum nanocluster: exploring oxidation behaviour by DFT," *Phys Chem Chem Phys*, vol. 19, no. 29, pp. 19308-19315, Jul 26 2017, doi: 10.1039/c7cp04029f.
- [34] L. G. V. Briquet, C. R. A. Catlow, and S. A. French, "Platinum Group Metal Adsorption on Clean and Hydroxylated Corundum Surfaces," *The Journal of Physical Chemistry C*, vol. 113, no. 38, pp. 16747-16756, 2009, doi: 10.1021/jp904217b.
- [35] L. G. V. Briquet, C. R. A. Catlow, and S. A. French, "Comparison of the Adsorption of Ni, Pd, and Pt on the (0001) Surface of  $\alpha$ -Alumina," *The Journal of Physical Chemistry C*, vol. 112, no. 48, pp. 18948-18954, 2008, doi: 10.1021/jp803540r.
- [36] K. Okumura, S.-a. Hyodo, and S. Noda, "Growth of Pt Crystallites supported on gamma-Al<sub>2</sub>O<sub>3</sub> studied by atomic force microscopy," *Journal of Physical Chemistry B*, no. 105, pp. 8345-8349, 2001.
- [37] L. Pauling and S. B. Hendricks, "The Crystal Structures of Hematite and Corundum," *Journal of the American Chemical Society*, vol. 47, no. 3, pp. 781-790, 1925, doi: 10.1021/ja01680a027.
- [38] K. Wefers and C. Misra, "Oxides and Hydroxides of Aluminum," *Alcoa Technical Paper*, vol. 19, 1987.
- [39] H. Ginsberg, W. Huttig, and G. Strunk-Lichtenberg, "Über den Einfluß des Ausgangsmaterials auf die beim thermischen Abbau bzw. Umbau von Aluminiumhydroxyden entstehenden kristallinen Formen. I. Die kristallinen Formen des Thermischen Abbaues der  $\gamma$ -Aluminiumhydroxyde," *Zeitschrift für Anorganische Chemie*, vol. 293, no. 1-2, pp. 33-46, 1957.
- [40] P. Eklund, M. Sridharan, G. Singh, and J. Böttiger, "Thermal Stability and Phase Transformations of  $\gamma$ -Amorphous-Al<sub>2</sub>O<sub>3</sub> Thin Films," *Plasma Processes and Polymers*, vol. 6, no. S1, pp. S907-S911, 2009, doi: 10.1002/ppap.200932301.
- [41] C. Wolverton and K. C. Hass, "Phase stability and structure of spinel-based transition aluminas," vol. 63, no. 2, 2000, doi: 10.1103/physrevb.63.024102.
- [42] R.-S. Zhou and R. L. Snyder, "Structures and transformation mechanisms of the eta, gamma, and theta transitions aluminas," *Acta Cryst.*, vol. B47, pp. 617-630, 1991.
- [43] G. Paglia *et al.*, "Boehmite Derived  $\gamma$ -Alumina System. 1. Structural Evolution with Temperature, with the Identification and Structural Determination of a New Transition Phase,  $\gamma'$ -Alumina," *Chem. Materia.*, vol. 16, pp. 220-236, 2004, doi: 10.1021/cm034917j.
- [44] L. Smrcok, V. Langer, and J. Krestan, "Gamma-alumina: a single-crystal X-ray diffraction study," *Acta Crystallogr C*, vol. 62, no. Pt 9, pp. i83-4, Sep 2006, doi: 10.1107/S0108270106026850.
- [45] M. Digne, P. Sautet, P. Raybaud, P. Euzen, and H. Toulhoat, "Hydroxyl Groups on  $\gamma$ -Alumina Surfaces: A DFT Study," *Journal of Catalysis*, vol. 211, no. 1, pp. 1-5, 2002, doi: 10.1006/jcat.2002.3741.
- [46] X. Krokidis, P. Raybaud, A.-E. Gobichon, B. Rebours, P. Euzen, and H. Toulhoat, "Theoretical Study of the Dehydration Process of Boehmite to  $\gamma$ -Alumina," *The Journal of Physical Chemistry B*, vol. 105, no. 22, pp. 5121-5130, 2001, doi: 10.1021/jp0038310.
- [47] L. Kovarik, M. Bowden, A. Genc, J. Szanyi, C. H. F. Peden, and J. H. Kwak, "Structure of  $\delta$ -Alumina: Toward the Atomic Level Understanding of Transition Alumina Phases," *The Journal of Physical Chemistry C*, vol. 118, no. 31, pp. 18051-18058, 2014, doi: 10.1021/jp500051j.

- [48] B. C. Lippens and J. H. De Boer, "Study of phase transformations during calcination of aluminum hydroxides by selected area electron diffraction," *Acta Cryst.*, vol. 17, p. 1312, 1964, doi: 10.1107/S0365110X64003267.
- [49] H. C. Stumpf, A. S. Russell, J. W. Newsome, and C. M. Tucker, "Thermal Transformations of Aluminas and Alumina Hydrates - Reaction with 44% Technical Acid," *Industrial & Engineering Chemistry*, vol. 42, no. 7, pp. 1398-1403, 1950, doi: 10.1021/ie50487a039.
- [50] C. R. Henry, "Surface studies of supported model catalysts," *Surface Science Reports*, vol. 31, no. 7-8, pp. 231-325, 1998, doi: 10.1016/s0167-5729(98)00002-8.
- [51] D. W. Blakely and G. A. Somorjai, "The stability and structure of high miller index platinum crystal surfaces in vacuum and in the presence of adsorbed carbon and oxygen," *Surface Science*, vol. 65, no. 2, pp. 419-442, 1977, doi: 10.1016/0039-6028(77)90457-5.
- [52] Y. Iwasawa, R. Mason, M. Textor, and G. A. Somorjai, "The reactions of carbon monoxide at coordinatively unsaturated sites on a platinum surface," *Chemical Physics Letters*, vol. 44, no. 3, pp. 486-470, 1976, doi: 10.1016/0009-2614(76)80706-3.
- [53] F. Gao and D. W. Goodman, "Model Catalysts: Simulating the Complexities of Heterogeneous Catalysts," *Annual Review of Physical Chemistry*, vol. 63, no. 1, pp. 265-286, 2012, doi: 10.1146/annurev-physchem-032511-143722.
- [54] M. K. Santala, V. Radmilovic, R. Giulian, M. C. Ridgway, A. M. Glaeser, and R. Gronsky, "Precipitate orientation relationships in Pt-implanted sapphire," *Scripta Materialia*, vol. 62, no. 4, pp. 187-190, 2010, doi: 10.1016/j.scriptamat.2009.10.023.
- [55] M. K. Santala, V. Radmilovic, R. Giulian, M. C. Ridgway, R. Gronsky, and A. M. Glaeser, "The orientation and morphology of platinum precipitates in sapphire," *Acta Materialia*, vol. 59, no. 12, pp. 4761-4774, 2011, doi: 10.1016/j.actamat.2011.04.012.
- [56] C. W. White *et al.*, "Ion Implantation and Annealing of Oxides," *Nuclear Instruments and Methods in Physics Research*, no. B32, pp. 11-22, 1987.
- [57] J. Jefferson, "Swords to Plowshares - A Short History of ORNL," S. Wyatt, Ed., ed. Oak Ridge TN: Oak Ridge Office of Public Affairs, 1993.
- [58] J. Choi and S. J. An, "Effects of arsenic implantation and rapid thermal annealing on ZnO nanorods for p-type doping," *Journal of Vacuum Science & Technology B*, vol. 38, no. 5, 2020, doi: 10.1116/6.0000041.
- [59] K. J. Kirkby and R. P. Webb, "Ion Implanted Nanostructures," in *Encyclopedia of Nanoscience and Nanotechnology* vol. 4, H. S. Nalwa, Ed., ed. University of Surrey, Guildford, Surrey, United Kingdom, 2004, pp. 1-11.
- [60] J. F. Ziegler, M. D. Ziegler, and J. P. Biersack, "SRIM – The stopping and range of ions in matter (2010)," *Nuclear Instruments and Methods in Physics Research Section B: Beam Interactions with Materials and Atoms*, vol. 268, no. 11-12, pp. 1818-1823, 2010, doi: 10.1016/j.nimb.2010.02.091.
- [61] N. Yu, P. C. McIntyre, M. Nastasi, and K. E. Sickafus, "High-quality epitaxial growth of  $\gamma$  -alumina films on  $\alpha$  -alumina sapphire induced by ion-beam bombardment," vol. 52, no. 24, pp. 17518-17522, 1995, doi: 10.1103/physrevb.52.17518.
- [62] J. D. Budai, C. W. White, S. P. Withrow, M. F. Chisholm, J. Zhu, and R. A. Zuhr, "Controlling the size, structure and orientation of semiconductor nanocrystals using metastable phase recrystallization," *Nature*, vol. 390, no. 6658, pp. 384-386, 1997, doi: 10.1038/37079.

- [63] L. Nguyen, F. F. Tao, Y. Tang, J. Dou, and X. J. Bao, "Understanding Catalyst Surfaces during Catalysis through Near Ambient Pressure X-ray Photoelectron Spectroscopy," *Chem Rev*, vol. 119, no. 12, pp. 6822-6905, Jun 26 2019, doi: 10.1021/acs.chemrev.8b00114.
- [64] L. Zhang, A. M. Karim, M. H. Engelhard, Z. Wei, D. L. King, and Y. Wang, "Correlation of Pt–Re surface properties with reaction pathways for the aqueous-phase reforming of glycerol," *Journal of Catalysis*, vol. 287, pp. 37-43, 2012, doi: 10.1016/j.jcat.2011.11.015.
- [65] K. A. Goulas, A. V. Mironenko, G. R. Jenness, T. Mazal, and D. G. Vlachos, "Fundamentals of C–O bond activation on metal oxide catalysts," *Nature Catalysis*, vol. 2, no. 3, pp. 269-276, 2019, doi: 10.1038/s41929-019-0234-6.
- [66] H. O. Ayoola *et al.*, "Probing the Local Bonding at the Pt/ $\gamma$ -Al<sub>2</sub>O<sub>3</sub> Interface," *The Journal of Physical Chemistry C*, vol. 124, no. 18, pp. 9876-9885, 2020, doi: 10.1021/acs.jpcc.9b12029.
- [67] Y. Jin, H. Xu, and A. K. Datye, "Electron energy loss spectroscopy (EELS) of iron Fischer-Tropsch catalysts," *Microsc Microanal*, vol. 12, no. 2, pp. 124-34, Apr 2006, doi: 10.1017/S1431927606060144.
- [68] D. B. Williams and C. B. Carter, 2, Ed. *Transmission Electron Microscopy*. Springer, 2009.
- [69] P. Santiago, L. Rendon, C. Reza-San German, and U. Pal, "HAADF imaging: an effective technique for the study of nonhomogeneous nanostructures," *J Nanosci Nanotechnol*, vol. 5, no. 7, pp. 1172-6, Jul 2005, doi: 10.1166/jnn.2005.139.
- [70] J. M. Lebeau, S. D. Findlay, L. J. Allen, and S. Stemmer, "Standardless Atom Counting in Scanning Transmission Electron Microscopy," *Nano Letters*, vol. 10, no. 11, pp. 4405-4408, 2010, doi: 10.1021/nl102025s.
- [71] K. Ishizuka, "A practical approach for STEM image simulation based on the FFT multislice method," *Ultramicroscopy*, vol. 90, no. 2-3, pp. 71-83, 2002, doi: 10.1016/s0304-3991(01)00145-0.
- [72] J. M. Cowley and A. F. Moodie, "The Scattering of Electrons by Atoms and Crystals. I. A New Theoretical Approach," *Acta Cryst.*, vol. 10, pp. 609-619, 1957, doi: 10.1107/s0365110x57002194
- [73] C. Ophus, "A fast image simulation algorithm for scanning transmission electron microscopy," *Advanced Structural and Chemical Imaging*, vol. 3, no. 1, 2017, doi: 10.1186/s40679-017-0046-1.
- [74] M. W. Small, S. I. Sanchez, L. D. Menard, J. H. Kang, A. I. Frenkel, and R. G. Nuzzo, "The atomic structural dynamics of gamma-Al<sub>2</sub>O<sub>3</sub> supported Ir-Pt nanocluster catalysts prepared from a bimetallic molecular precursor: a study using aberration-corrected electron microscopy and X-ray absorption spectroscopy," *J Am Chem Soc*, vol. 133, no. 10, pp. 3582-91, Mar 16 2011, doi: 10.1021/ja110033g.
- [75] L. Samain *et al.*, "Structural analysis of highly porous  $\gamma$ -Al<sub>2</sub>O<sub>3</sub>," *Journal of Solid State Chemistry*, vol. 217, pp. 1-8, 2014, doi: 10.1016/j.jssc.2014.05.004.
- [76] W. Sinkler, S. Bradley, U. Ziese, and K. D. Jong, "3D-TEM Study of Gamma Alumina Catalyst Supports," *Microscopy and Microanalysis*, vol. 12, no. S02, pp. 52-53, 2006, doi: 10.1017/s1431927606067869.
- [77] J. H. Kwak *et al.*, "Coordinatively Unsaturated Al<sup>3+</sup> Centers as Binding Sites for Active Catalyst Phases of Platinum on  $\gamma$ -Al<sub>2</sub>O<sub>3</sub>," *Science*, vol. 325, pp. 1670-1673, 2009.

- [78] Konstantin Khivantsev, †,\* Nicholas R. Jaegers,<sup>1,2</sup> † Ja-Hun Kwak,<sup>3,\*</sup> Janos Szanyi,<sup>1,\*</sup> and Libor Kovarik<sup>1,†,\*</sup>, "Precise identification and characterization of catalytically active sites on the surface of  $\gamma$ -alumina."
- [79] K. Oware Sarfo, A. L. Clauser, M. K. Santala, and L. Árnadóttir, "On the atomic structure of Pt(1 1 1)/ $\gamma$ -Al<sub>2</sub>O<sub>3</sub>(1 1 1) interfaces and the changes in their interfacial energy with temperature and oxygen pressure," *Applied Surface Science*, vol. 542, 2021, doi: 10.1016/j.apsusc.2020.148594.

## 2. Preliminary Experimental Studies

### 2.1. Formation of dense $\gamma$ -alumina via “self-implantation”

The main goal of this work is to characterize interfaces of Pt nanoparticles embedded within  $\gamma$ -alumina and other transitions aluminas structurally and chemically at an atomic scale. This is described in the Chapters 3, 4, and 5 in the form of an archival journal publication (Chapter 3) and two drafts for journal articles (Chapters 4 and 5). The embedded particles were formed by ion implantation of Pt into synthetic single crystal  $\alpha$ -alumina (sapphire) wafers followed by thermal annealing.

During this project, the potential for creating dense  $\gamma$ -alumina surface layers on sapphire wafers as a substrate for supported metal nanoparticles was also explored. The process of ion implantation can also be used with species that constitute the oxide layer, therefore maintaining the stoichiometry of the layer and producing an amorphous pure layer of oxide with a tuned thickness [1]. This so-called “self-implantation” was used initially in producing amorphous alumina to overcome the thickness limitations of thermal oxidation and to avoid the introduction of impurities that may occur during sputtering [2]. Implantation of Al and O ions can amorphized a surface or sub-surface layer of  $\text{Al}_2\text{O}_3$  without introducing any impurities into the damaged layer. The viability of this processing method was checked initially using stoichiometric implantation of aluminum and oxygen ions to amorphized sapphire targets. Here, self-implanted samples produced using the same nominal implantation parameters as in references [3, 4] were then annealed at 800°C and 850°C to determine the best parameters for generating pristine  $\gamma$ -alumina. The intent was to anneal the partially amorphized sapphire at relatively high temperatures and for a long enough time to form highly crystalline  $\gamma$ -alumina while avoiding conversion to  $\delta$ -alumina or re-growth of the  $\alpha$ -alumina. X-ray diffraction (XRD) and TEM were

performed on these materials to characterize the level of crystallinity and the phase development in the alumina in the absence of the implanted Pt.

XRD was used here to provide overall information on the level of crystallinity and phase of alumina that developed in the ion implanted and subsequently annealed wafers. XRD has been used in many studies to identify transition alumina development during processing. *In situ* XRD boehmite dehydration studies coupled with differential thermal analysis were used by Lamouri *et al.* to pinpoint the relationship between developed transition alumina phases and the XRD peaks they exhibit [5]. This is important because these phases are related through their structure and many of the d-spacings that one phase exhibits are also present in the others. In the work by Lamouri *et al.*, key boehmite peaks first disappear at around 500°C. A wide range of temperatures produced the characteristic  $\gamma$ -alumina peak at 45.9° 2 $\theta$  from 600°C to almost 1000°C; this peak is associated with a d-spacing of  $d_{(400)\gamma} = 1.977\text{\AA}$ . At around 900°C diffraction peaks associated with  $\delta$ -alumina appear first as a shoulder to the 45.9° =  $d_{(400)\gamma}$   $\gamma$ -alumina peak, and then as a series of peaks from 1000°C to 1100°C at  $d_{(00.12)\delta} = 46.49^\circ$ ,  $d_{(318)\delta} = 47.50^\circ$  and  $d_{(319)\delta}$  and  $d_{(22.10)\delta} = 49.91^\circ$ . Between 1000°C and 1200°C a  $\theta$ -alumina distinct peak emerges at  $d_{(600)\theta} = 47.62^\circ$ . Finally at temperatures above 1200°C the  $\alpha$ -alumina peak dominates the pattern near  $d_{(113)\alpha} = 43.40^\circ$ . XRD provides a way to test to implantation and annealing parameters that can be used to produce specific desired phases of transition alumina before labor intensive TEM sample preparation. Selected area electron diffraction has been used to differentiate transition alumina phases [6] and was used here to characterize both the microstructure of the as-implanted sample and the transition phase of annealed specimens.

### 2.1.1. Processing and characterization of self-implanted sapphire: Methods

Self-implanted sapphire wafers were prepared by implanting a 1" × 1" single crystal  $\alpha$ -alumina wafer with the (0001) parallel to the implanted face with a 2:3 ratio of Al and O ions.

Doses of  $4 \times 10^{16}$  Al atoms/cm<sup>2</sup> Al at 90keV and  $6 \times 10^{16}$  O atoms/cm<sup>2</sup> at 55 keV were used to ensure overlap of the implanted region and thus stoichiometric amorphization of the  $\alpha$ -Al<sub>2</sub>O<sub>3</sub> wafer. The wafers were implanted using liquid nitrogen cooling. The stoichiometric implantation of alumina is necessary because using a single species like just Al causes p-type doping in the alumina wafers which in turn can cause Al channeling, a mechanism that effects the resulting crystallinity of the material [7]. The as-implanted sapphire wafer was cut into smaller sections, which were thermal annealed at 800°C and 850°C in air. A Bruker-AXS D8 Discover x-ray diffraction instrument was used to collect diffraction patterns using Cu K<sub>α</sub> ( $\lambda = 0.15406$  nm) with a scan rate of 5° per minute for 10 to 100° 2 $\theta$ . As-implanted samples and samples that were thermally annealed for 25h at 800°C were prepared for examination in the TEM. Samples were prepared in cross section by mechanically thinning glued sections to ~100um and polishing one side to 0.25 um grit. The other side was then dimpled to a thickness of ~20um and polished to a 0.25 um grit finish before being thinned by Ar<sup>+</sup> in a Gatan PIPS II ion mill to perforation with an initial accelerating voltage of 8 keV, the voltage was reduced in stages with final polishing at 0.5 keV. An FEI Titan operated at 200keV was used to collect bright field (BF) images, perform two-beam dark field (DF) experiments, and collect diffraction patterns.

### 2.1.2. Self-implanted sapphire: Results and discussion

Figure 4 shows the XRD patterns of the self-implanted sapphire wafers and the XRD patterns collected after their subsequent annealing. Two prominent peaks are visible at  $2\theta = 41.72^\circ$  and  $90.76^\circ$  in all the patterns and are associated with  $(0006)_\alpha$  and  $(000.12)_\alpha$   $\alpha$ -alumina planes. Ion implantation only amorphizes a thin layer of material near the surface of the

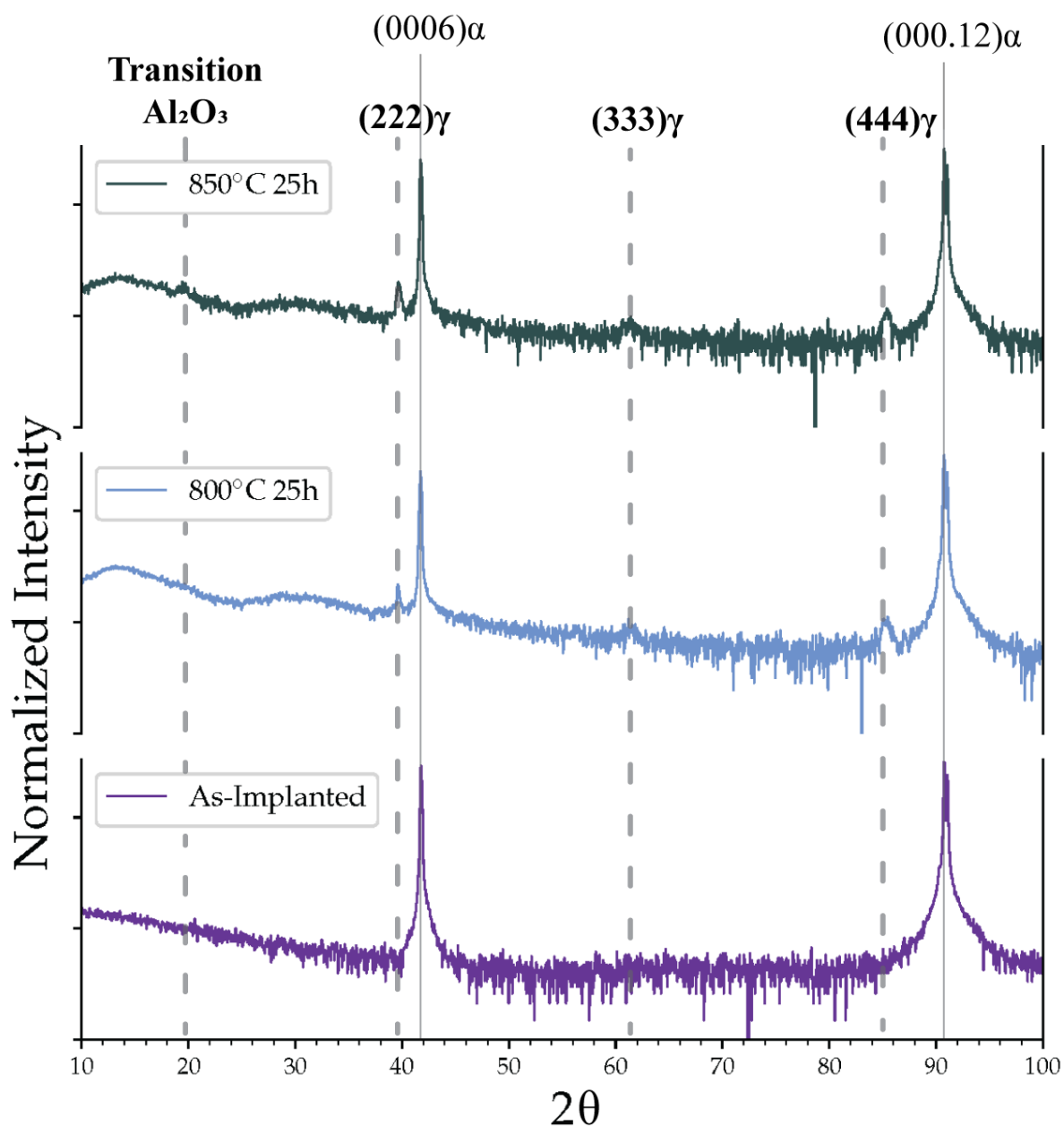


Figure 4 XRD patterns for “self-implanted” sapphire wafers

*XRD patterns for sapphire wafers amorphized using Al and O with annealing parameters as labeled: as-implanted, 800°C for 25 h and 850°C for 25 h. Diffraction peaks from the undamaged  $\alpha$ -alumina wafer are labeled with solid lines. Dashed lines indicate  $\gamma$ -alumina planar spacings. The amorphous hump from the XRD stage obscures the  $(111)\gamma$  peak in the 800°C and 850°C samples, but peak from the family of planes are visible at  $2\theta = 39, 60.5, 83.3$ .*

wafer. The remaining wafer of single crystal  $\alpha$ -alumina still makes up most of the sample. These peaks have very large intensities with respect to the other diffraction peaks because of single crystal alignment of crystalline planes in the sapphire wafers that have the  $(0001)_\alpha$  parallel to the implanted wafer face. This family of planes is related to the of hexagonal close-packed planes of O with Al atoms in octahedral interstices of the O-sublattice. In the annealed samples, diffraction peaks from transition phases of alumina are present and can be used to infer recrystallization of the amorphized substrate. After 25 h at 800°C, peaks develop in the XRD patterns with a d-spacing consistent with the  $\{111\}_\gamma$  family of planes. The peaks associated with this family of planes are labeled on Figure 4. The  $(111)_\gamma$  may be obscured in the 800°C pattern by a broad hump in the scan located from 10-22° 2 $\theta$  due background from the amorphous polymer stage used when collecting the XRD data from small samples. The  $\{111\}$  family of planes are the close packed planes in the cubic transition phases of alumina and do not uniquely identify the phase as  $\gamma$ -alumina, the diffraction peak from the  $(111)_\gamma$  plane has a d-spacing that is very close to both the  $(201)_\theta$  and also the  $(113)_\delta$  planes. There are no  $\gamma$ -alumina d-spacings expected to have prominent peaks that exist solely in the  $\gamma$  phase. The  $(444)_\gamma$  reflection at  $\sim 85.0^\circ$  2 $\theta$  does not share d-spacings with other transition phases but it does have a similar d-spacing with the  $(311)_\alpha$  alumina planes and diffracts at a much lower intensity. This means that further characterization is needed to confirm the presence of these transition phases beyond XRD. At higher anneal temperatures of 850°C the XRD pattern remains the same. A topotaxial crystallization relative to the underlying  $\alpha$ -alumina can be inferred by the concomitant presence of  $\{111\}_\gamma$  and  $\{0001\}_\alpha$  peaks. Using XRD alone on these self-implanted samples is inconclusive with respect to differentiating different phases of transition alumina, but did indicate that, in the range of 800 – 850°C, 25 h anneals would not result is complete recovery to the  $\alpha$ -alumina

phase Figure 5 shows a cross-section of a self-implanted sapphire wafer in a bright field TEM image and selected area electron diffraction pattern taken from the lower boundary of damaged  $\alpha$ -alumina and the amorphized layer above. This image is viewed down the  $[10\bar{1}0]_{\alpha}$  direction of the  $\alpha$ -alumina. The featureless, lighter area of the implanted wafers is a layer of amorphized alumina. The inset of this figure shows a diffraction pattern of a crystalline  $\alpha$ -alumina layer topped by an amorphous layer. The inset diffraction pattern has both a clear  $[10\bar{1}0]_{\alpha}$  zone axis pattern (indexed) and a broad ring indicating the selected area has both highly crystalline sapphire and an amorphized layer. Figure 6 shows (a) zone-axis BF, (b) a two-beam DF image, and (c-d) selected area diffraction patterns from two zone axes of a cross section of self-implanted alumina that had been annealed for 25 h at 800°C. The zone axis diffraction patterns may be consistently indexed with  $\alpha$ - and  $\gamma$ -alumina phases. The  $\delta$ -alumina structure has a distinct superlattice made of multiple spinel unit cells and the absence of the superlattice reflections (as in Figure 7) can be used to confirm that the transformation of the alumina has not proceeded beyond the desired  $\gamma$ -alumina phase during annealing. Simulated zone axis diffraction patterns of  $\gamma$ - and  $\delta$ -alumina are shown in Figure 13f, where they were used to confirm the presence of  $\gamma$ -alumina and the absence of  $\delta$ -alumina in thermally annealed Pt-implanted sapphire. In the DF image shown in Figure 6, the  $(222)_{\gamma}$  spot was selected using the objective aperture. Areas of the sample that are strongly diffracting from that crystalline set of planes are the brightest areas of the DF image under two-beam imaging conditions. From this image, one can see that  $\gamma$ -alumina has grown into the previously amorphized area from the  $\alpha$ -alumina beneath all the way up to the surface of the wafer. From the diffraction patterns, one may see that the  $(0003)_{\alpha}$  planes, the close-packed O planes in  $\alpha$ -alumina, are parallel to the  $(111)$  close-packed planes of oxygen in  $\gamma$ -alumina. The single crystal  $\alpha$ -alumina provided a template for the epitaxial

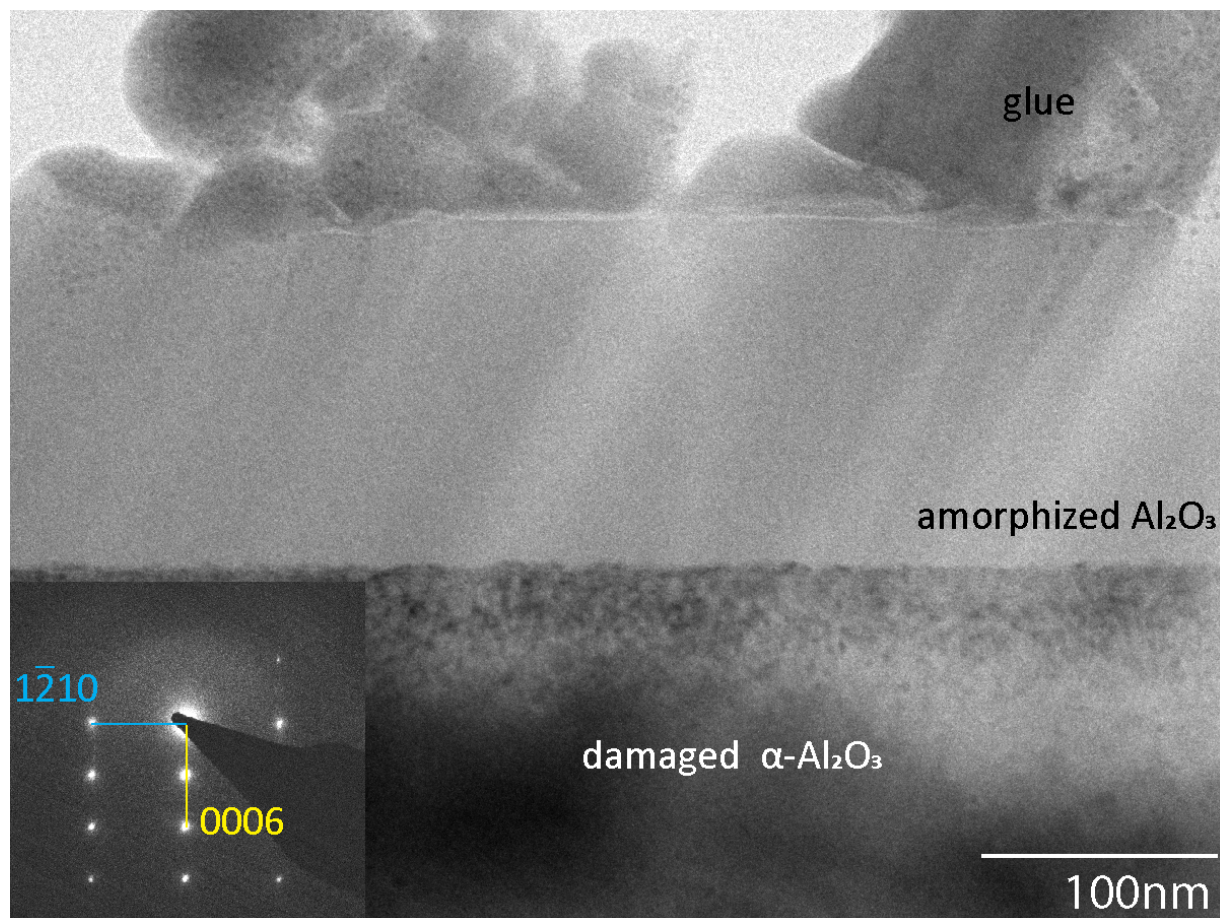


Figure 5 Bright field TEM image of self-implanted sapphire

*Bright field TEM image of self-implanted sapphire and corresponding selected area diffraction pattern. They were taken on the  $[10\bar{1}0]$  zone axis and show the amorphization of the top implanted layer of alumina*

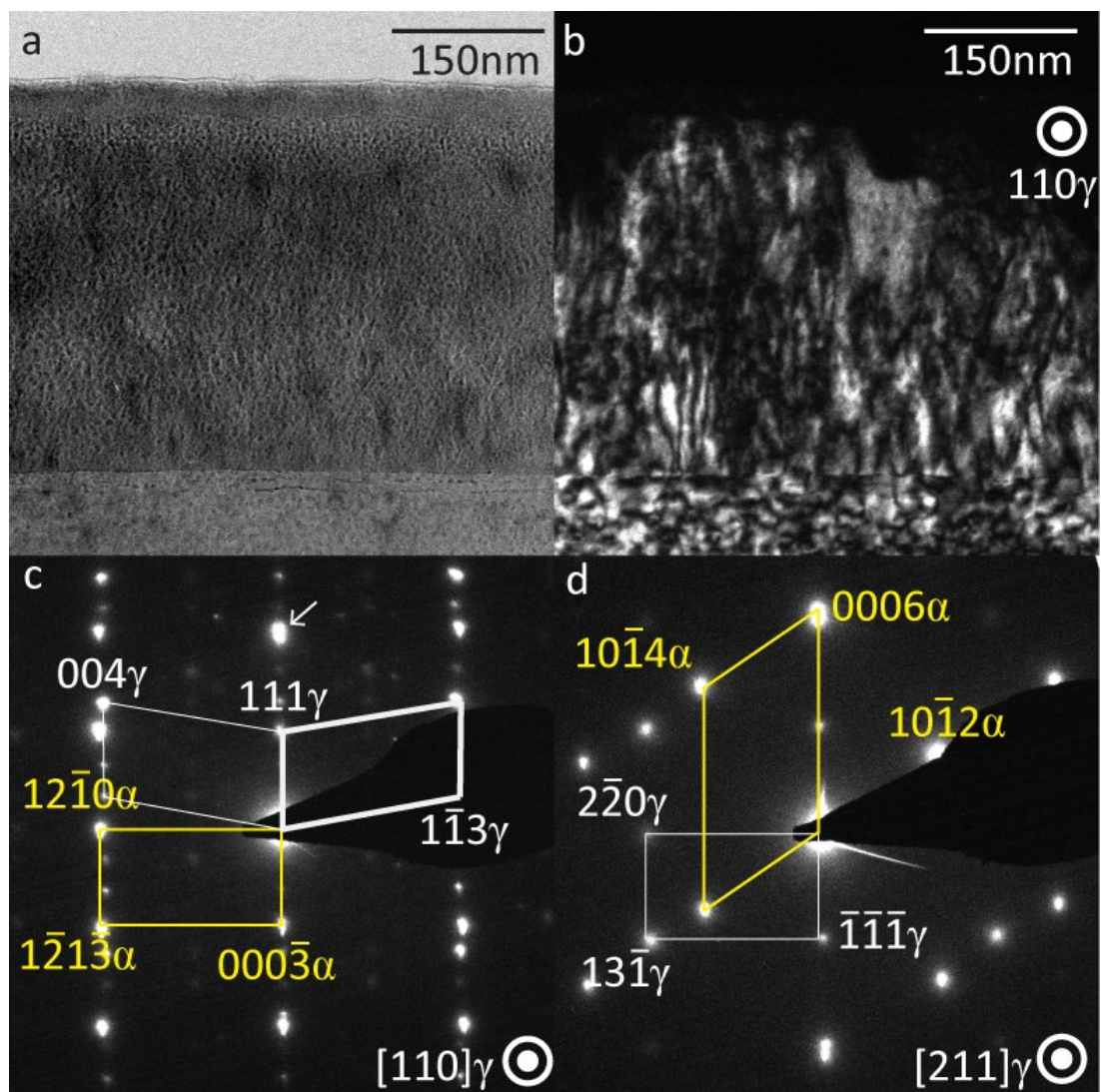


Figure 6 TEM BF and DF image pair with  $[110]$  and  $[211]$  diffraction patterns

(a) a zone-axis TEM brightfield image of self-implanted alumina annealed at  $800^{\circ}\text{C}$  for 25h and (b) dark field image pair using the  $(222)\gamma$  spot indicated by the white arrow in (c) a diffraction pattern collected down the  $[110]\gamma$  zone axis. (d) a diffraction pattern collected down the  $[211]\gamma$  zone axis that shows the epitaxial growth determined by the close packed planes  $(0006)\alpha \parallel (111)\gamma$

growth of  $\gamma$ -alumina from the damaged/amorphous layer boundary. These preliminary experiments have established a processing method for creating dense, highly oriented  $\gamma$ -alumina surfaces for model studies of  $\gamma$ -alumina-supported metal nanoparticles.

## **2.2. Preliminary characterization studies on Pt-implanted sapphire**

The self-implanted alumina studies showed that the process did generate an identifiable  $\gamma$ -alumina phase from implantation amorphized alumina. Several Pt implantation doses were used to find the best dose and annealing parameters for the generation of transition alumina dense with faceted Pt nanoparticles (NPs). The approach was taken under the assumption that if more Pt NPs were present, there would be more faceted interfaces present and available for characterization. Because these phases were going to be damaged by high-energy implantation with relatively large (high atomic number)  $\text{Pt}^+$  ions, increased anneal times were used to ensure that Pt had enough time to diffuse through the alumina and was able to form relatively large faceted NPs within the samples and also to make sure that a complete transformation of  $\gamma$ -alumina had occurred.

### 2.2.1. Processing and characterization of Pt-implanted sapphire: Methods

Three different doses of increasing Pt concentration were implanted into (0001) oriented  $\alpha$ -alumina wafers. Implantation energies of 600 keV  $\text{Pt}^+$  ions at  $7^\circ$  to the normal of the sapphire wafer were performed at room temperature. Two wafers were implanted in a 300 kV Tandatron at the Ion Implantation Laboratory at the Universidade Federal do Rio Grande do Sul (UFRGS) with target fluences of  $1 \times 10^{16} \text{Pt}^+$  ions/cm<sup>2</sup>,  $5 \times 10^{16} \text{Pt}^+$  ions/cm<sup>2</sup>, and  $1 \times 10^{17} \text{Pt}^+$  ions/cm<sup>2</sup>. The samples with the higher  $1 \times 10^{17} \text{Pt}/\text{cm}^2$  dose are discussed in Chapter 3. These implanted samples were annealed with the same parameters that the self-implanted samples were and were the highest implantation dose achieved. However, this higher dose also sometimes caused the

implanted layer to spall off after annealing due to the high density of sub-surface Pt nanoparticles, so no higher doses were attempted. The Rutherford backscatter spectroscopy used to initially confirm fluences was performed at the Ion Implantation Laboratory at UFRGS using 1 MeV He<sup>+</sup> ions and the backscattered ions were detected by a surface barrier detector. RUMP software (version 2.0) was used to analyze the data and is further discussed in Chapter 3 [8, 9]. The  $1 \times 10^{17}$  Pt/cm<sup>2</sup> implantation dose proved to be the best candidate for atomic resolution aberration corrected STEM and was used to determine the chemical termination of implanted NPs. This is further discussed in Chapters 3 and 4. The preliminary results with the lower doses of Pt are described here.

To convert the amorphized alumina to  $\gamma$ -alumina and to precipitate the implanted Pt the  $1 \times 10^{16}$  Pt/cm<sup>2</sup> implanted sapphire wafer was cut into smaller sections and pieces were annealed in air at 800 and 850°C for 500 h. These implanted wafers were annealed at longer times than self-implanted alumina to overcome a slowing of the rate of crystallization due to the kinetic impediment that is known to be imposed when large non-native ions are incorporated into crystalline structures [10]. The samples that were implanted with  $1 \times 10^{16}$  Pt/cm<sup>2</sup> were sliced into 3 mm sections and then annealed. These sections were then scanned by a Bruker-AXS D8 Discover x-ray diffraction instrument using Cu K $\alpha$  radiation ( $\lambda = 0.15406$  nm) at a scan rate of 5° per minute for 10 to 100° 2 $\theta$ . These samples were then prepared in cross section for TEM and mechanically polished and dimpled in the same manner as the self-implanted samples discussed previously. A 200 keV FEI Titan was used to characterize the samples once they had been prepared to collect brightfield, darkfield and selected area electron diffraction patterns of the implanted layers of alumina. Transmission electron microscopy was performed on the cross sections of sapphire implanted with  $1 \times 16$  Pt/cm<sup>2</sup> using the method described for the self-

implanted specimens in 2.1. A single exploratory *in situ* annealing experiment was performed on TEM cross section of from the as-implanted specimen with this implantation dose as well. A Gatan model 652 heating holder,<sup>1</sup> which has a maximum temperature of 900°C, was used to heat a piece of as-implanted alumina that had been prepared as a TEM cross section to 800°C in the TEM. Zone axis diffraction patterns were taken using a double tilt holder and were similar to patterns collected in furnace annealed samples.

The specimen implanted with  $5 \times 16 \text{ Pt/cm}^2$  was also cut into 3 mm wide strips and pieces were annealed at 800°C and 850°C in air (the temperatures from the self-implanted and  $1 \times 10^{16} \text{ Pt/cm}^2$  studies). This specimen was also annealed at 750°C for 100h. XRD was performed on the wafers and then prepared in cross section for TEM as previously described.

### 2.2.2. Preliminary characterization of Pt-implanted sapphire: Results

The XRD patterns in Figure 7 are of sapphire wafers that were implanted with  $1 \times 10^{16} \text{ Pt/cm}^2$ . The XRD patterns from the Pt-implanted specimen show the same development of alumina phases upon annealing as in the self-implanted specimens described in section 2.1.2 with the exception that now Pt is present. In the as-implanted sample, there are two indexed  $\alpha$ -alumina peaks present as observed previously in the self-implanted sapphire. The XRD patterns of the specimen annealed at 800°C for 500 h reflect the development of a transition phase of alumina and the precipitation of Pt. This is seen as a series of larger peaks associated with  $\{111\}_{\text{Pt}}$  and  $\{111\}_{\gamma}$  families of planes. These phases have very similar d-spacings so the (111) and  $(222)_{\text{Pt}}$  peaks overlap with the transition alumina, so it cannot be determined from XRD alone if the Pt is present, however the TEM results (described below) confirm the presence of both crystalline Pt and  $\gamma$ -alumina and the XRD peaks are labeled as such.

---

<sup>1</sup> Gatan, Inc. W. Las Positas Blvd, Pleasanton, CA

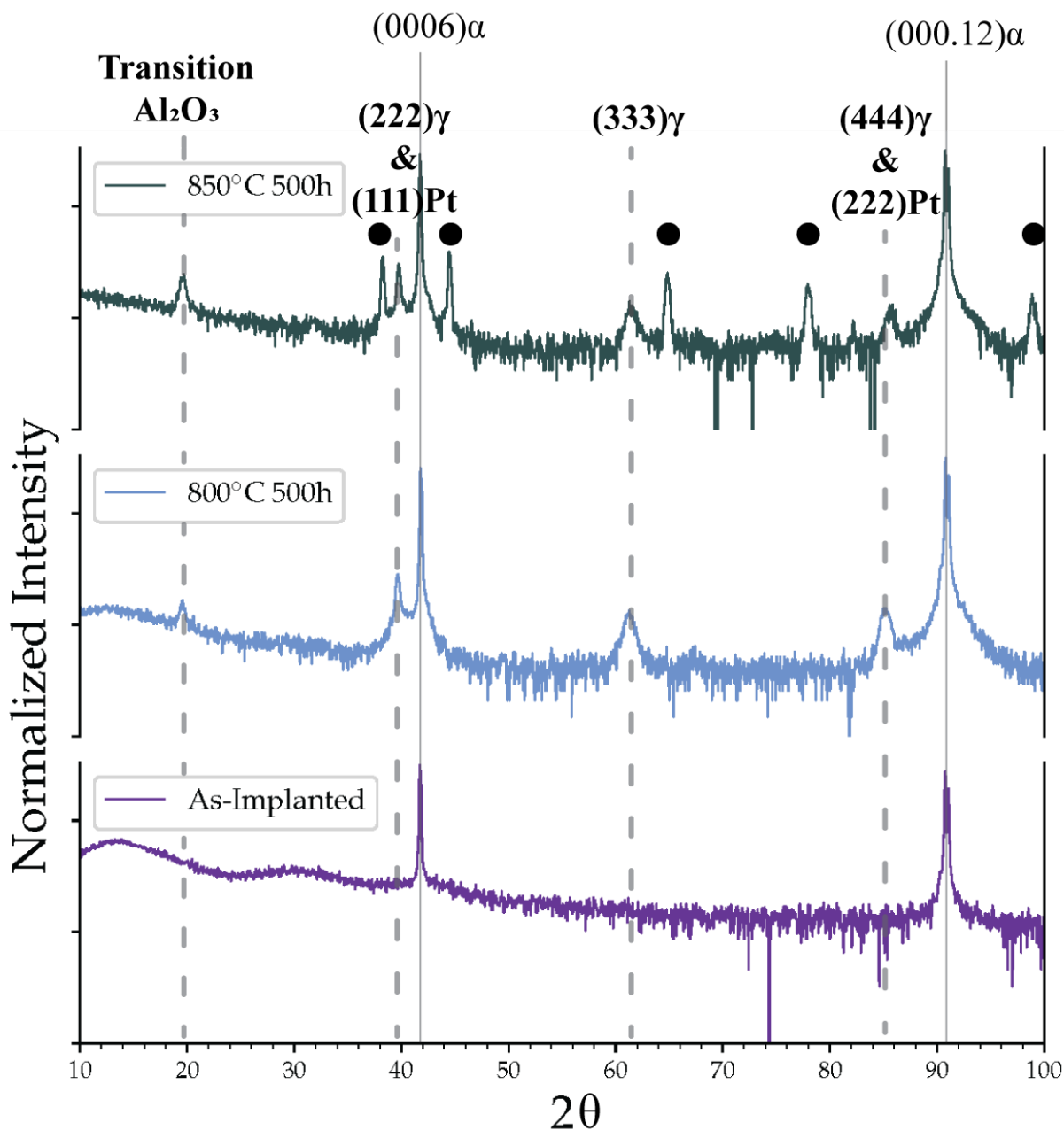


Figure 7 XRD patterns for alumina wafers implanted with a Pt dose of  $1 \times 10^{16} \text{ cm}^{-2}$

*XRD patterns for alumina wafers implanted with a Pt dose of  $1 \times 10^{16} \text{ cm}^{-2}$  then annealed at 800°C for 500h and 850°C for 500h. The (222) and (444)  $\gamma$ -alumina planes share planar spacings with Pt (111) and (222) planes of the precipitated nanoparticles, so these peaks overlap. The presence of both phases is confirmed by TEM diffraction. Black dots mark peaks that are not associated with  $\gamma$ -alumina but are present in later transition phases and are summarized in Table 1.*

After 500 h at 850°C, transition alumina peaks not associated with  $\gamma$ -alumina develop. These peaks are marked by black circles and associated with  $\delta$ -alumina or  $\theta$ -alumina the next phase in the irreversible crystallization series discussed in Chapter 1. These reflections are summarized in Table 1. The development of  $\delta$ -alumina in this sample at 850°C led to the elimination of this as a possible annealing temperature for generating Pt NPs in  $\gamma$ -alumina. Previous work on the orientation relationships between  $\alpha$ - and  $\theta$ -alumina [11] show  $\theta$ -alumina develops in Pt implanted samples at annealed in air for 1000°C for 250 h. This annealing parameter was used to process specimen for the atomic-resolution study of Pt/ $\theta$ -alumina interfaces discussed in Chapter 5.

Table 1 Transition phases of alumina  $\theta$  and  $\delta$  share planes with similar d-spacings

<b>2<math>\theta</math></b>	<b>d-spacing (Å)</b>	<b>(hkl) <math>\delta</math></b>	<b>(hkl) <math>\theta</math></b>
38.30°	2.35	314,305	401,310
44.51°	2.04	11.10	311,112
64.81°	1.44	440	020
77.94°	1.23	624	222
98.92°	1.01	800	622,224

Figure 8 shows a TEM image and diffraction pattern of a  $1 \times 16$  Pt/cm<sup>2</sup> implanted sapphire wafer annealed for 500 h at 800°C. In this diffraction pattern Pt precipitates are formed in such that the (111)<sub>Pt</sub> planes are parallel to the (222) <sub>$\gamma$</sub>  alumina planes. Two orientations of  $\gamma$ -alumina can be seen in the diffraction pattern and are marked. The of  $\gamma$ -alumina are twinned along a (111) <sub>$\gamma$</sub>  plane. This orientation relationship is described further in Chapter 3 and imaged at the atomic level using HRTEM and STEM in Chapter 4 for samples with higher Pt doses. The

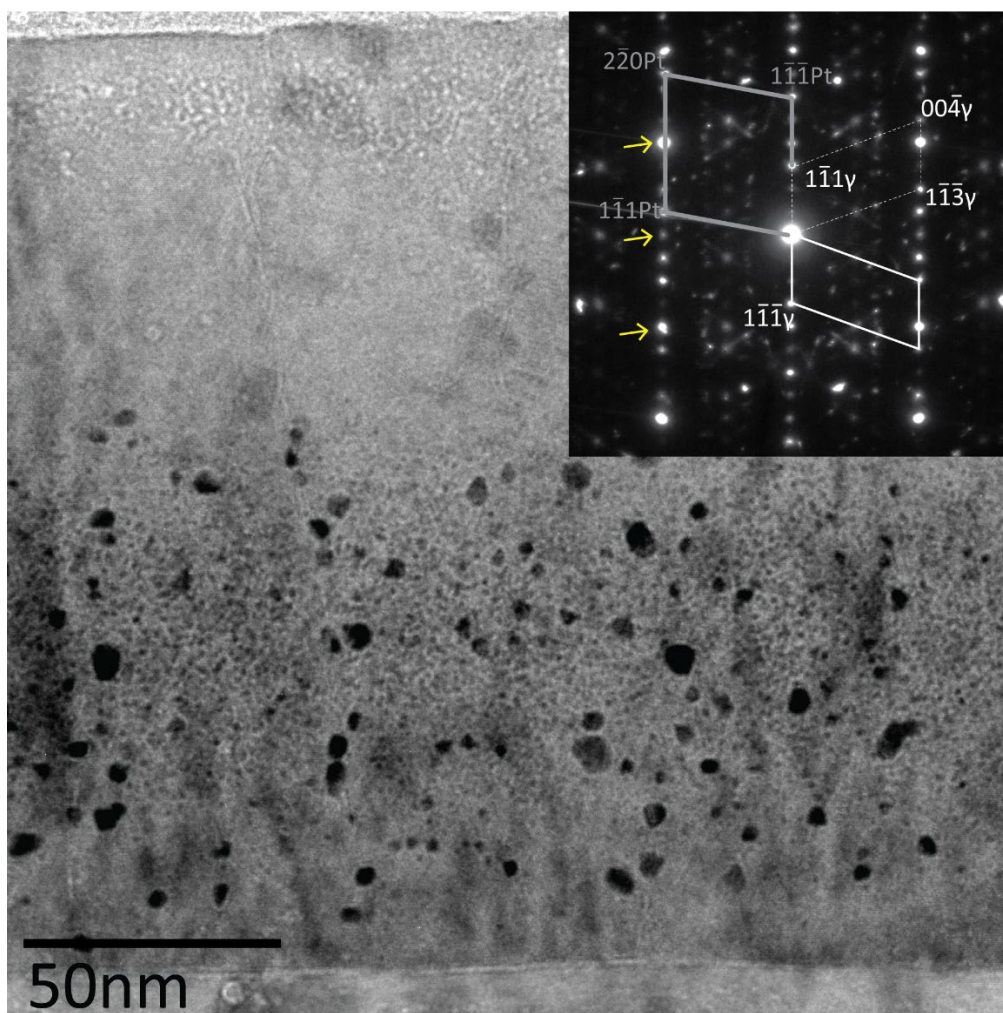


Figure 8 Pt-implanted layer with a dose of  $1 \times 16 \text{ Pt/cm}^2$  TEM image and  $[110]_{\text{Pt}}$  diffraction pattern

*Pt-implanted layer with a dose of  $1 \times 16 \text{ Pt/cm}^2$  of a partially amorphized alumina wafer that had been annealed at  $800^\circ\text{C}$  for 500 h showing the precipitation of faceted NPs in the matrix. The Pt is oriented in the alumina such that the (111) planes of the NP are parallel to the (111) planes of the  $\gamma$ -alumina. Both the Pt and  $\gamma$ -alumina are viewed down the  $[110]$  zone-axis. The two twin variants of  $\gamma$ -alumina are shown in the inset diffraction pattern with white solid and dotted lines. The gray line shows Pt diffraction points. The yellow arrows point to diffraction spots associated with underlying  $\alpha$ -alumina as also seen in Figure 6*

amount of Pt implanted in these preliminary experiments was sufficient to generate Pt NPs in  $\gamma$ -alumina, but based on the results here, higher doses were used in the experiments described in Chapters 3 – 5 to increase the size and density of the Pt nanoparticles to facilitate the atom-level characterization of the interfaces.

The XRD patterns for as implanted and thermally annealed  $5 \times 10^{16}$  Pt/cm<sup>2</sup> dose samples are shown in Figure 9. The as-implanted sample scans have prominent (111)<sub>Pt</sub> and (222)<sub>Pt</sub> peaks that are not present on the  $1 \times 10^{16}$  Pt/cm<sup>2</sup> sample. The lowest and shortest anneal parameters shows the development of diffuse diffraction peaks that were indexed previously to the {111} family of  $\gamma$ -alumina planes. Increasing these anneal times from 100 h to 500 h did not cause any significant change in the diffraction patterns and samples annealed at 750°C for 500 h still have diffuse {111} peaks. Long anneal times at 800°C and 850°C show a sharpening of the peaks associated with the {111}<sub>Pt</sub> and even (222) and (444) of  $\gamma$ -alumina. From the previous work done on the  $1 \times 10^{16}$  cm<sup>-2</sup> samples, it was clear that 850°C would provide enough thermal energy to begin the transformation of transition aluminas beyond  $\gamma$ -alumina phase and is ultimately why 800°C was chosen for the TEM characterization studies described in the following chapters. The odd hkl planes of the {111} family of planes are forbidden reflections in the cubic transition aluminas given an FCC sublattice present in a cubic spinel unit cell. After 500 h at 800°C, the “forbidden” peaks seen in the 750°C samples have flattened and are more consistent with what is to be expected from a well-ordered cubic spinel. In this higher dose Pt implanted sample annealed at 850°C for 500 h the (333) <sub>$\gamma$</sub>  peak is also reduced relative to the specimen annealed at 800°C however there is a development of a sharp (111) peak that could be from  $\gamma$ -alumina but also shares a d-spacing with the (113) <sub>$\delta$</sub>  and (201) <sub>$\theta$</sub> . The peak that is closest in d-spacing to the (444) <sub>$\gamma$</sub>  and (222)<sub>Pt</sub> plane has also shifted to the right nearer to the (000.12) <sub>$\alpha$</sub>  at the 850°C anneal

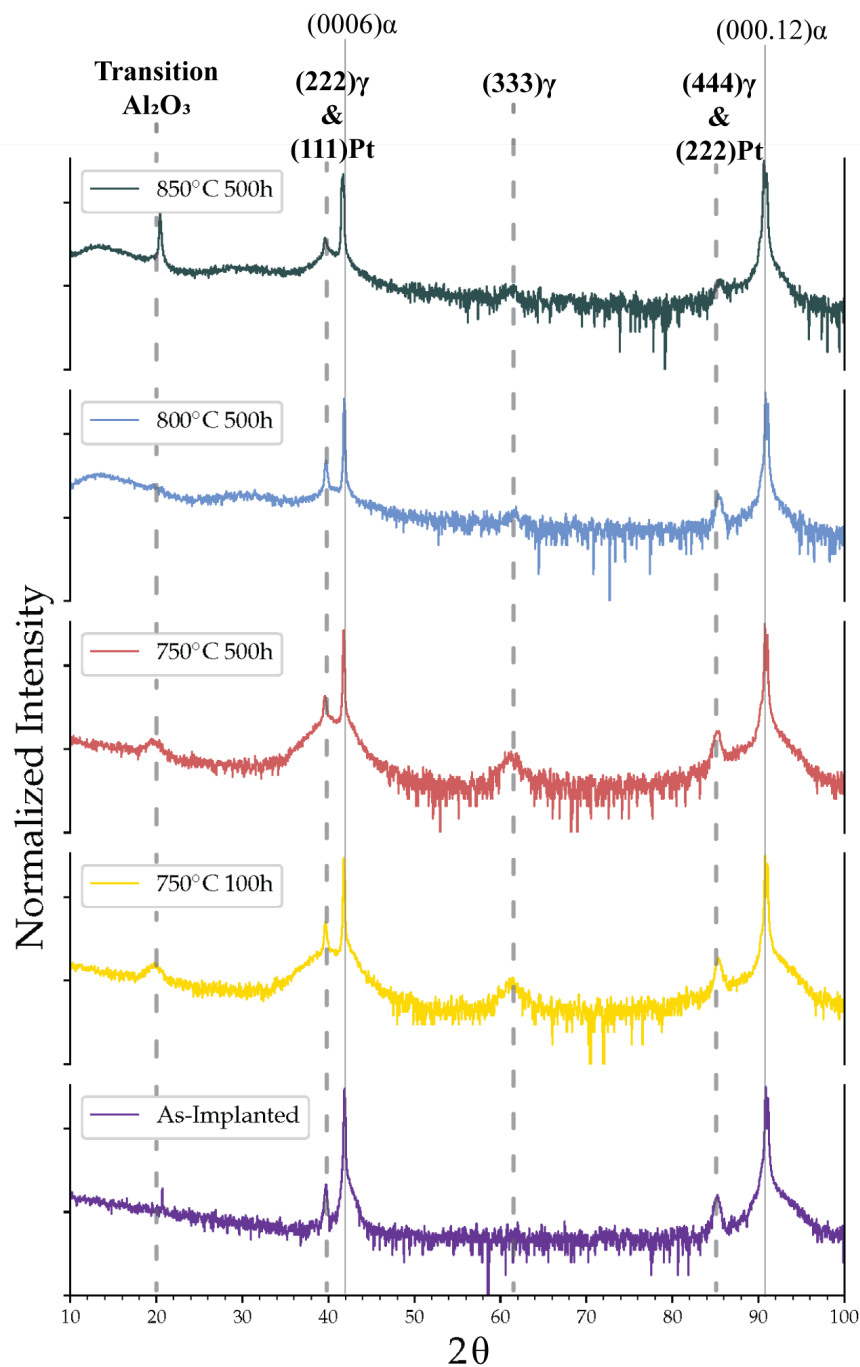


Figure 9 XRD patterns for wafers implanted with  $5 \times 10^{16} \text{ Pt}^+/\text{cm}^2$ .

*The higher density of Pt results in the appearance of  $\{111\}$ Pt peaks before annealing. The odd  $\{111\}$  planes of  $\gamma$ -alumina develop at 750°C at both 100 h and 500h anneal times. The  $\delta$  and  $\theta$  diffraction peaks seen at the same annealing parameters in the  $1 \times 10^{16}$  wafers are not present*

temperature. These diffraction patterns show that the Pt close packed planes and the alumina close packed planes are consistently aligned. The experimental data the XRD and from the TEM selected area diffraction patterns from this implanted set and showed that the orientation relationship between Pt and  $\gamma$ -alumina was consistently  $(111)_{\text{Pt}} \parallel (111)_{\gamma}$  and was used to guide the DFT models of Pt/ $\gamma$ -alumina interfaces performed by collaborators [12].

The results of the exploratory *in situ* annealing study is shown in Figure 10. Heating to 800°C caused the precipitation of Pt particles and conversion of the amorphized to  $\gamma$ -alumina within 2 hours. Zone axis selected area diffraction patterns (not shown) taken after the *in situ* experiment showed that the Pt NPs formed the same orientation relationship to the  $\gamma$ -alumina as for all the other Pt-implanted specimen. However, it is known that the temperature at the sample during *in situ* TEM heating experiments can be unreliable and that such experiments are costly and time consuming relative to *ex situ* TEM. It provided data like that collected with traditional *ex situ* experimentation with the only benefit being the ability to monitor the transformation in real time. Given the long annealing times required to develop the desired microstructures for the interface characterization experiments, *in situ* heating was not utilized beyond this exploratory experiment.

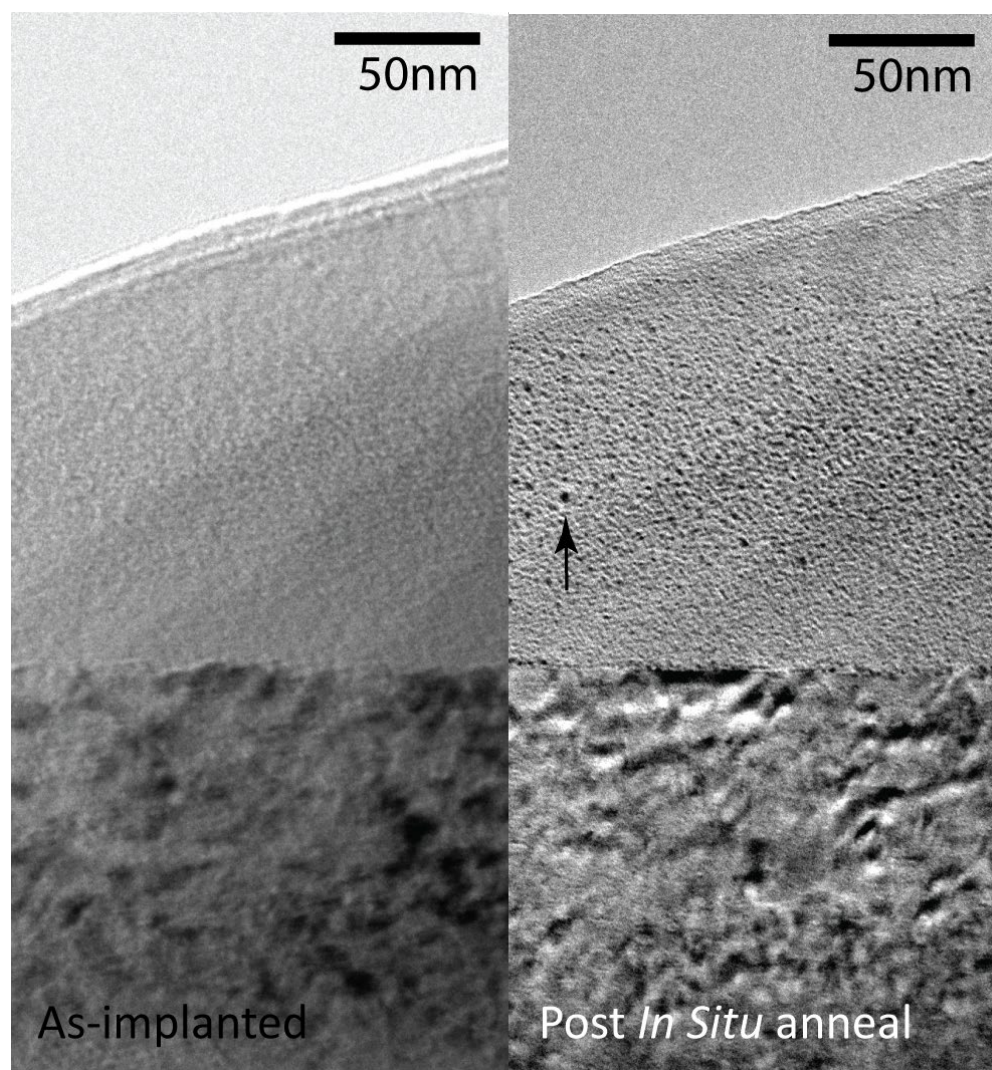


Figure 10 BF TEM images collected during and after in situ TEM annealing of  $5 \times 10^{16} \text{ Pt cm}^{-2}$

*Image shows implanted sapphire in the Gatan heated TEM holder. A relatively large Pt particle is indicated by the black arrow in the post-in-situ-anneal image. Images were not taken on zone-axis due to limitations of tilt imposed by the TEM holder*

## Chapter 2 References

- [1] N. Yu, P. C. McIntyre, M. Nastasi, and K. E. Sickafus, "High-quality epitaxial growth of  $\gamma$ -alumina films on  $\alpha$ -alumina sapphire induced by ion-beam bombardment," vol. 52, no. 24, pp. 17518-17522, 1995, doi: 10.1103/physrevb.52.17518.
- [2] G. C. Farlow, P. S. Sklad, C. W. White, C. J. McHargue, and B. R. Appleton, "The Formation and Annealing of Amorphous Layers of Al<sub>2</sub>O<sub>3</sub>," in *Materials Research Symposium*, 1985, vol. 60, doi: 10.1557/proc-60-387
- [3] C. W. White *et al.*, "Ion-Implantation and Annealing of Crystalline Oxides and Ceramic Materials," *Nuclear Instruments & Methods in Physics Research Section B-Beam Interactions with Materials and Atoms*, vol. 32, no. 1-4, pp. 11-22, May 1988. [Online]. Available: <Go to ISI>://A1988N93740003
- [4] C. W. White, C. J. McHargue, P. S. Sklad, L. A. Boatner, and G. C. Farlow, "Ion implantation and annealing of crystalline oxides," *Material Science Reports*, vol. 4, no. 2-3, pp. 41-146, July 1989, doi: 10.1016/s0920-2307(89)80005-2.
- [5] S. Lamouri *et al.*, "Control of the  $\gamma$ -alumina to  $\alpha$ -alumina phase transformation for an optimized alumina densification," *Boletín de la Sociedad Española de Cerámica y Vidrio*, vol. 56, no. 2, pp. 47-54, 2017, doi: 10.1016/j.bseev.2016.10.001.
- [6] I. Levin, T. Gemming, and D. G. Brandon, *Some Metastable Polymorphs and Transient Stages of Transformation in Alumina*. 1998, p. 197.
- [7] M. K. Linnarsson, A. Hallén, and L. Vines, "Influence of a thin amorphous surface layer on de-channeling during aluminum implantation at different temperatures into 4H-SiC," *Applied Physics A*, vol. 125, no. 12, 2019, doi: 10.1007/s00339-019-3144-1.
- [8] N. P. Barradas *et al.*, "International Atomic Energy Agency intercomparison of ion beam analysis software," vol. 262, no. 2, pp. 281-303, 2007, doi: 10.1016/j.nimb.2007.05.018.
- [9] L. R. Doolittle, "Algorithms for the Rapid Simulation of Rutherford Backscattering Spectra," *Nuclear Instruments and Methods in Physics Research*, vol. 9, no. 3, B, pp. 344-351, June 1984, doi: 10.1016/0168-583X(85)90762-1.
- [10] H. Albetran and I. M. Low, "Effect of indium ion implantation on crystallization kinetics and phase transformation of anodized titania nanotubes using in-situ high-temperature radiation diffraction," *Journal of Materials Research*, vol. 31, no. 11, pp. 1588-1595, 2016, doi: 10.1557/jmr.2016.83.
- [11] M. K. Santala, V. Radmilovic, R. Giulian, M. C. Ridgway, A. M. Glaeser, and R. Gronsky, "Precipitate orientation relationships in Pt-implanted sapphire," vol. 62, no. 4, pp. 187-190, 2010, doi: 10.1016/j.scriptamat.2009.10.023.
- [12] K. Oware Sarfo, A. L. Clauser, M. K. Santala, and L. Árnadóttir, "On the atomic structure of Pt(1 1 1)/ $\gamma$ -Al<sub>2</sub>O<sub>3</sub>(1 1 1) interfaces and the changes in their interfacial energy with temperature and oxygen pressure," *Applied Surface Science*, vol. 542, 2021, doi: 10.1016/j.apsusc.2020.148594.

**3. Orientation and morphology of Pt nanoparticles in  $\gamma$ -alumina processed via ion implantation and thermal annealing**

Arielle L. Clauser

Raquel Giulian

Zachary D. McClure

Kofi Oware Sarfo

Colin Ophus

Jim Ciston

Líney Árnadóttir

Melissa K. Santala

Scripta Materialia

Radarweg 29

1043 NX Amsterdam

The Netherlands

Volume 188

The formation of nanoprecipitates by high-dose ion implantation followed by thermal annealing is a means to alter the near-surface optical, electrical, and magnetic properties of oxides and other insulators and has potential technological applications [1, 2]. The size and spatial distribution of the nanoprecipitates can be controlled by the implantation dose, energy, and annealing temperature and environment. These parameters also impact the level of damage to the matrix and the path of recovery during thermal annealing which in turn can alter the orientation relationships of the precipitates [3]. This provides an opportunity to tune properties [4] and also a platform for studying of metal/oxide interfaces with a variety of interfacial relationships [5]. In this work, high-energy ion implantation of platinum into sapphire ( $\alpha$ -Al<sub>2</sub>O<sub>3</sub>) wafers followed by thermal annealing was used to create a simple, model system of dense  $\gamma$ -alumina with Pt nanoparticles for detailed characterization of orientation relationships, interfacial relationships, and nanoparticle morphology. Platinum dispersed on  $\gamma$ -alumina is an important heterocatalyst system [6, 7]. The orientation, size, and morphology of metal nanoparticles on oxide supports impact the activity of heterogeneous catalyst systems [8, 9], but characterization of Pt nanoparticles on  $\gamma$ -alumina is challenging due to the complexity of  $\gamma$ -alumina and the added degrees of freedom introduced by the nanoparticles. This model system differs substantially from those used for heterocatalysis because the nanoparticles are embedded in the oxide, however its simplicity offers path to study the atomic-level structure of Pt/ $\gamma$ -alumina interfaces. The identification of highly-faceted interfaces with an interfacial relationship common to those observed in supported nanoparticles gives directions for studies on the atomic-level characterization of the interfaces.

The  $\gamma$ -alumina phase is a transition alumina that may be produced by different processing paths, including the topotactic transformation of boehmite [10] or crystallization of amorphous

$\text{Al}_2\text{O}_3$  [11]. The structure of  $\gamma$ -alumina has been the subject of experimental investigations [10-14] and computational simulations [15-19] and yet is still debated. X-ray diffraction (XRD) [10, 11] and other characterization experiments may be inconclusive because of the structural similarities between  $\gamma$ -alumina and other transition aluminas and the frequent co-existence of different alumina phases. Numerous models for  $\gamma$ -alumina have been proposed, including Zhou and Snyder's defect spinel  $\text{Fd}\bar{3}\text{m}$  model derived from XRD and Rietveld refinement of neutron diffraction data [12], a proposed refinement of that model with a tetragonal  $\text{I41}/\text{amd}$  structure [17, 19], and a model with modifications to capture the properties of  $\gamma$ -alumina surfaces [18]. Transmission electron microscopy (TEM) diffraction and high-resolution (HR) imaging have been used to study the structure of  $\gamma$ -alumina and distinguish it from the similar  $\delta$ - and  $\theta$ -alumina forms [11, 20-24].

Ion implantation of Pt into sapphire followed by thermal annealing has been used to produce Pt nanoparticles in  $\gamma$ -alumina [3],  $\theta$ -alumina [25, 26], and  $\alpha$ -alumina [3, 5, 25-27]. Accumulation of damage during ion implantation can result in near-surface amorphization of the sapphire matrix. Annealing induces re-crystallization of the amorphized alumina and precipitation of the implanted Pt. The form of alumina after re-crystallization is determined by the annealing conditions. Upon heating, the expected transitions of amorphous alumina are  $\gamma \rightarrow \delta \rightarrow \theta \rightarrow \alpha$  [11]. These transitions are not reversible upon cooling. While the thermodynamic and kinetic factors influencing the orientation and morphology of Pt with  $\gamma$ -alumina differ between embedded and supported nanoparticles, the study of interfaces in a model system using embedded nanoparticles produced by this processing method provides certain advantages. Topotaxial re-growth of alumina has been reported for  $\gamma/\alpha$  [3, 28, 29] and  $\theta/\alpha$ -alumina [25] interfaces formed during re-crystallization of partially amorphized  $\alpha$ -alumina. The resulting

interfacial relationships have the parallel closed-packed planes of oxygen and parallel alignment of the close-packed oxygen directions. The well-defined orientation relationship of the re-crystallized alumina with the undamaged sapphire matrix greatly simplifies the systematic study of the structure of many nanoparticles through atomic-resolution zone axis imaging.

Introducing Pt sub-surface *via* ion implantation offers great control over the system purity and distribution of the metal. The accumulated damage in the alumina is controlled through the implantation energy, fluence, and substrate temperature. The specimen purity is limited only by the base impurities of the  $\gamma$ -alumina “precursor”, sapphire, which is commercially available with impurity levels under 100 parts per million. The formation of nanoparticles within the alumina, without a pre-existing alumina interface also allows, by comparison, an evaluation of the role of surface orientation on the orientation relationships and interfacial relationships observed in supported particles.

When Pt implanted into alumina precipitates, the orientation relationships that develop depend on the phase of alumina [5, 25-27, 30, 31]. Precipitation into  $\alpha$ -alumina results in multiple orientations of Pt nanoparticles, whereas precipitation of Pt into a  $\theta$ -alumina at 1000°C leads to a single predominant orientation relationship,  $(111)_{Pt} || (\bar{2}01)_{\theta\alpha}; [1\bar{1}0]_{Pt} || [132]_{\theta}$ , [25, 26] in which the close-packed  $\{111\}_{Pt}$  planes are parallel with close-packed planes of the oxygen sub-lattice. These Pt nanoparticles in  $\theta$ -alumina are bound by  $\{111\}_{Pt}$  facets [26]. The structure of  $\theta$ -alumina is related to  $\gamma$ -alumina in its near face-center-cubic packing of the oxygen sublattice, but has a monoclinic, rather than cubic crystal structure. This orientation and morphology results in multiple close-packed directions to be in parallel alignment at the interfaces.

Pt nanoparticles embedded in alumina were produced via ion implantation and thermal annealing of 99.99% pure optical grade sapphire wafers with [0001] direction normal to the wafer face. The alumina was partially amorphized by implantation of 600 keV Pt<sup>+</sup> ions at 7° to the normal of the sapphire wafer at room temperature. Two wafers were implanted in a 300 kV Tandetron at the Ion Implantation Laboratory at UFRGS with target fluences of  $5 \times 10^{16}$  Pt<sup>+</sup> ions/cm<sup>2</sup> and  $1 \times 10^{17}$  Pt<sup>+</sup> ions/cm<sup>2</sup>. Both fluences are high enough to amorphize the near-surface region of the implanted sapphire. Higher fluences at the same implantation energy increases the local sub-surface density of the implanted species and decreases the diffusion distances required for the formation of nanoparticles and was expected to result in a higher density of nanoparticles. The implantation energy was expected to result in a peak density of Pt at 94.1 nm below the Al<sub>2</sub>O<sub>3</sub> surface, based on calculations performed with the Stopping and Range of Ions in Matter software (SRIM) [32]. Rutherford backscattering spectrometry (RBS) was used to characterize the depth of the implanted Pt and to verify the implantation fluences in the two as-implanted wafers. RBS measurements were performed at the Ion Implantation Laboratory at UFRGS using 1 MeV He<sup>+</sup> ions and the backscattered ions were detected by a surface barrier detector. RUMP software (version 2.0) [33, 34] was used to analyze the RBS data and calculate the depth distribution of Pt atoms and implantation fluence. A piece of each of the implanted wafers was annealed at 800°C for 500 h in air with the goal of forming  $\gamma$ -alumina with well-defined Pt nanoparticles. An annealing temperature of 800°C was chosen as the highest temperature expected to induce crystallization to  $\gamma$ -alumina without transition to  $\delta$ -alumina [10, 13]. XRD was used to characterize changes in near-surface crystal structure caused by implantation and subsequent thermal annealing. A Bruker AXS-D8 Discover diffractometer using Cu K $\alpha$  radiation

(wavelength 0.15406 nm) was used for  $\theta$ - $2\theta$  scans from 10-100° ( $2\theta$ ) at a scanning rate of 5°/min. After XRD, specimens were prepared for TEM by mechanically thinning of glued cross sections to  $\sim 100\mu\text{m}$ , polishing on side to 0.25  $\mu\text{m}$  grit, then dimpling and polishing the other side to a 0.25  $\mu\text{m}$  grit finish, followed by  $\text{Ar}^+$  milling to perforation. An FEI Titan TEM operated at 200 keV was used to collect bright-field (BF) and dark-field (DF) images and selected area electron diffraction (SAED) patterns. An image-corrected FEI Titan operated at 300 keV was used for high-resolution TEM (HRTEM) imaging. The TEAM I at the National Center for Electron Microscopy Facility of the Molecular Foundry at Lawrence Berkeley National Lab was operated at 300keV to collect probe-corrected high-angle annular dark field (HAADF) scanning TEM (STEM) data.

RBS was performed at five points across the wafer that had a nominal target fluence of  $1 \times 10^{17} \text{Pt}^+/\text{cm}^2$ . The measured Pt fluence varied from a peak of  $2 \times 10^{17} \text{Pt}/\text{cm}^2$  at the center of the wafer to  $0.8 \times 10^{17} \text{Pt}/\text{cm}^2$ , 10 mm away, near the edge of the wafer. The concentration profile of Pt as a function of depth was determined with RBS on the as-implanted wafer with a target fluence of  $1 \times 10^{17} \text{Pt}^+/\text{cm}^2$ . The RBS spectrum is shown in

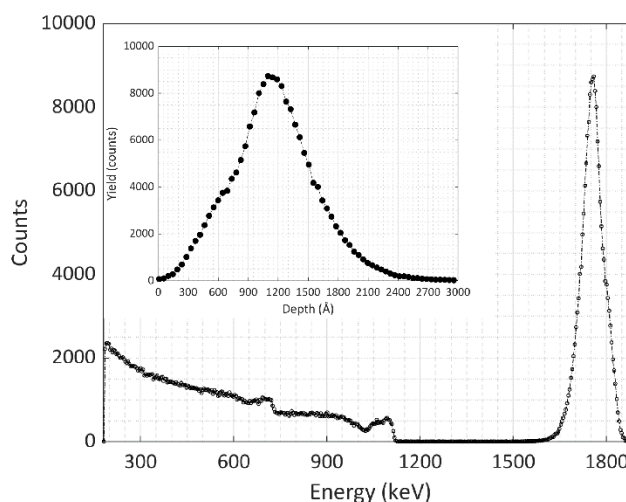


Figure 11 RBS spectrum of  $1 \times 10^{17} \text{Pt}/\text{cm}^2$  wafers

*RBS spectrum. used to determine the depth and Pt fluence in the sapphire wafer with a target fluence of  $1 \times 10^{17} \text{Pt}/\text{cm}^2$  before thermal treatment. The peak concentration of Pt occurred a depth of 110 nm and fluence was found to vary over the wafer, ranging between  $0.8$  and  $2 \times 10^{17} \text{Pt}^+/\text{cm}^2$*

Figure 11 and the inset shows the peak concentration was 110 nm below the wafer surface. XRD of the as-implanted specimen with nominally  $1 \times 10^{17} \text{ Pt}^+/\text{cm}^2$  Figure 12(a) shows prominent peaks at  $2\theta=41.8^\circ$  and  $90.8^\circ$ , consistent with  $(0006)_\alpha$  and  $(000.12)_\alpha$  of  $\alpha$ -alumina expected from the bulk of the sapphire wafer. There are small peaks at  $39.6^\circ$  and  $85.2^\circ$  in the as-implanted specimen, which show a large increase in relative intensity with respect to the  $\alpha$ -alumina peaks after 500 h at  $800^\circ\text{C}$  along with broadening of the peak at  $2\theta=85^\circ$  Figure 12(b). The observed peaks (and

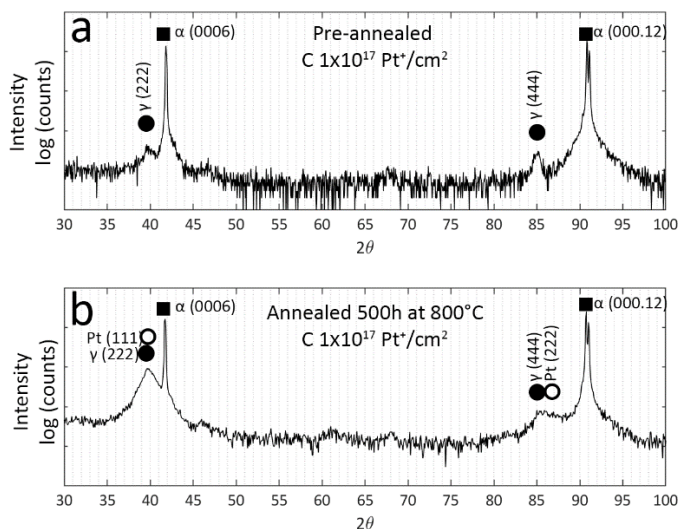


Figure 12 XRD of sapphire wafers implanted with  $1 \times 10^{17} \text{ Pt cm}^{-2}$

*XRD of sapphire wafers after implantation but before annealing (a) showing intense  $\alpha$ - $\text{Al}_2\text{O}_3$  peaks and broad, weak peaks likely due to a transition alumina formed by implantation damage to the matrix. After 500 h at  $800^\circ\text{C}$  (b), peaks consistent with Pt and a transition alumina are visible. The lack of other peaks is evidence of highly oriented growth of transition alumina and the consistent orientation of the Pt nanoparticles within the alumina. Identification of Pt and  $\gamma$ -alumina peaks is based on additional information from TEM imaging and diffraction.*

notable absence of others) are consistent with the development of  $\gamma$ -alumina and the precipitation of Pt with a well-defined in-plane orientation relative to the sapphire matrix. The  $(222)_\gamma$  and  $(111)_{\text{Pt}}$  peaks are expected at  $2\theta = 39.4^\circ$  and  $39.8^\circ$ , respectively, and the  $(444)_\gamma$  and  $(222)_{\text{Pt}}$  peaks are expected at  $85.0^\circ$  and  $85.7^\circ$ , respectively. These peaks indicate  $\{111\}_{\text{Pt}}$  and  $\{222\}_\gamma$  planes are parallel to  $(0006)_\alpha$  planes of the sapphire, but does not exclude other orientations that may not be detected in XRD if they present only at a very small phase fraction. Because of the similarity between transition phases of alumina, the presence of other forms cannot be excluded based on

these XRD data. The assignment of the  $\gamma$ -alumina and Pt peaks in Figure 12 was made using additional information derived from the TEM experiments described below.

TEM was used to characterize changes in the microstructure and the crystal structure with processing and to characterize the Pt-alumina orientation relationships and Pt nanoparticle morphology. Figure 13a shows a cross section of a sapphire wafer as-implanted with  $5 \times 10^{16}$  Pt<sup>+</sup>/cm<sup>2</sup>. A nearly featureless,  $133 \pm 8$  nm thick amorphous layer lies beneath an  $86 \pm 3$  nm thick damaged  $\alpha$ -alumina with the highest density of Pt at  $\sim 110$  nm beneath the surface, in agreement with RBS data, and located within the amorphized layer of alumina. SRIM calculations, predict a peak concentration at a depth of only 94 nm, but this small discrepancy is not unexpected as the accuracy for predicting the stopping power of compound materials, such as aluminum oxide, are limited, as SRIM does not capture the change in the strength of interactions in the compound [32].

A BF zone-axis image (Figure 13b) after 500 h at 800°C shows dark Pt nanoparticles that have developed within the re-crystallized alumina in the implanted region. Most Pt nanoparticles are within the  $\gamma$ -alumina because the peak Pt density from implantation was within the amorphous region. However, annealing also caused growth  $\alpha$ -Al<sub>2</sub>O<sub>3</sub> into the  $\gamma$ -alumina. The  $\alpha$ -Al<sub>2</sub>O<sub>3</sub> grows past some Pt particles, which appear to have been dragged with the boundary. This process leaves some nanoparticles within the  $\alpha$ -Al<sub>2</sub>O<sub>3</sub> and some decorating the  $\alpha/\gamma$ -alumina

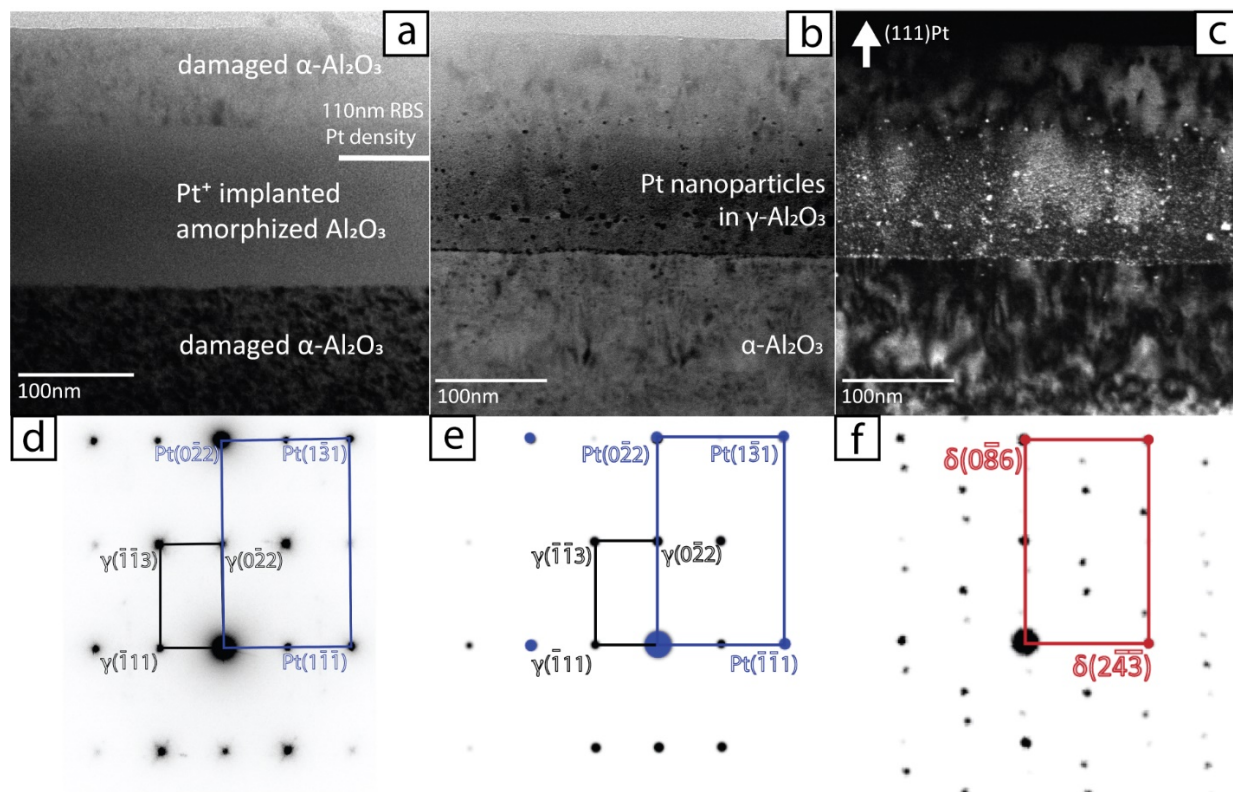


Figure 13 BF TEM images of the  $5 \times 10^{16}$  Pt/cm<sup>2</sup> wafer and simulated diffraction patterns

*BF TEM images of a cross section of (a) the as-implanted  $5 \times 10^{16}$  Pt/cm<sup>2</sup> wafer and (b) after 500 h at 800°C. The sapphire is amorphized where the peak density of implanted Pt occurs. After 500 h at 800°C (b), the amorphous alumina has recrystallized as  $\gamma$ -alumina and the  $\alpha$ -alumina has grown into the region that had been amorphized. Most of the precipitates are near the peak of the implanted Pt density, but they also decorate the  $\gamma/\alpha$ -alumina boundary. (c) DF image of the region in (b) taken in a two-beam condition from  $(111)_{Pt}$  and  $(222)_{\gamma}$ ; the smallest objective aperture could not exclude the  $(0006)_{\alpha}$  diffracted beam. The DF image highlights the high degree of alignment of the Pt within the  $\gamma$ -alumina and of  $\gamma$ -alumina with the  $\alpha$  phase. Experimental SAED pattern (d) of the implanted region after annealing at 800°C for 500h; the adjacent sapphire was excluded with the selected area aperture. The intensities were inverted for clarity. Simulated SAED patterns of (e) Pt and  $\gamma$ -alumina along the  $[211]$  zone axes, using the Zhou and Snyder model [12] and (f) of  $\delta$ -alumina using a structure reported by Kovarik et al. [17] along the  $[35.9.12]_{\delta}$  zone axis where  $(\bar{2}43)_{\delta}$  is equivalent to  $(\bar{1}11)_{\gamma}$  (parallel to close-packed planes of the oxygen sub-lattice) and  $(0\bar{4}3)_{\delta}$  is to  $(0\bar{2}2)_{\gamma}$ .*

boundary, similar to the microstructural development of Pt-implanted  $\alpha$ -Al<sub>2</sub>O<sub>3</sub> annealed at 1000°C, except in that case the transition form of the oxide is  $\theta$ -alumina [25-27].

SAED was used to confirm the identity of transition alumina and to determine the prevalent orientation relationships between the phases. A two-beam DF image (Figure 13c) was taken of the region using the overlapping 111<sub>Pt</sub> and 222 <sub>$\gamma$</sub>  diffracted beams and shows that nearly all Pt particles in the  $\gamma$ -alumina matrix are oriented with (111)<sub>Pt</sub>||((222) <sub>$\gamma$</sub> , confirming that the in-plane orientation determined by XRD is prevalent. Figure 13d shows a typical SAED from the implanted region of a specimen after annealing at 800°C for 500 h. A simulated SAED [211] zone axis pattern for both Pt and the Zhou and Snyder  $\gamma$ -alumina model is shown in Figure 13e and is an excellent match to the experimental pattern. This may reflect the fact that the diffraction information is derived from many cubic nanometers of the  $\gamma$ -alumina – higher resolution structural characterization may be required to reveal the tetragonal symmetry that is predicted by the work of Paglia and coworkers [17, 19]. Based on reports on the alumina transition series [10, 11], the processing path used here could plausibly result in  $\delta$ -alumina, however TEM imaging and diffraction observations of these specimens differ substantially from other TEM characterization of  $\delta$ -alumina [11, 21, 22]. As an example, a simulated pattern of  $\delta$ -alumina, based on a structure from reference [22], shown down an equivalent zone axis to [211] <sub>$\gamma$</sub>  in Figure 13f shows expected diffraction intensity absent in Figure 13d. This and other observations exclude  $\delta$ -alumina as the transition phase in our specimens Figure 13d allows the prevalent orientation relationship between the Pt particles and  $\gamma$ -alumina to be fully determined as (111)<sub>Pt</sub>||((111) <sub>$\gamma$</sub> ;[1 $\bar{1}$ 0] <sub>$\gamma$</sub> ||[1 $\bar{1}$ 0]<sub>Pt</sub>, a “cube-on-cube” orientation.

Phase-contrast HRTEM was used to characterize the morphology and the faceted interfaces

of the Pt nanoparticles in a specimen from the wafer with the higher density of nanoparticles ( $1 \times 10^{17} \text{ Pt}^+/\text{cm}^2$ , annealed 500 h at  $800^\circ\text{C}$ ). Figure 14a shows an atomic resolution micrograph of Pt nanoparticles in a  $\gamma$ -alumina matrix with the underlying  $\alpha$ -alumina. Insets in Figure 14a show fast Fourier transforms (FFTs) of image regions with Pt nanoparticles in  $\gamma$ -alumina (region 1) and the  $\alpha$ -alumina (region 2) revealing the orientation relationships of the phases. The  $\gamma$ -alumina forms with the orientation  $(0006)_\alpha \parallel (111)_\gamma; [10\bar{1}0]_\alpha \parallel [110]_\gamma$ , which results in parallel alignment of close-packed planes of the oxygen sub-lattice in each of the phases as well as alignment of the close-packed oxygen directions within those planes at the interfaces. Epitaxial growth of  $\gamma$ -alumina on  $\alpha$ -alumina has been documented after thermal annealing of  $\alpha$ -alumina that had been partially amorphized by high-energy ion bombardment of various species [3, 28]. The Pt particles have the orientation  $(111)_{\text{Pt}} \parallel (111)_\gamma; [1\bar{1}0]_\gamma \parallel [1\bar{1}0]_{\text{Pt}}$  (as in the specimen with lower fluence) and many appear to be in the form of tetrahedra or truncated tetrahedra bound by  $\{111\}$  facets. The morphology of the nanoparticles was surveyed in HRTEM images of more than 30 particles. All the Pt nanoparticles showed prominent  $\{111\}$  facets, although some also presented small  $\{002\}$  facets.

The three-dimensional (3D) morphology of Pt nanoparticles may be more easily inferred from HAADF STEM image because image intensity is more directly related to scattering potential and the intensity of the Pt positions is roughly proportional to the number of Pt in the columns. The near tetrahedral form of small Pt nanoparticles can be inferred in atomic resolution HAADF STEM images (Figure 14b). A schematic of the morphology of a perfect tetrahedral nanoparticle is shown in the inset of Figure 14b. The smallest particles (one's containing  $\sim 100$  Pt atoms) tend toward a defective tetrahedral shape rather than a cubo-octahedral, with symmetric

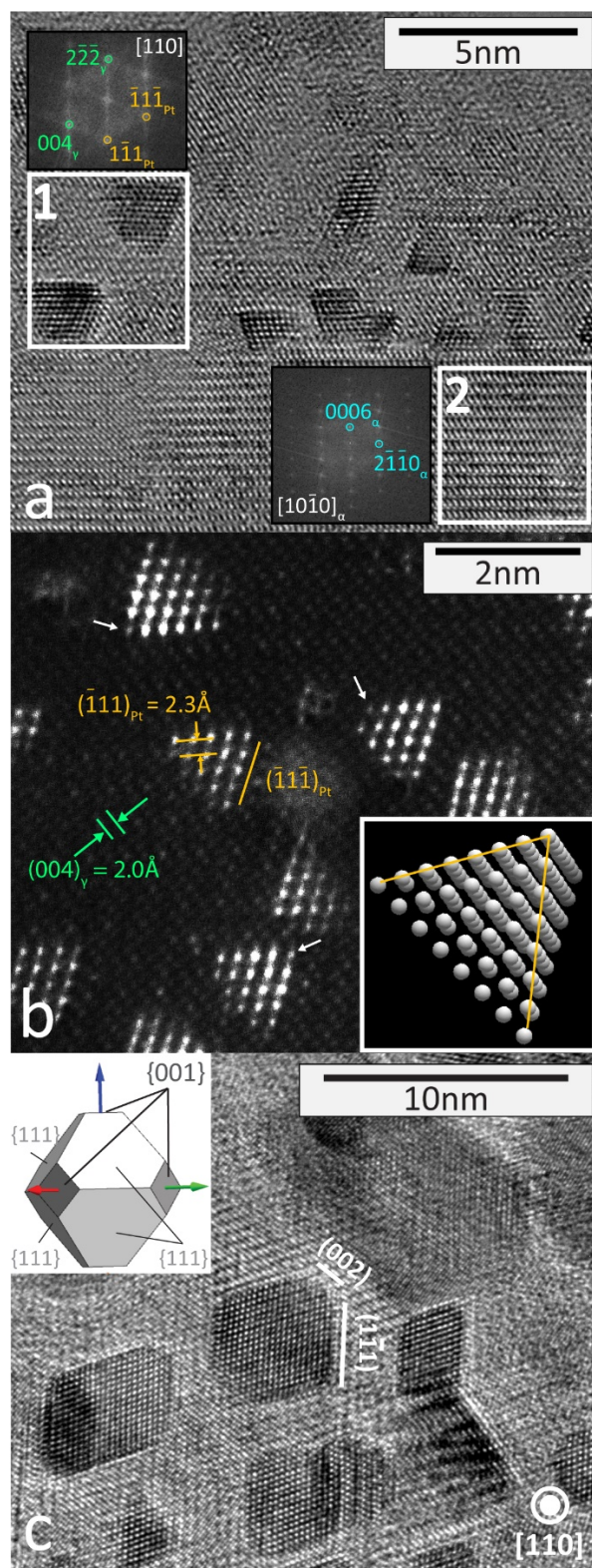


Figure 14 Aberration-corrected phase-contrast HRTEM

*Aberration-corrected phase-contrast HRTEM (a,c) and probe-corrected HAADF STEM (b) micrographs of the  $1 \times 10^{17}$  Pt/cm<sup>2</sup> implanted wafer after 800°C at 500 h. The FFT of region 1 in (a) is consistent with the cube-on-cube orientation between Pt and  $\gamma$ -alumina. The FFT of region 2 shows that  $\gamma$ -alumina crystallizes epitaxially from the  $\alpha$ -alumina with the orientation  $(0001)_\alpha || (111)_\gamma$ ;  $[10\bar{1}0]_\alpha || [110]_\gamma$ . The 3D morphology of Pt nanoparticles may be more easily inferred from the HAADF STEM image. The inset shows a model of a perfect tetrahedral Pt nanoparticle bound by {111} facets tilted slightly off the [110] zone axis; the low intensity at the corners of the nanoparticles in the STEM images indicate “missing” corner and edge atoms (indicated by white arrows) which are not shown in the model. Larger Pt nanoparticles (c) tend to be cubo-octohedral rather than tetrahedral. A 3-D model is shown in the inset [35].*

{111} facets and {200} facets. The larger particles, which have not converged onto a single shape, are more likely to be cubo-octahedral in shape, as shown in the HRTEM image in Figure 14c. The equilibrium shape is expected to be independent of size for large particles, but for small particles (<20 nm), the edge energies can be a significant contribution to the total interfacial energy, resulting in changes in the equilibrium shape as a function of size [36, 37]. Additionally, strain energy may impact the morphology of precipitates as a function of size [38, 39]. At this point, it is unclear if the difference in morphology of large and small nanoparticles is simply due to a lack of convergence of the larger particles onto a tetrahedral form, or if it is due to different relative contributions of strain, interfacial, and edge energies related to the nanoparticle size.

Orientation and interfacial relationships that develop during precipitation into a solid matrix and onto surfaces can differ because the strain and interfacial energetic contributions with 3D constraints on differ from the two-dimensional constraints on supported particles [40]. However, common interfacial orientation may still develop, which is the case for Pt and  $\gamma$ -alumina. Zhang *et al.* [41] reported that Pt nanoparticles supported on (111)  $\gamma$ -alumina surfaces, formed by oxidation of (110) NiAl single crystals, took on two orientations. One interfacial relationship was the “cube-on-cube” orientation observed here, the other was  $\text{Pt}(100)[011] \parallel \gamma\text{-Al}_2\text{O}_3(111)[211]$ , which was not observed in this study. The common  $(111)_{\text{Pt}} \parallel (111)_{\gamma}; [1\bar{1}0]_{\gamma} \parallel [1\bar{1}0]_{\text{Pt}}$  interface is the focus of current atomic-resolution characterization.

Ion implantation followed by thermal annealing has been used to synthesize transition aluminas, including ones with embedded metal nanoparticles, but the method has not seen its full potential in the study of the interfacial structure of systems that are important for catalysis. Although the processing path differs from those used to produce supported industrial catalysts, it offers a high degree of control over the purity of the system and allows the system to access

degrees of freedom in the formation of interfacial relationships that are not possible with processing methods that entail deposition of Pt or a Pt-containing precursor on  $\gamma$ -alumina. Use of a processing path where the Pt precipitates into alumina as it crystallizes removes the biasing effect of a pre-existing  $\gamma$ -alumina surface structure by removing pre-existing surface orientations.

Although diffusion in alumina is expected to be sluggish at the processing temperature used here, Pt precipitates with atomically sharp interfaces several nanometers across were formed in experimentally accessible times, when high ion implantation fluences were used. With a larger survey of nanoparticles, this model system provides a means to compare the relative contributions of edge energy [36, 37], strain [38, 39], and interfacial chemistry on the energetics of the system. The interfacial energies for different chemical terminations of the  $\{111\}$  faceted interfaces have been calculated [42], guided by the experimental observation of the interfaces here, but further data is needed on  $\{200\}$  interfaces and edge energies.

### Chapter 3 References

- [1] A. Meldrum, R. F. Haglund, L. A. Boatner, and C. W. White, "Nanocomposite materials formed by ion implantation," *Advanced Materials*, vol. 13, no. 19, pp. 1431-1444, Oct 2001, doi: 10.1002/1521-4095(200110)13:19<1431::Aid-adma1431>3.0.Co;2-z.
- [2] P. Normand *et al.*, "Nanocrystals manufacturing by ultra-low-energy ion-beam-synthesis for non-volatile memory applications," *Nuclear Instruments & Methods in Physics Research Section B-Beam Interactions with Materials and Atoms*, vol. 216, pp. 228-238, Feb 2004, doi: 10.1016/j.nimb.2003.11.039.
- [3] J. D. Budai, C. W. White, S. P. Withrow, M. F. Chisholm, J. Zhu, and R. A. Zuhr, "Controlling the size, structure and orientation of semiconductor nanocrystals using metastable phase recrystallization," *Nature*, vol. 390, no. 6658, pp. 384-386, 1997, doi: 10.1038/37079.
- [4] C. W. White *et al.*, "Ferromagnetic FePt nanoparticles formed in Al<sub>2</sub>O<sub>3</sub> by ion implantation," *Nuclear Instruments & Methods B*, Article vol. 191, pp. 437-441, May 2002. [Online]. Available: <Go to ISI>://000176692300085
- [5] M. K. Santala, V. Radmilovic, R. Giulian, M. C. Ridgway, R. Gronsky, and A. M. Glaeser, "The orientation and morphology of platinum precipitates in sapphire," *Acta Materialia*, vol. 59, no. 12, pp. 4761-4774, Jul 2011, doi: 10.1016/j.actamat.2011.04.012.
- [6] M. Trueba and S. P. Trasatti, "Gamma-alumina as a support for catalysts: A review of fundamental aspects," *European Journal of Inorganic Chemistry*, no. 17, pp. 3393-3403, Sep 2005, doi: 10.1002/ejic.200500348.
- [7] G. Ertl, H. Knözinger, and J. Weitkamp, *The Handbook of Heterogeneous Catalysis*. Weinheim: Wiley-VCH, 1997.
- [8] A. Ionescu, A. Allouche, J. P. Aycard, M. Rajzmann, and F. Hutschka, "Study of gamma-alumina surface reactivity: Adsorption of water and hydrogen sulfide on octahedral aluminum sites," *Journal of Physical Chemistry B*, vol. 106, no. 36, pp. 9359-9366, Sep 2002, doi: 10.1021/jp020145n.
- [9] J. C. Vedrine, "Heterogeneous Catalysis on Metal Oxides," *Catalysts*, vol. 7, no. 11, Nov 2017, Art no. 341, doi: 10.3390/catal7110341.
- [10] K. Wefers and C. Misra, "Oxides and Hydroxides of Aluminum: Alcoa Technical Paper No. 19, Revised " Alcoa Laboratories, 19, 1987.
- [11] I. Levin and D. Brandon, "Metastable alumina polymorphs: Crystal structures and transition sequences," *Journal of the American Ceramic Society*, vol. 81, no. 8, pp. 1995-2012, Aug 1998. [Online]. Available: <Go to ISI>://WOS:000075368600002.
- [12] R. S. Zhou and R. L. Snyder, "Structures and transformation mechanisms of the eta, gamma and theta transition aluminas," *Acta Crystallographica Section B-Structural Science*, Article vol. 47, pp. 617-630, Oct 1991. [Online]. Available: <Go to ISI>://A1991GL01200006
- [13] C. Pecharrroman, I. Sobrados, J. E. Iglesias, T. Gonzalez-Carreno, and J. Sanz, "Thermal evolution of transitional aluminas followed by NMR and IR spectroscopies," *Journal of Physical Chemistry B*, vol. 103, no. 30, pp. 6160-6170, Jul 29 1999, doi: 10.1021/jp983316q.
- [14] L. Samain *et al.*, "Structural analysis of highly porous gamma-Al<sub>2</sub>O<sub>3</sub>," *Journal of Solid State Chemistry*, vol. 217, pp. 1-8, Sep 2014, doi: 10.1016/j.jssc.2014.05.004.
- [15] C. Wolverton and K. C. Hass, "Phase stability and structure of spinel-based transition aluminas," *Phys. Rev. B*, Article vol. 6302, no. 2, p. 024102, Jan 2001. [Online]. Available: <Go to ISI>://000166382200013

- [16] M. Digne, P. Sautet, P. Raybaud, P. Euzen, and H. Toulhoat, "Hydroxyl groups on gamma-alumina surfaces: A DFT study," *Journal of Catalysis*, vol. 211, no. 1, pp. 1-5, Oct 2002, doi: 10.1006/jcat.2002.3741.
- [17] G. Paglia *et al.*, "Tetragonal structure model for boehmite-derived gamma-alumina," *Phys. Rev. B*, vol. 68, no. 14, Oct 2003, Art no. 144110, doi: 10.1103/PhysRevB.68.144110.
- [18] M. Digne, P. Sautet, P. Raybaud, P. Euzen, and H. Toulhoat, "Use of DFT to achieve a rational understanding of acid-basic properties of gamma-alumina surfaces," *Journal of Catalysis*, vol. 226, no. 1, pp. 54-68, Aug 2004, doi: 10.1016/j.jcat.2004.04.020.
- [19] G. Paglia, A. L. Rohl, C. E. Buckley, and J. D. Gale, "Determination of the structure of gamma-alumina from interatomic potential and first-principles calculations: The requirement of significant numbers of nonspinel positions to achieve an accurate structural model," *Phys. Rev. B*, vol. 71, no. 22, Jun 2005, Art no. 224115, doi: 10.1103/PhysRevB.71.224115.
- [20] K. J. Morrissey, K. K. Czanderna, R. P. Merrill, and C. B. Carter, "Transition alumina structures studied using HREM," (in English), *Ultramicroscopy*, Article vol. 18, no. 1-4, pp. 379-385, 1985, doi: 10.1016/0304-3991(85)90156-1.
- [21] I. Levin, T. Gemming, and D. G. Brandon, "Some metastable polymorphs and transient stages of transformation in alumina," *Phys. Status Solidi A-Appl. Res.*, Article vol. 166, no. 1, pp. 197-218, Mar 1998. [Online]. Available: <Go to ISI>://000072976500019
- [22] L. Kovarik, M. Bowden, A. Genc, J. Szanyi, C. H. F. Peden, and J. H. Kwak, "Structure of delta-Alumina: Toward the Atomic Level Understanding of Transition Alumina Phases," *Journal of Physical Chemistry C*, vol. 118, no. 31, pp. 18051-18058, Aug 7 2014, doi: 10.1021/jp500051j.
- [23] L. Kovarik *et al.*, "Unraveling the Origin of Structural Disorder in High Temperature Transition Al<sub>2</sub>O<sub>3</sub>: Structure of theta-Al<sub>2</sub>O<sub>3</sub>," *Chemistry of Materials*, vol. 27, no. 20, pp. 7042-7049, Oct 2015, doi: 10.1021/acs.chemmater.5b02523.
- [24] L. Kovarik *et al.*, "Tomography and High-Resolution Electron Microscopy Study of Surfaces and Porosity in a Plate-like gamma-Al<sub>2</sub>O<sub>3</sub>," *Journal of Physical Chemistry C*, vol. 117, no. 1, pp. 179-186, Jan 2013, doi: 10.1021/jp306800h.
- [25] M. K. Santala, V. Radmilovic, R. Giulian, M. C. Ridgway, A. M. Glaeser, and R. Gronsky, "Precipitate orientation relationships in Pt-implanted sapphire," *Scr. Mater.*, vol. 62, no. 4, pp. 187-190, Feb 2010, doi: 10.1016/j.scriptamat.2009.10.023.
- [26] M. K. Santala, "On Orientation Relationships and Morphologies of Platinum Precipitates in Sapphire," Ph.D., Materials Science and Engineering, University of California, Berkeley, 2009.
- [27] M. Gandman, M. Ridgway, R. Gronsky, and A. M. Glaeser, "Microstructural evolution in Pt-implanted polycrystalline Al<sub>2</sub>O<sub>3</sub>," *Acta Materialia*, vol. 83, pp. 169-179, Jan 2015, doi: 10.1016/j.actamat.2014.09.045.
- [28] N. Yu, P. C. McIntyre, M. Nastasi, and K. E. Sickafus, "High-quality epitaxial growth of  $\gamma$ -alumina films on  $\alpha$ -alumina sapphire induced by ion-beam bombardment," *Phys. Rev. B*, vol. 52, no. 24, pp. 17518-17522, Dec 15 1995, doi: 10.1103/PhysRevB.52.17518.
- [29] C. W. White, C. J. McHargue, P. S. Sklad, L. A. Boatner, and G. C. Farlow, "Ion implantation and annealing of crystalline oxides," *Material Science Reports*, vol. 4, no. 2-3, pp. 41-146, July 1989, doi: 10.1016/s0920-2307(89)80005-2.
- [30] E. Alves, R. C. da Silva, O. Conde, M. F. da Silva, and J. C. Soares, "Formation of coherent precipitates of platinum in sapphire," *Nuclear Instruments & Methods B*, Article vol. 148, no. 1-4, pp. 1049-1053, Jan 1999. [Online]. Available: <Go to ISI>://000078575700196

- [31] C. W. White *et al.*, "Oriented ferromagnetic Fe-Pt alloy nanoparticles produced in Al<sub>2</sub>O<sub>3</sub> by ion-beam synthesis," *Journal of Applied Physics*, vol. 93, no. 9, pp. 5656-5669, 2003, doi: 10.1063/1.1565691.
- [32] J. F. Ziegler, M. D. Ziegler, and J. P. Biersack, "SRIM - The stopping and range of ions in matter (2010)," *Nuclear Instruments & Methods in Physics Research Section B-Beam Interactions with Materials and Atoms*, vol. 268, no. 11-12, pp. 1818-1823, Jun 2010, doi: 10.1016/j.nimb.2010.02.091.
- [33] L. R. Doolittle, "ALGORITHMS FOR THE RAPID SIMULATION OF RUTHERFORD BACKSCATTERING SPECTRA," (in English), *Nuclear Instruments & Methods in Physics Research Section B-Beam Interactions with Materials and Atoms*, Letter vol. 9, no. 3, pp. 344-351, 1985, doi: 10.1016/0168-583x(85)90762-1.
- [34] N. P. Barradas *et al.*, "International Atomic Energy Agency intercomparison of ion beam analysis software," *Nuclear Instruments & Methods in Physics Research Section B-Beam Interactions with Materials and Atoms*, vol. 262, no. 2, pp. 281-303, Sep 2007, doi: 10.1016/j.nimb.2007.05.018.
- [35] R. V. Zucker, D. Chatain, U. Dahmen, S. Hagege, and W. C. Carter, "New software tools for the calculation and display of isolated and attached interfacial-energy minimizing particle shapes," *Journal of Materials Science*, vol. 47, no. 24, pp. 8290-8302, Dec 2012, doi: 10.1007/s10853-012-6739-x.
- [36] L. D. Marks, "Particle-Size Effects on Wulff Constructions," *Surface Science*, Article vol. 150, no. 2, pp. 358-366, 1985. [Online]. Available: <Go to ISI>://A1985ADW0900007
- [37] L. D. Marks, "Experimental studies of small-particle structures," *Reports on Progress in Physics*, vol. 57, no. 6, pp. 603-649, Jun 1994, doi: 10.1088/0034-4885/57/6/002.
- [38] U. Dahmen, S. Q. Xiao, S. Paciornik, E. Johnson, and A. Johansen, "Magic-size equilibrium shapes of nanoscale Pb inclusions in Al," *Physical Review Letters*, Article vol. 78, no. 3, pp. 471-474, Jan 1997. [Online]. Available: <Go to ISI>://A1997WC79800019
- [39] M. E. Thompson, C. S. Su, and P. W. Voorhees, "The Equilibrium Shape of a Misfitting Precipitate," *Acta Metall. Mater.*, vol. 42, no. 6, pp. 2107-2122, Jun 1994. [Online]. Available: <Go to ISI>://A1994NM40100034
- [40] P. Wynblatt and D. Chatain, "Two-dimensional versus three-dimensional constraints in hetero-epitaxy/orientation relationships," *Journal of Materials Science*, vol. 52, no. 16, pp. 9630-9639, Aug 2017, doi: 10.1007/s10853-017-1145-z.
- [41] Z. Zhang, L. Li, and J. C. Yang, "Adhesion of Pt Nanoparticles Supported on gamma-Al<sub>2</sub>O<sub>3</sub> Single Crystal," *Journal of Physical Chemistry C*, vol. 117, no. 41, pp. 21407-21412, Oct 17 2013, doi: 10.1021/jp407798b.
- [42] K. Oware Sarfo, A. L. Clauser, M. K. Santala, and L. Árnadóttir, "Ab initio study of the stability and electronic structure of Pt/gamma-Al<sub>2</sub>O<sub>3</sub> interfaces using density functional theory," *Appl. Surf. Sci.*, submitted 2020, in review.

#### **4. Characterization of the atomic -level structure of (111) Pt/ $\gamma$ -alumina interfaces**

(manuscript in preparation for submission to *Acta Materialia*)

A.L. Clauser,<sup>a</sup> K. Oware Sarfo,<sup>b</sup> C. Ophus,<sup>c</sup> J. Ciston,<sup>c</sup> L. Árnadóttir,<sup>b</sup> and M.K. Santala<sup>a</sup>

<sup>a</sup>*School of Mechanical, Industrial, and Manufacturing Engineering, Oregon State University, Corvallis, OR, USA*

<sup>b</sup>*School of Chemical, Biological, and Environmental Engineering, Oregon State University, Corvallis, OR, United States*

<sup>c</sup>*National Center for Electron Microscopy, Molecular Foundry, Lawrence Berkeley National Laboratory, Berkeley, CA, United States*

##### **Abstract**

The interface of  $\gamma$ -alumina supported Pt nanoparticles (NPs) is fundamentally important to the efficacy of this metal/metal oxide system in catalysis. Here, (111) Pt/  $\gamma$ -alumina interfaces are characterized in a model system produced by high-energy implantation of Pt<sup>+</sup> ions into sapphire that was thermally treated at 800°C to produce a surface layer of dense  $\gamma$ -alumina embedded with faceted Pt NPs. Aberration-corrected STEM was used to collect atomic resolution brightfield (BF) and high-angle annular darkfield (HAADF) images down the [110]<sub>Pt</sub> and [211]<sub>Pt</sub> zone-axis. The images were compared to STEM simulations of two popular experimentally-based bulk models of  $\gamma$ -alumina by Smrčok et al. and Zhou and Snyder and a density functional theory-based model of the (111) interface recently published by Oware Sarfo and coworkers. The Smrčok  $\gamma$ -alumina model was a better fit than the Zhou structure to the bulk of the  $\gamma$ -alumina. The Oware Sarfo interfacial model that best fit the experimental data was oxygen-terminated with an atomic arrangement at the interface of NPs that consists of Pt-O-Al<sub>oct</sub>-O layers. The Oware Sarfo structure was a relatively poor fit to the experimental data beyond the third atomic layer from the interface in the  $\gamma$ -alumina. The poor fit of the Oware Sarfo model within the bulk is attributed to the compromises required in the design of the model in order to limit the cell size to limit computational time required.

## 4.1. Introduction

Pt nanoparticles (NPs) supported by transition  $\gamma$ -alumina are a catalytic system used in many applications, including methane combustion microreactor coatings, the production of high octane gasoline from linear alkanes, and CO chemisorption [1-4]. The metal-oxide interfacial interactions impact many of the important qualities of this system, for example, the Pt NP size and morphology can affect the activity and reaction rate of catalysts used in CO electro-oxidation [5] and strong metal-support interactions are necessary to sustain high activity catalysis under operating conditions [6].

Because of its technological importance, the structure of the Pt/ $\gamma$ -alumina system has been extensively studied [7-11], including transmission electron microscopy (TEM) studies of Pt NPs supported by  $\gamma$ -alumina [6, 12-14]. Past TEM imaging studies have not resolved the atomic-level structure of the interfaces, but electron energy loss spectroscopy (EELS) along with scanning transmission electron microscopy (STEM) imaging have been employed to characterize the bonding at the interfaces [6-9]. Some of these studies cited beam damage as an issue to be managed in this type of experiment, as transition aluminas can recrystallize during electron microscopy and the thin areas ideal for atomic resolution microscopy quickly become damaged. Spectroscopic methods like EELS can be used to generate structural and chemical data in the TEM with probe sizes as small as 0.1 nm, fine enough for atomic resolution analysis. However, knowledge of bonding data does not necessarily imply knowledge of the spatial structure. Neutron magnetic resonance and x-ray absorption spectroscopy has been used to probe this system [6, 15]. These techniques provide averaged structural data, which provide only partial structural information, especially in a system containing  $\gamma$ -alumina which is known to have disordered occupancy of atomic sites.

In this work, Pt/ $\gamma$ -alumina interfaces in a model nanocomposite system were imaged at atomic resolution using aberration-corrected STEM and the experimental images of the  $\gamma$ -alumina and the interfaces were compared to two structural models of  $\gamma$ -alumina and a set of density functional theory (DFT) based interfacial models with different chemical terminations of the  $\gamma$ -alumina. High energy ion implantation was used to generate a metal-oxide nanocomposite material, a concept described by White *et al.* [16] and an approach used to study the structure and orientation of Pt in a variety of alumina phases [17-20]. Ion implantation followed by thermal annealing was used to generate a high density of faceted Pt NPs with a well-defined orientation relationship in a dense  $\gamma$ -alumina matrix. Metal-implanted alumina offers an alternative method to study metal-alumina interfaces; one of the advantages being greater stability of the dense alumina with embedded metal NPs under the electron beam relative to NPs supported on high-surface-area alumina. This model system facilitated atomic resolution imaging of the interfaces and the approach was to compare STEM image simulations of structural models to the experimental images rather than using spectroscopic methods to probe the structure and chemistry of the interfaces.

The  $\gamma$ -alumina phase is a metastable transition phase, which may be formed by a variety of processing methods [21-27]. The precursor affects the character of resulting  $\gamma$ -alumina which has led to a number of proposed models for this oxide. Commercially,  $\gamma$ -alumina is formed when aluminum hydroxides, often boehmite ore (AlOOH), are calcined at 800°C. Boehmite-derived  $\gamma$ -alumina is formed when water is driven out of the structure causing a structural collapse of (001) layers of boehmite [28] and the resulting  $\gamma$ -alumina often has a residual tetragonality inherited from the parent structure [29]. The complexity of  $\gamma$ -alumina and topotactic dependence of its

structure on its precursor means there is still debate over the most appropriate model for  $\gamma$ -alumina.

The transition alumina that develop on the  $\text{AlOOH}/\text{amorphous} \rightarrow \gamma \rightarrow \delta \rightarrow \theta \rightarrow \alpha$ -alumina transformation path progress mainly by rearrangement of Al within the oxygen sublattice. The  $\gamma$  and  $\delta$  variants possess a face-centered cubic (FCC) oxygen sublattice with a spinel-like distribution of Al cations. To maintain the  $\text{Al}_2\text{O}_3$  stoichiometry, only a fraction of the O interstitial sites are occupied by Al. The differences in the distribution of the Al differentiates these transition alumina phases. The  $\gamma$ -alumina phase has been determined to have a 25-30% of the tetrahedral O interstices occupied by Al ( $\text{Al}_t$ ),  $\delta$ -alumina has 37.5% and  $\theta$ -alumina has 50% of the  $\text{Al}_t$  positions occupied [30]. As the processing temperature increases Al migrates from octahedral sites ( $\text{Al}_o$ ) to tetrahedral sites on the FCC O-sublattice. At higher temperatures ( $\sim 1000^\circ\text{C}$ ), monoclinic  $\theta$ - $\text{Al}_2\text{O}_3$  transforms to  $\alpha$ -alumina ( $1100$ - $1200^\circ\text{C}$ ), the most stable form, which has a hexagonal close packed O-sublattice with Al occupying two-thirds of the  $\text{Al}_o$  sites.

#### 4.1.1. Producing NPs in $\gamma$ -alumina via ion implantation

Ion implantation of crystalline oxides followed by thermal annealing is a method that can be used to generate epitaxially grown oxides with embedded nanoparticles [16, 31]. Ion implantation allows for control of precipitate size and particle orientation [32]. This processing method creates an amorphous region near the surface of an implanted wafer which can be re-crystallized and used to study crystallization kinetics [23], NP morphology, and properties of embedded NPs. The temperature required for partially amorphized alumina to crystallize to  $\gamma$ -alumina depends on the crystallinity retained in the wafer and has been characterized at temperatures as low as  $650^\circ\text{C}$ , but  $\gamma$ -alumina can still be present up to  $1000^\circ\text{C}$  [33, 34]. Pt NPs in  $\gamma$ -alumina formed by the high-energy implantation followed by thermal annealing in air at  $1173$

K (800°C) take on the orientation relationship  $(111)_{\text{Pt}} \parallel (111)_{\gamma}$ ;  $[1\bar{1}0]_{\text{Pt}} \parallel [1\bar{1}0]_{\gamma}$  [35]. Small NPs take on nearly tetrahedral shapes bound by  $\{111\}$  facets whereas larger NPs may be cubo-octohedral with large  $\{111\}$  facets and relatively small  $\{200\}$  facets.

#### 4.1.2. Structural Models of $\gamma$ -alumina

Several models for the structure of  $\gamma$ -alumina have been proposed, including a widely-cited defected cubic spinel model by Zhou and Snyder [36], a cubic spinel model by Smrčok *et al.* [37], a widely-used DFT-based non-spinel model by Digne *et al.* [38, 39], a distorted tetragonal spinel by Paglia *et al.* [40] which does not restrict Al cations to spinel positions, and a DFT-based model by Pinto *et al.* was developed to model surface behavior and which also proposed non-spinel cation sites dominated by five-coordinated aluminum and some tetrahedral Al [41], among others. Recent work by Ayoola *et al.* [42] evaluated the Smrčok [37], Paglia [40], Digne [39] and Pinto [41] models of  $\gamma$ -alumina by comparing them to XRD and TEM data of  $\gamma$ -alumina grown from single crystal NiAl (110) wafers. They found the Smrčok model to be the best fit based on comparison of experimental and simulated diffraction data. They did not consider the Zhou model, but it was found to be a good fit to electron diffraction data of  $\gamma$ -alumina derived from the recrystallization of partially amorphized sapphire annealed at 800°C by Clauser *et al.* [35].

The bulk  $\gamma$ -alumina in this study is compared to both the Zhou and Smrčok models, which differ primarily in the positions the Al atoms occupy. Figure 15 and Table 2 shows the unit cells and structural data of the Zhou and Smrčok models. Both models have an FCC oxygen sublattice and a high occupancy of the 8a tetrahedral site. The Smrčok model assumes a higher occupation of Al in the octahedral 16d site than the Zhou model. The Zhou model has a low occupation of quasi-octahedral Al in position 32e, whereas the Smrčok model proposes two sparsely occupied

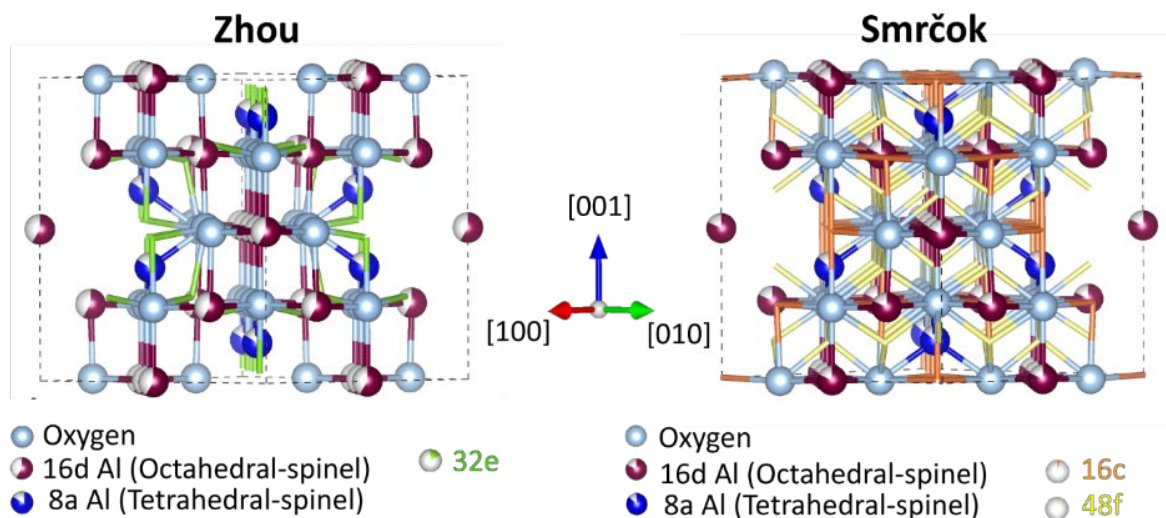


Figure 15 The Zhou and Smrčok models for  $\gamma$ -alumina

*The oxygen in both models forms an FCC sublattice with Al in spinel positions and some non-spinel positions defined by partial occupancies. For clarity, atomic sites with occupancies below 30% percent are not represented as spheres, but instead as colored branches.*

non-spinel octahedral and tetrahedral sites 16c and 48f. The Zhou [36] model is based on the Rietveld refinement of neutron powder diffraction patterns and x-ray powder diffraction of  $\gamma$ -alumina derived from boehmite calcined at 873K (~600°C). The crystal structure is  $Fd\bar{3}m$  structure with a lattice parameter  $a=7.911\text{\AA}$ . The Zhou model consists of two types of alternating (111) aluminum layers within the O-sublattice, one composed of  $Al_o$ , and the other composed of a mixture of  $Al_o$ , quasi-octahedral Al, and  $Al_t$ . Zhou and Snyder found that the  $Al_t$  are disordered through an observation of the broadening of the XRD (220) reflection and that the  $Al_o$  is less disordered than the  $Al_t$  sites. The Smrčok structure was developed from XRD data from  $\gamma$ -alumina whiskers and can be considered a refinement of the Zhou model. The Al occupies ideal spinel positions as well as non-spinel tetrahedral and octahedral positions. There is a 63:37 octahedral to tetrahedral Al atom ratio with 6% of all Al ions occupying non-spinel positions.

Table 2 Atomic positions for the Zhou and Smrčok defected spinel  $\gamma$ -alumina models.

Both models have a high occupancy of tetrahedral site 8a. The Smrčok model has a higher occupation of Al in the octahedral 16d site than the Zhou model. The Zhou model has a low occupation of quasi-octahedral Al in position 32e, whereas the Smrčok model proposes two sparsely occupied non-spinel octahedral and tetrahedral sites 16c and 48f.

Species	Site	Site description	Zhou occupancy	Smrčok occupancy
O	32e	FCC-like sub-lattice	1	1
Al <sub>o</sub>	16d	octahedral	0.58	0.816
Al <sub>t</sub>	8a	tetrahedral	0.84	0.8633
Al	32e	quasi-octahedral	0.17	
Al	16c	non-spinel octahedral		0.028
Al	48f	non-spinel tetrahedral		0.019

#### 4.1.3. Structural Model of the Pt/ $\gamma$ -alumina Interface

There have been many models of single atoms [43, 44] or small clusters of Pt [10, 45, 46] on  $\gamma$ -alumina, but few of extended interfaces [47]. The predominance of the  $\{111\}$  facets observed by Clauser *et al.* was used as guide for a DFT-based study by Oware Sarfo *et al.* [47] of the structure and relative thermodynamic stability of extended Pt/ $\gamma$ -alumina interfaces with the  $(111)_{Pt}|| (111)_{\gamma}$ ;  $[1\bar{1}0]_{\gamma}|| [1\bar{1}0]_{Pt}$  interfacial relationship with different chemical terminations (O, Al, and Al<sub>2</sub>) of the  $\gamma$ -alumina. The O-terminated interface was found to be the most thermodynamically stable at 1173 K and an oxygen partial pressure ( $p_{O_2}$ ) of 0.2, the processing conditions used in [35] and in this work. Here, the Oware Sarfo interface model [47] is compared to experimental atomic-resolution microscopy images through image simulations. The starting point for the  $\gamma$ -alumina in the Oware Sarfo model was the DFT-based model by Digne *et al.* [39], which is monoclinic and is based on a molecular dynamics study by Krokidis *et al.* [28] used to understand the collapse and reconstruction of boehmite ore during calcination. The Digne model was developed for surface studies and used the lowest energy structure of the Krokidis simulation with 25% of Al cations in Al<sub>t</sub> positions. The model is made of eight Al<sub>2</sub>O<sub>3</sub> structural units and is widely used in DFT studies

due to the simplicity of the cell, lack of partial occupancies, and benchmarking against experimental data (of mainly surface sensitive properties).

## 4.2. Experimental

To create a system of  $\gamma$ -alumina with a high density of platinum interfaces, Pt nanoparticles were precipitated in a  $\gamma$ -alumina matrix by annealing single crystal (99.99%) optical grade  $\alpha$ - $\text{Al}_2\text{O}_3$  wafers that had been implanted with  $\text{Pt}^+$  ions at room temperature using 600keV,  $7^\circ$  to normal of the sapphire wafer face. The wafers were cut such that the  $(0001)_\alpha$  is parallel to the face of the wafer. These large faces were then partially amorphized through high-energy ion implantation of nominally  $1 \times 10^{17} \text{ Pt}^+/\text{cm}^2$ . This results in the region just below the wafer surface to become amorphized with a peak distribution of Pt 110 nm below the surface. The wafers were then annealed at  $800^\circ\text{C}$  for 500h in air - long enough to enable a full transition of amorphous alumina to  $\gamma$ -alumina and the formation of faceted Pt NPs [35]. The annealed wafer pieces were prepared for TEM characterization in cross-section by bonding two pieces of wafer together using M-bond 610 epoxy adhesive, sectioning them, thinning sections to 160-180 $\mu\text{m}$  thick, and polishing to a 0.25 $\mu\text{m}$  diamond paste finish on one side. Samples were then dimpled to <20  $\mu\text{m}$  on the other side and polished to a 0.25 $\mu\text{m}$  finish before being ion milled to electron transparency.

STEM data was collected on the TEAM 1 electron microscope, a double probe-corrected FEI Titan at the National Center for Electron Microscopy (NCEM), operated at 300keV. A high angle annular darkfield (HAADF) and a brightfield (BF) detector were used to collect orthogonal, consecutive HAADF/BF image pairs. STEM images were collected along the  $[110]_{\text{Pt}}$  and  $[211]_{\text{Pt}}$  zone axes. Orthogonal image pairs of the interface were used to perform drift

correction to reduce the effect of nonlinear drift in STEM images developed using Matlab code [48].

STEM images based on the Zhou, Smrčok, and the Oware Sarfo Pt/ $\gamma$ -alumina interface models were simulated using Prismatic [49] [50], a software that uses quantum calculations to simulate STEM images, for comparison to experimental images. The Smrčok model used in the simulation and was taken from the .cif file accompanying [37] which differed very slightly from the structure reported in the text of that reference. Experimental images of interfaces were compared to Prismatic image simulations of interfacial platinum and  $\gamma$ -alumina using the Oware-Sarfo model and  $\gamma$ -alumina bulk structures were simulated using the Zhou and Smrčok models with included partial occupancies.

The Zhou and Smrčok structures were simulated using two  $4 \times 4$  constructions of unit cells of  $\gamma$ -alumina with the [110] and [211] directions parallel to the electron beam. The [211] zone axis structure is bound on the sides by {111} and {011} planes and is four-unit cells thick in the [211] directions. The [110] structure is bound by {001} with the {110} facets four-unit cells thick. The Oware Sarfo structures for three different chemical terminations of the (111) Pt/ $\gamma$ -alumina interface were simulated down the [110] and [211] directions. The O-terminated interfacial model used in simulations are shown in Figure 20 and Figure 21. Al<sub>1</sub>-terminated and Al<sub>2</sub> terminated models are shown in Figure S1 in the Appendix. For image simulations, these cells were tiled three-unit cells wide and two-unit cells thick such that the largest interface perpendicular to the z-direction was [110] and [211] respectively.

The imaging conditions for Prismatic simulations were chosen to represent the imaging conditions of the TEAM 1.0 microscope using bright field BF (18 - 36 mrad), and HAADF (60 - 98 mrad) detectors at a 300keV acceleration voltage and probe semi-angle of 30 mrad.

Atomap, a Python library created for the analysis of atomic resolution STEM images [51], was used for 2-D Gaussian fitting of atomic columns of average experimental STEM HAADF images and the simulated micrographs. It was also used to aid in identifying symmetry axes.

### 4.3. Results and discussion

A drift-corrected BF and HAADF STEM image pair in Figure 16 show Pt NPs embedded within  $\gamma$ -alumina. Imaging down the  $[110]$  zone axis of  $\gamma$ -alumina and Pt show the NPs have the orientation relationship of  $(111)_{\text{Pt}} \parallel (111)_{\gamma}$ ;  $[1\bar{1}0]_{\text{Pt}} \parallel [1\bar{1}0]_{\gamma}$  with the  $\gamma$ -alumina are mainly bound by  $\{111\}$  facets with an interfacial orientation relationship of  $(111)_{\text{Pt}} \parallel (111)_{\gamma}$ , as reported in. The small NPs are tetrahedral and larger ones are cubo-octahedral and, as described previously [35]. The  $(111)_{\text{Pt}}$  facets viewed edge on in the HAADF image (Figure 16a) have the brightest atomic columns, since the intensity in the HAADF increases with increasing thickness and atomic

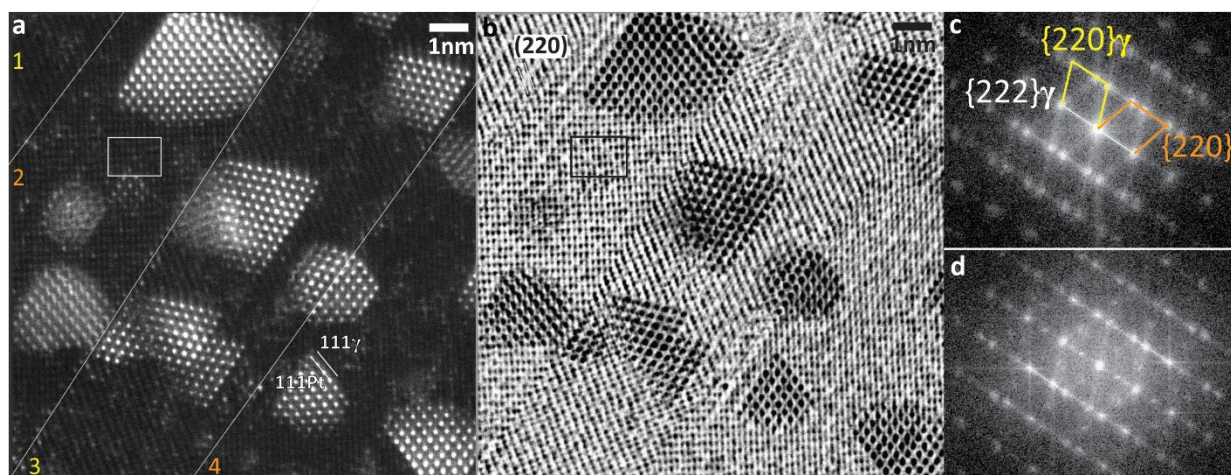


Figure 16 HRSTEM HAADF and BF image of  $\gamma$ - $\text{Al}_2\text{O}_3$

*STEM (a) HAADF and (b) BF image pair show Pt NPs embedded in  $\gamma$ -alumina down the  $[110]$  zone-axis. Twins in the alumina are marked in the HAADF image by white lines and the orientation of the  $(220)$  plane is marked in the BF image. Details of a unit cell of alumina marked by boxes are shown in Figure 17. The FFTs of the HAADF (c) and BF (d) show the twin orientations (labeled in c). The increased contrast in the alumina matrix results in additional intensities in (d) not seen in (c)*

number. The tetrahedral particles taper off in thickness in the [220] direction which causes decreasing brightness in the Pt columns of the HAADF image. The appearance of the faceted Pt/alumina interfaces in this image are typical of Pt NPs observed. It is useful to have the image pair, as the BF STEM image (Figure 16(b)) shows greater contrast in the alumina matrix than the HAADF, which is reflected in the additional intensities that are present in the fast Fourier transforms (FFTs, Figure 16(c-d)). The alumina is multiply twinned and the twin boundaries are marked in Figure 16(a) by white lines and identified in the HAADF FFT. The twins are labeled 1-4; 2 and 4 have the same orientation such that  $(220)_\gamma$  planes are horizontal in the figure. Twin 2 is most precisely oriented on [110] zone axis and thus the atomic columns in the  $\gamma$ -alumina are especially clear.

#### 4.3.1. Comparison of $\gamma$ -alumina to Smrčok and Zhou models

A detail of a unit cell of alumina identified by the boxes in Figure 16(a) and (b) is shown in 17(a) and 17(b), respectively. The structure of the  $\gamma$ -alumina is compared to the Zhou and Smrčok models and image simulations in Figure 17(c-d). The two models have an O sublattice in common, as well as  $Al_o$  in the 16d position though they differ in occupancy of this position. Both models have spinel  $Al_t$ , though they too differ in simulated intensity due to differences in occupation. The presence of quasi-octahedral Al in the Zhou model give rise to a smeared out, elliptical appearance of some atomic columns which are not observed in the experimental images. The Smrčok model does not have elliptical features and shows clear intensity at  $Al_t$  and non-spinel  $Al_o$  sites between (220) planes between the atomic columns associated with O sublattice.

The simulated STEM images show a convenient (visual) structural unit of O- $Al_o$ -O that appears as a horizontal row of three spots. These groups of three atomic columns are marked by

boxes on the simulated images and corresponding models. These units are separated by an apparent gap in intensity where there is a (111) layer of Al occupying a mix of  $Al_t$ ,  $Al_o$ , and, in the Zhou model, quasi-tetrahedral positions. Of the two models, the Al occupancy in the Smrčok model results in a more uniform intensity of all columns in the diagonal band of O- $Al_o$ -O layers, which better matches the banding seen in the experimental image.

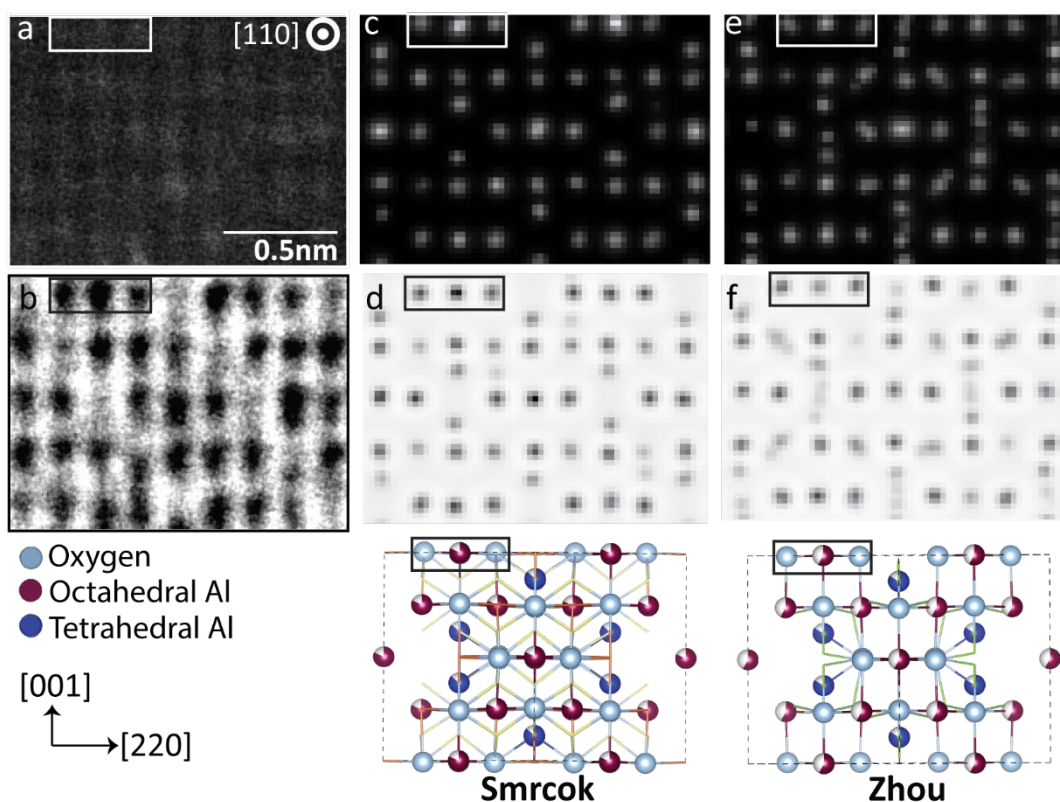


Figure 17 A HAADF and BF image pair of a unit cell of alumina from Figure 16 with  $\gamma$ -alumina simulations.

(a) HAADF and (b) BF image pair of a unit cell of alumina from Figure 16(a) and (b). Structural units made up of O- $Al_o$ -O are marked by boxes in the Smrčok and Zhou models of  $\gamma$ -alumina viewed along [110] with BF and HAADF image simulations. Units made up of O- $Al_o$ -O are marked in the Smrčok and Zhou models and image simulations of  $\gamma$ -alumina. The Smrčok model results in more uniform intensity in the entire band of O- $Al_o$ -O units and lower intensity positions mainly occupied by  $Al_t$  resulting in a better match to the experimental images.

Although there is variability in the intensities in  $\gamma$ -alumina in the experimental images, the key features of the dense plane of units of three atomic columns that runs diagonally with  $\{111\}$  planes separated by less densely occupied (111) planes, allow us through comparison with the models to differentiate the O layers from the different Al layers.

Figure 18 shows a drift-corrected BF/HAADF STEM image pair of a thin area of  $\gamma$ -alumina with small Pt NPs viewed down a  $[211]$  zone axis. There appear to be two structural variants in the alumina. An area that contains both of these variants is marked by blue boxes in Figure 18(a, b) and are compared to the Zhou and Smrčok models and image simulations in Figure 19. Figure 19 shows both variants as well as an intermediate area between the variants. Using image simulations of bulk alumina (Figure 17(c) and (d)), both the Smrčok and Zhou models predict a

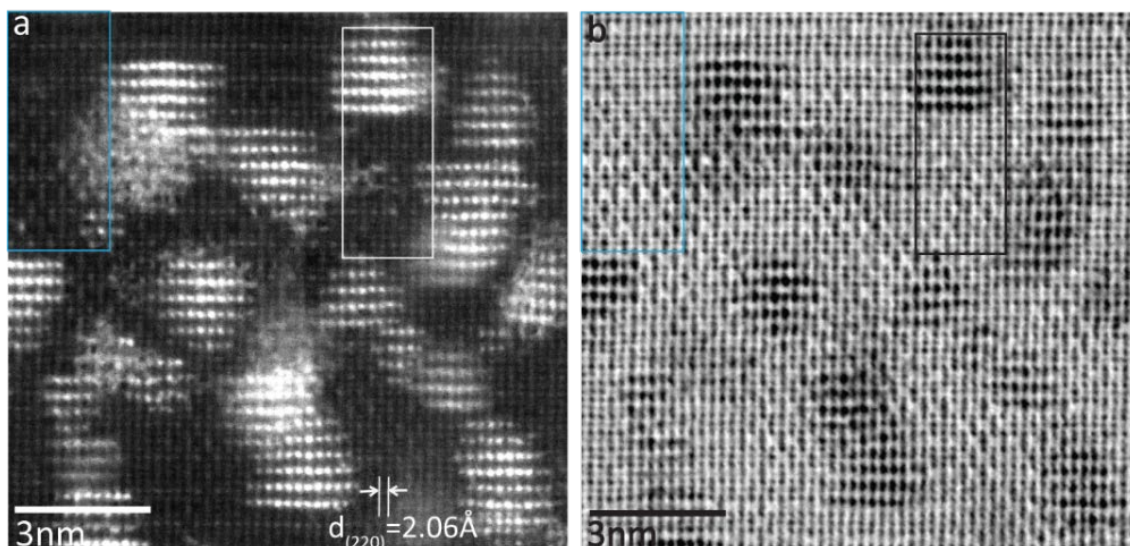


Figure 18 Drift-corrected (a) BF and (b) HAADF pair of Pt NPs in  $\gamma$ -alumina viewed on a  $[211]$  zone axis.

*The  $\{111\}$  planes run horizontally in this image. Only one horizontal (111) Pt facet in each NP is viewed edge. Two variants of alumina ordering are highlighted in the box in the upper left, shown in detail in Figure 19. The mottled appearance in areas of (a) is due to the accumulation of material on the surface during imaging as a consequence of beam damage.*

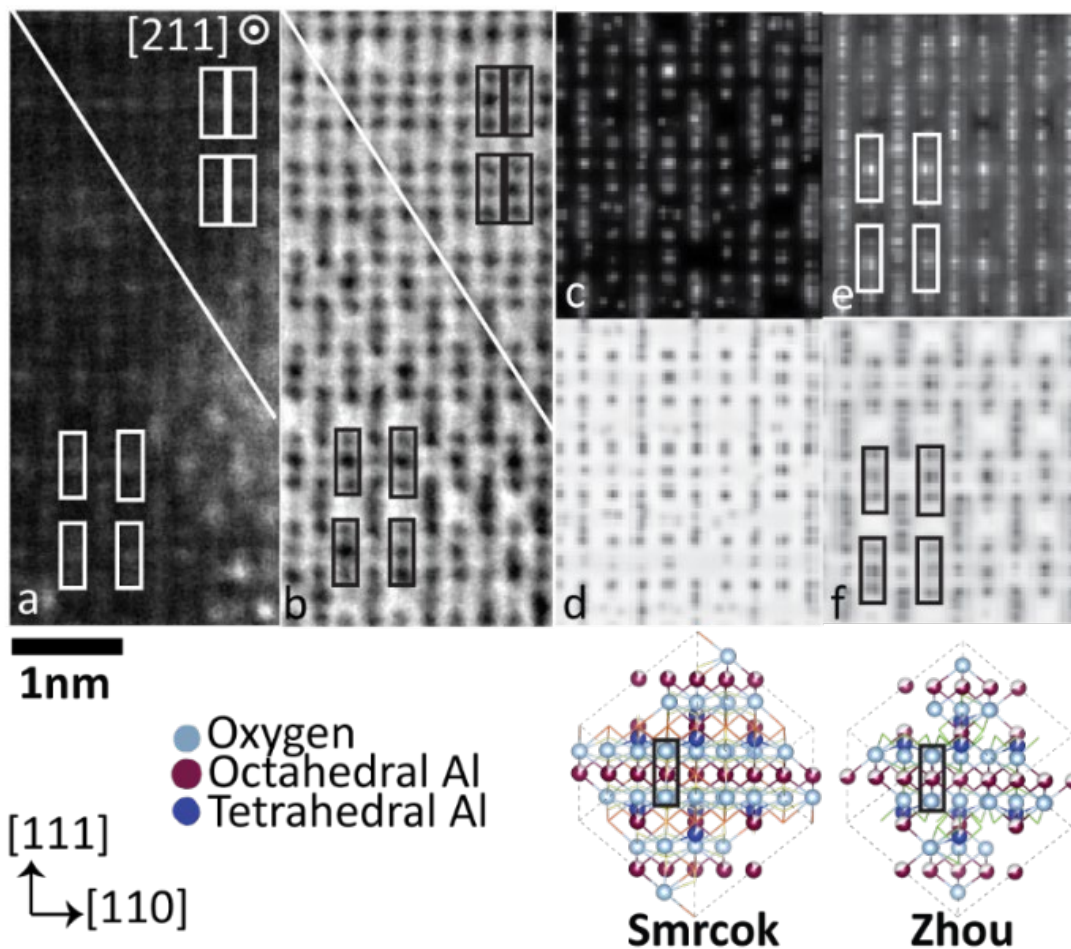


Figure 19 Detail from Figure 18 with DFT models and simulations

shows both alumina variants in (a) BF and (b) HAADF. A white line indicates the approximate boundary between the variants. BF and HAADF Prismatic simulations of the Smrčok unit cell and the Zhou unit cell viewed down the  $[211]$  zone axis are shown in (c-d) and (e-f), respectively. Boxes mark O-Al<sub>6</sub>-O units in the simulated images which match the boxed features in the experimental images. All images and simulations are shown to the same scale.

brick-like arrangement of O-Al<sub>o</sub>-O units, which is seen on the lower left side of the experimental images. The second variant on the upper right side of 16(a-b) and appears to have O-Al<sub>o</sub>-O units aligned in linear rows and there is also an apparent increase in occupancy between the O-Al<sub>o</sub>-O units. Local changes in the stacking order of these O-Al<sub>o</sub>-O units are seen in the [211] zone axis of the  $\gamma$ -Al<sub>2</sub>O<sub>3</sub> but were not readily apparent in the [110] zone axis images. From the models, in this orientation the Al<sub>t</sub> positions can be identified in rows of alumina that appear smeared out along vertical <220> direction. The linearly stacked variant has a greater amount of Al<sub>t</sub> than the brick-like stacking with respect to the bulk  $\gamma$ -alumina simulations.

The expected lattice misfit between Pt and  $\gamma$  alumina is small (1.11% and 1.46% for the Smrčok and Zhou structures respectively). The experimentally determined lattice parameter for the Pt and  $\gamma$ -alumina in this study are shown in Table 3 Pt and  $\gamma$ -Al<sub>2</sub>O<sub>3</sub> lattice parameters. The  $\gamma$ -alumina is slightly larger than both parameters reported in the bulk structures simulated in this study. The Smrčok structure is a better fit than the Zhou model to experimental data in terms of the distribution of Al and in the measured experimental d-spacing.

Table 3 *Pt and  $\gamma$ -Al<sub>2</sub>O<sub>3</sub> lattice parameters*

<b>Measured Pt and Al<sub>2</sub>O<sub>3</sub></b>	<b>Lattice parameter (nm)</b>
Pt [52]	0.3912
Pt experiment	0.4163 ± 0.001
Zhou $\gamma$ -alumina	0.7911
Smrčok $\gamma$ -alumina	0.793820
$\gamma$ -alumina experiment	0.822 ± 0.016

### 4.3.2. The structure of the (111) Pt/ $\gamma$ -alumina interface

Figure 20(a-b) shows a drift-corrected HAADF and BF image pair of a cubo-octahedral NP bound by four edge-on  $\{111\}$  facets viewed along a  $[110]$  zone axis. The differences in the alumina appearance in 6(b) can be attributed to twinning around the NP and to very slight changes in grain orientation relative to the  $[110]$  direction. The FFT (inset) shows a pattern consistent with Pt and twinned  $\gamma$ -alumina grains. Although the contrast varies somewhat, the  $\{111\}$  Pt/ $\gamma$  facets have a similar structure close to their interfaces. The boxed areas in 17(a-b) are reproduced in 17(c-d), respectively, as the  $\gamma$ -alumina is exactly on zone axis in this region and shows clarity of atomic columns at the interface. The  $\gamma$ -alumina at the interfaces with Pt in the BF image 17(d) very consistently show a row of three dark columns (marked with a box), which match the O-Al<sub>o</sub>-O units in model and image simulations of the Oware-Sarfo DFT oxygen-terminated  $(111)_{\text{Pt}}|| (111)_{\gamma}$  interface. The Pt-O distance of the O-terminated oxygen interfacial model is the 0.2035 nm, the Al<sub>1</sub> Pt-O distance is 0.1948 nm and the Al<sub>2</sub> Pt-O distance is 0.3284 nm. The measured average interfacial distance on a single NP was calculated using ten different measurements of experimental images is 0.2096 with a standard deviation of 0.084. The O-Al<sub>o</sub>-O structural unit is marked by small boxes in 17(e-f). In both the model and experiment the Pt appears to sit directly on top of what appears to be the terminating layer of atoms in the  $\gamma$ -alumina. (The Al<sub>1</sub>- and Al<sub>2</sub>-terminated interfaces and image simulations are available in the Supplemental materials for comparison, but they both provide a much poorer match to the experimentally observed interface structure.)

Comparison of the simulated and experimental images shows a good match at the interface to four layers of atoms into the alumina. The chemical termination of this model consists of a Pt-O-Al<sub>o</sub>-O-Al<sub>t</sub>. The Oware-Sarfo interface model provides less of match further into the bulk of the  $\gamma$ -

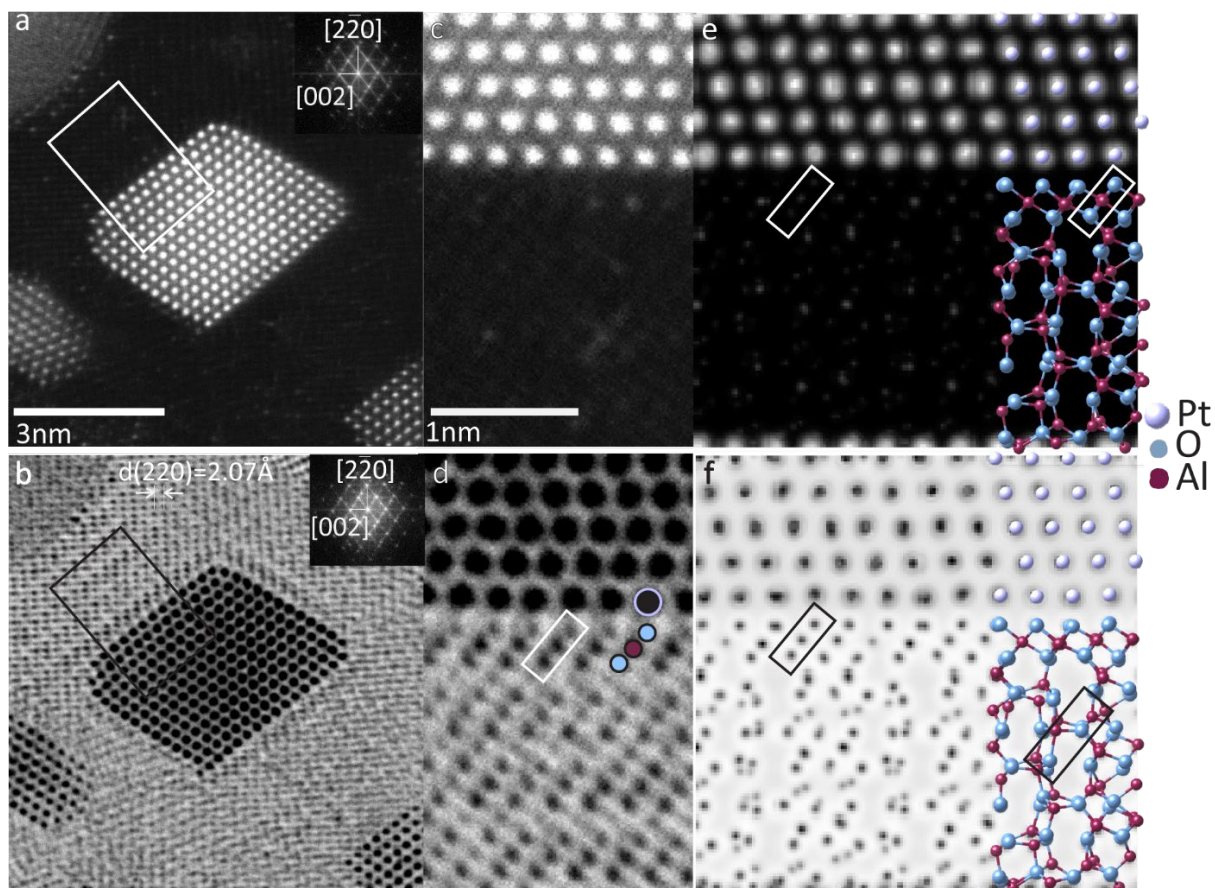


Figure 20 Drift-corrected HAADF and BF STEM image pair of a Pt NP in  $\gamma$ -alumina with DFT model and simulated interface imaged along the  $[110]_{\text{Pt}}$  zone-axis

*Drift-corrected (a) HAADF and (b) BF STEM image pair of a Pt NP in  $\gamma$ -alumina interface imaged along the  $[110]_{\text{Pt}}$  zone-axis. The Pt NP is bound by with  $(111)_{\text{Pt}}/\gamma$ -alumina interfaces. Details of the boxed region are shown in (c-d). Prismatic STEM (e) HAADF and (f) BF simulated images of the O-terminated interface with the model overlaid on the right, where white balls = Pt, small purple balls = Al and light blue balls = O. There is an excellent match between the experimental images and the simulated images of the O-terminated Oware Sarfo model interface up to the first four layers of the alumina ( $\text{O-Al}_6\text{-O-Al}_6$ ), but the match is poorer further into the bulk  $\text{Al}_2\text{O}_3$ .*

alumina. The DFT model structure in Figure 20(e-f) does not maintain the high alignment of the O-Al<sub>o</sub>-O units into the bulk, although they are clearly observed experimentally in Figure 20(d).

Figure 21(a-b) show the (111)Pt/ $\gamma$ -alumina interface from the boxed area in Figure 18(a-b) viewed on a  $[211]_{\text{Pt}}$  zone-axis. This NPs is small and tetrahedral. In this orientation only one interface of Pt tetrahedra is parallel to the electron beam. From Figure 19 it appears that O-Al<sub>o</sub>-O stacking may be brick-like or linear at the vicinity of the interface. In the  $[211]$  zone axis the O and octahedral and tetrahedral Al are stacked in (vertical) (220) planes perpendicular to (111) planes (which are horizontal in Figure 18 and Figure 21). This means that (220) plane with high and low occupancy of Al<sub>t</sub> positions can be differentiated more easily than down the  $[110]$  zone axis, because imaging down this axis shows (220) planes with Al<sub>t</sub> and Al<sub>o</sub> occupancy that are separated and not overlapping (unlike the  $[110]$  direction where non-spinel octahedral Al overlay Al<sub>t</sub> positions).

The  $[211]$  zone axis shows an interfacial termination consistent with O-Al<sub>o</sub>-O ordering of atoms viewed in the  $[110]$  images. This structural unit is marked by boxes in each part of Figure 21. The vertical planes of (220)  $\gamma$ -alumina with more tetrahedral Al than octahedral Al appear

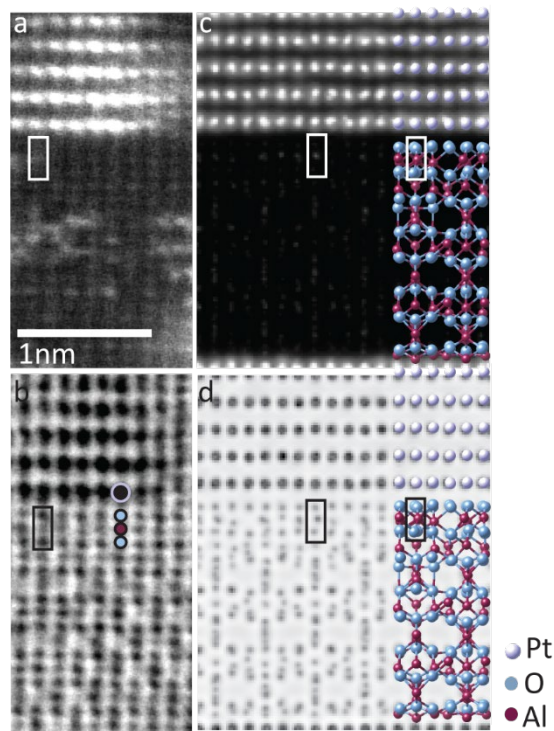


Figure 21 Detail of a (111)Pt/ $\gamma$ -alumina interface boxed in Figure 18.

*HAADF and BF images(a-b) viewed on a  $[211]_{\text{Pt}}$  zone-axis. Prismatic simulated STEM (c) HAADF and (d) BF micrographs with the Oware-Sarfo O-terminated interface model overlaid on the right side. All parts are to the same scale as in (a).*

smear out compared to planes where octahedral Al predominate. Vacant rows of O interstitial sites,  $\square_i$ , appear in the simulated images as gaps between O-Al<sub>o</sub>-O units.

The [211] simulated images of the Oware Sarfo O-terminated interface in 18(c, d) show rows with  $\square_i$  sites adjacent. In the adjacent  $\square_i$  positions, one row is comprised of O-Al<sub>t</sub>-Al<sub>t</sub>-O- $\square_i$  units and the other of O-Al<sub>o</sub>-O- $\square_i$  units. The (220) planes with no  $\square_i$  border the two  $\square_i$  alumina rows and appear line like due to a mixture of both Al<sub>t</sub> and Al<sub>o</sub> sites; the box in 18(c-d) are centered on an O-Al<sub>o</sub>-O unit in a row of (220) alumina that is free of  $\square_i$ . In the O-terminated image simulations the first row of Al<sub>o</sub> adjacent to the Pt interface shows a mostly octahedral Al occupancy with a single  $\square_i$ . Experimental interfaces viewed from the [211] zone-axis do not have a low contrast area associated with  $\square_i$  in the first layer of Al the interface as in the model.

The best fitting Oware-Sarfo interfacial model to all the particles with (111)<sub>Pt</sub>|| (111)<sub>γ</sub> interfaces is the O-terminated model, which has many of the same features as the experimental images including the Pt positioned on top of the terminating O as viewed from both the [110] and [211] zone axes. The (111) facets of Pt particles imaged in this study were bound by rows of O-Al<sub>o</sub>-O planes as seen in Figure 20 and Figure 21.

The likelihood of Pt bonding to oxygen on  $\gamma$ -alumina has been proposed in other studies. The O-terminated Oware Sarfo image simulation of embedded Pt ions confirms this relationship. Ayoola et al.[43] proposed a DFT-based interfacial structure made up of tetrahedrally coordinated Al at the surface of a  $\gamma$ -alumina supporting a single Pt atom, however they proposed the existence of an O adatom bridge, which was necessary to make their experimental EELS spectrum consistent with their simulated spectra. Pt has also been found to bond to O on interface with other phases of alumina. A study comparing DFT-based calculated structures of (111)Pt/(0001) $\alpha$ -alumina interfaces with O-, Al-, and Al<sub>2</sub>-terminations of the  $\alpha$ -alumina to high-resolution TEM (HRTEM)

data [53] found the O-termination to be best structural match to Pt/ $\alpha$ -alumina interfaces of embedded Pt particles processed at 1973 K in air, although the transition between the Al- and the O-termination was calculated to occur at 1600 K at  $(pO_2) = 0.2$  over a large range of temperatures.

#### 4.4. Conclusions

A combination of experimental atomic-resolution microscopy with image simulation of the Zhou and Smrčok  $\gamma$ -alumina models and recently developed Pt/ $\gamma$ -alumina interfacial models were used to develop an understanding of the atomic structure of the interfaces of Pt NPs in  $\gamma$ -alumina. Prismatic STEM simulations of the Oware-Sarfo interfaces (O, Al<sub>1</sub>, Al<sub>2</sub>) show that of the three different chemical terminations of (111) interfaces show the best fitting structure is O-terminated. The simulated O-terminated structure has Pt located directly on top of the terminating O position. The next layer of atoms from the surface are Al<sub>o</sub> followed by another row of O atoms. Beyond these first three layers the ordering of the Al in the bulk  $\gamma$ -alumina remains well-ordered in the experimental image, but not in the DFT model.

The Smrčok model was a better fit to the experimentally observed  $\gamma$ -alumina in the bulk and these experiments support the view that Al can occupy non-spinel tetrahedral and octahedral sites. This was clearly visible in the form vacant sites and twins that occur frequently in the experimental alumina especially along alumina grains. The Zhou model overestimates the amount of Al<sub>t</sub> atoms present which is consistent with boehmite-derived  $\gamma$ -alumina. It was also found that defected cubic spinel models for bulk  $\gamma$ -alumina that allowed for the occupancy of non-spinel positions are appropriate for bulk  $\gamma$ -alumina.

## Chapter 4 References

- [1] C. R. Henry, "Surface studies of supported model catalysts," *Surface Science Reports*, vol. 31, no. 7-8, pp. 231-325, 1998, doi: 10.1016/s0167-5729(98)00002-8.
- [2] P. Raybaud, C. Chizallet, C. Mager-Maury, M. Digne, H. Toulhoat, and P. Sautet, "From  $\gamma$ -alumina to supported platinum nanoclusters in reforming conditions: 10 years of DFT modeling and beyond," *Journal of Catalysis*, vol. 308, pp. 328-340, 2013, doi: 10.1016/j.jcat.2013.08.015.
- [3] V. P. Pakharukova, I. Y. Pakharukov, V. I. Bukhtiyarov, and V. N. Parmon, "Alumina-supported platinum catalysts: Local atomic structure and catalytic activity for complete methane oxidation," *Applied Catalysis A: General*, vol. 486, pp. 12-18, 2014, doi: 10.1016/j.apcata.2014.08.014.
- [4] L. He, Y. Fan, L. Luo, J. Bellettre, and J. Yue, "Preparation of Pt/ $\gamma$ -Al<sub>2</sub>O<sub>3</sub> catalyst coating in microreactors for catalytic methane combustion," *Chemical Engineering Journal*, vol. 380, p. 122424, 2020, doi: 10.1016/j.cej.2019.122424.
- [5] M. Arenz *et al.*, "The Effect of the Particle Size on the Kinetics of CO Electrooxidation on High Surface Area Pt Catalysts," *Journal of the American Chemical Society*, vol. 127, no. 18, pp. 6819-6829, 2005, doi: 10.1021/ja043602h.
- [6] J. H. Kwak *et al.*, "Coordinatively Unsaturated Al<sup>3+</sup> Centers as Binding Sites for Active Catalyst Phases of Platinum on  $\gamma$ -Al<sub>2</sub>O<sub>3</sub>," *Science*, vol. 325, pp. 1670-1673, 2009.
- [7] W. G. Rothschild, H. C. Yao, and H. K. Plummer, "Surface interaction in the platinum- $\gamma$ -alumina system. V. Effects of atmosphere and fractal topology on the sintering of platinum," *Langmuir*, vol. 2, no. 5, pp. 588-593, 1986, doi: 10.1021/la00071a010.
- [8] S. M. Augustine and W. M. H. Sachtler, "Variation of catalytic activity over platinum-rhenium/ $\gamma$ -alumina," *Journal of Physical Chemistry*, vol. 91, no. 23, pp. 5953-5956, 1987, doi: 10.1021/j100307a028.
- [9] A. Dandapat, D. Jana, and G. De, "Synthesis of Thick Mesoporous  $\gamma$ -Alumina Films, Loading of Pt Nanoparticles, and Use of the Composite Film as a Reusable Catalyst," *ACS Applied Materials & Interfaces*, vol. 1, no. 4, pp. 833-840, 2009, doi: 10.1021/am800241x.
- [10] C. Mager-Maury, C. Chizallet, P. Sautet, and P. Raybaud, "Platinum Nanoclusters Stabilized on  $\gamma$ -Alumina by Chlorine Used As a Capping Surface Ligand: A Density Functional Theory Study," *ACS Catalysis*, vol. 2, no. 7, pp. 1346-1357, 2012, doi: 10.1021/cs300178y.
- [11] P. Raybaud, C. Chizallet, C. Mager-Maury, M. Digne, H. Toulhoat, and P. Sautet, "From  $\gamma$ -alumina to supported platinum nanoclusters in reforming conditions: 10 years of DFT modeling and beyond," *Journal of Catalysis*, vol. 308, pp. 328-340, Dec 2013, doi: 10.1016/j.jcat.2013.08.015.
- [12] M. W. Small, S. I. Sanchez, L. D. Menard, J. H. Kang, A. I. Frenkel, and R. G. Nuzzo, "The atomic structural dynamics of  $\gamma$ -Al<sub>2</sub>O<sub>3</sub> supported Ir-Pt nanocluster catalysts prepared from a bimetallic molecular precursor: a study using aberration-corrected electron microscopy and X-ray absorption spectroscopy," *J Am Chem Soc*, vol. 133, no. 10, pp. 3582-91, Mar 16 2011, doi: 10.1021/ja110033g.
- [13] Z. Zhang, L. Li, and J. C. Yang, "Adhesion of Pt Nanoparticles Supported on  $\gamma$ -Al<sub>2</sub>O<sub>3</sub> Single Crystal," vol. 117, no. 41, pp. 21407-21412, 2013, doi: 10.1021/jp407798b.

- [14] H. O. Ayoola *et al.*, "Probing the Local Bonding at the Pt/ $\gamma$ -Al<sub>2</sub>O<sub>3</sub> Interface," *The Journal of Physical Chemistry C*, vol. 124, no. 18, pp. 9876-9885, 2020, doi: 10.1021/acs.jpcc.9b12029.
- [15] C. Dessal *et al.*, "Atmosphere-dependent stability and mobility of catalytic Pt single atoms and clusters on  $\gamma$ -Al<sub>2</sub>O<sub>3</sub>," *Nanoscale*, vol. 11, no. 14, pp. 6897-6904, 2019, doi: 10.1039/c9nr01641d.
- [16] C. W. White *et al.*, "Ion Implantation and Annealing of Oxides," *Nuclear Instruments and Methods in Physics Research*, no. B32, pp. 11-22, 1987.
- [17] E. Alves, R. C. Da Silva, O. Conde, M. F. Da Silva, and J. C. Soares, "Formation of coherent precipitates of platinum in sapphire," *Nuclear Instruments and Methods in Physics Research Section B: Beam Interactions with Materials and Atoms*, vol. 148, no. 1-4, pp. 1049-1053, 1999, doi: 10.1016/s0168-583x(98)00706-x.
- [18] M. K. Santala, V. Radmilovic, R. Giulian, M. C. Ridgway, A. M. Glaeser, and R. Gronsky, "Precipitate orientation relationships in Pt-implanted sapphire," *Scripta Materialia*, vol. 62, no. 4, pp. 187-190, 2010, doi: 10.1016/j.scriptamat.2009.10.023.
- [19] M. K. Santala, V. Radmilovic, R. Giulian, M. C. Ridgway, R. Gronsky, and A. M. Glaeser, "The orientation and morphology of platinum precipitates in sapphire," *Acta Materialia*, vol. 59, no. 12, pp. 4761-4774, 2011, doi: 10.1016/j.actamat.2011.04.012.
- [20] M. Gandman, M. Ridgway, R. Gronsky, and A. M. Glaeser, "Microstructural evolution in Pt-implanted polycrystalline Al<sub>2</sub>O<sub>3</sub>," *Acta Materialia*, vol. 83, pp. 169-179, 2015, doi: 10.1016/j.actamat.2014.09.045.
- [21] S. J. Wilson, "Dehydration Of Boehmite, Gamma-AlOOH, To Gamma-Al<sub>2</sub>O<sub>3</sub>," (in English), *Journal of Solid State Chemistry*, Article vol. 30, no. 2, pp. 247-255, 1979, doi: 10.1016/0022-4596(79)90106-3.
- [22] K. Wefers and C. Misra, "Oxides and Hydroxides of Aluminum," *Alcoa Technical Paper*, vol. 19, 1987.
- [23] C. W. White, C. J. McHargue, P. S. Sklad, L. A. Boatner, and G. C. Farlow, "Ion implantation and annealing of crystalline oxides," *Material Science Reports*, vol. 4, no. 2-3, pp. 41-146, July 1989, doi: 10.1016/s0920-2307(89)80005-2.
- [24] J. C. Yang, E. Schumann, I. Levin, and M. Ruhle, "Transient oxidation of NiAl," *Acta Materialia*, vol. 46, no. 6, pp. 2195-2201, Mar 23 1998, doi: 10.1016/s1359-6454(97)00378-9.
- [25] Y. Liu *et al.*, "Hydrothermal synthesis of microscale boehmite and gamma nanoleaves alumina," *Materials Letters*, vol. 62, no. 8-9, pp. 1297-1301, 2008, doi: 10.1016/j.matlet.2007.08.067.
- [26] J.-H. Yi, Y.-Y. Sun, J.-F. Gao, and C.-Y. Xu, "Synthesis of crystalline  $\gamma$ -Al<sub>2</sub>O<sub>3</sub> with high purity," *Transactions of Nonferrous Metals Society of China*, vol. 19, no. 5, pp. 1237-1242, 2009, doi: 10.1016/s1003-6326(08)60435-5.
- [27] S. Lan, N. Guo, L. Liu, X. Wu, L. Li, and S. Gan, "Facile preparation of hierarchical hollow structure gamma alumina and a study of its adsorption capacity," *Applied Surface Science*, vol. 283, pp. 1032-1040, 2013, doi: 10.1016/j.apsusc.2013.07.064.
- [28] X. Krokidis, P. Raybaud, A.-E. Gobichon, B. Rebours, P. Euzen, and H. Toulhoat, "Theoretical Study of the Dehydration Process of Boehmite to  $\gamma$ -Alumina," *The Journal of Physical Chemistry B*, vol. 105, no. 22, pp. 5121-5130, 2001, doi: 10.1021/jp0038310.
- [29] S. J. Wilson, "The Dehydration of Boehmite, g-AlOOH to g-Al<sub>2</sub>O<sub>3</sub>," *Journal of Solid State Chemistry*, vol. 30, pp. 247-255, 1979.

- [30] L. Kovarik, M. Bowden, A. Genc, J. Szanyi, C. H. F. Peden, and J. H. Kwak, "Structure of  $\delta$ -Alumina: Toward the Atomic Level Understanding of Transition Alumina Phases," *The Journal of Physical Chemistry C*, vol. 118, no. 31, pp. 18051-18058, 2014, doi: 10.1021/jp500051j.
- [31] J. D. Budai, C. W. White, S. P. Withrow, M. F. Chisholm, J. Zhu, and R. A. Zuhr, "Controlling the size, structure and orientation of semiconductor nanocrystals using metastable phase recrystallization," *Nature*, vol. 390, no. 6658, pp. 384-386, 1997, doi: 10.1038/37079.
- [32] M. Arai, "Particle size effect and structure sensitivity in catalysis by supported metal catalysts," *JOURNAL OF CHEMICAL ENGINEERING OF JAPAN*, vol. 30, no. 6, pp. 1123-1125, 1997, doi: 10.1252/jcej.30.1123.
- [33] P. Eklund, M. Sridharan, G. Singh, and J. Bøttiger, "Thermal Stability and Phase Transformations of  $\gamma$ -Amorphous- $\text{Al}_2\text{O}_3$  Thin Films," *Plasma Processes and Polymers*, vol. 6, no. S1, pp. S907-S911, 2009, doi: 10.1002/ppap.200932301.
- [34] S. Lamouri *et al.*, "Control of the  $\gamma$ -alumina to  $\alpha$ -alumina phase transformation for an optimized alumina densification," *Boletín de la Sociedad Española de Cerámica y Vidrio*, vol. 56, no. 2, pp. 47-54, 2017, doi: 10.1016/j.bsecv.2016.10.001.
- [35] A. L. Clauser *et al.*, "Orientation and morphology of Pt nanoparticles in  $\gamma$ -alumina processed via ion implantation and thermal annealing," *Scr. Mater.*, vol. 188, pp. 44-49, 2020.
- [36] R.-S. Zhou and R. L. Snyder, "Structures and transformation mechanisms of the eta, gamma, and theta transitions aluminas," *Acta Cryst.*, vol. B47, pp. 617-630, 1991.
- [37] L. Smrcok, V. Langer, and J. Krestan, "Gamma-alumina: a single-crystal X-ray diffraction study," *Acta Crystallogr C*, vol. 62, no. Pt 9, pp. i83-4, Sep 2006, doi: 10.1107/S0108270106026850.
- [38] M. Digne, P. Sautet, P. Raybaud, P. Euzen, and H. Toulhoat, "Hydroxyl Groups on  $\gamma$ -Alumina Surfaces: A DFT Study," *Journal of Catalysis*, vol. 211, no. 1, pp. 1-5, 2002, doi: 10.1006/jcat.2002.3741.
- [39] M. Digne, P. Sautet, P. Raybaud, P. Euzen, and H. Toulhoat, "Use of DFT to achieve a rational understanding of acid-basic properties of  $\gamma$ -alumina surfaces," *Journal of Catalysis*, vol. 226, no. 1, pp. 54-68, Aug 2004, doi: 10.1016/j.jcat.2004.04.020.
- [40] G. Paglia *et al.*, "Tetragonal structure model for boehmite-derived gamma-alumina," *Physical Review B*, vol. 68, no. 14, pp. 144110 (1-11), 10/27/ 2003, doi: 10.1103/PhysRevB.68.144110.
- [41] H. P. Pinto, R. M. Nieminen, and S. D. Elliott, "Ab initio study of  $\gamma$  -  $\text{Al}_2\text{O}_3$  surfaces," *Physical Review B*, vol. 70, no. 12, 2004, doi: 10.1103/physrevb.70.125402.
- [42] H. O. Ayoola, S. D. House, C. S. Bonifacio, K. Kisslinger, W. A. Saidi, and J. C. Yang, "Evaluating the accuracy of common  $\gamma$ - $\text{Al}_2\text{O}_3$  structure models by selected area electron diffraction from high-quality crystalline  $\gamma$ - $\text{Al}_2\text{O}_3$ ," *Acta Materialia*, vol. 182, pp. 257-266, 2020, doi: 10.1016/j.actamat.2019.10.027.
- [43] H. O. Ayoola *et al.*, "Probing the Local Bonding at the Pt/ $\gamma$ - $\text{Al}_2\text{O}_3$  Interface," *Journal of Physical Chemistry C*, vol. 124, no. 18, pp. 9876-9885, May 2020, doi: 10.1021/acs.jpcc.9b12029.
- [44] N. A. Deskins, D. H. Mei, and M. Dupuis, "Adsorption and diffusion of a single Pt atom on  $\gamma$ - $\text{Al}_2\text{O}_3$  surfaces," *Surface Science*, vol. 603, no. 17, pp. 2793-2807, Sep 2009, doi: 10.1016/j.susc.2009.07.021.

- [45] J. H. Kwak *et al.*, "Coordinatively unsaturated  $\text{Al}_3^+$  centers as binding sites for active catalyst phases of platinum on  $\gamma\text{-Al}_2\text{O}_3$ ," *Science*, vol. 325, no. 5948, pp. 1670-1673, Sep 25 2009, doi: 10.1126/science.1176745.
- [46] C. Mager-Maury, G. Bonnard, C. Chizallet, P. Sautet, and P. Raybaud, "H-2-Induced Reconstruction of Supported Pt Clusters: Metal-Support Interaction versus Surface Hydride," *ChemCatChem*, vol. 3, no. 1, pp. 200-207, Jan 2011, doi: 10.1002/cctc.201000324.
- [47] K. Oware Sarfo, A. L. Clauser, M. K. Santala, and L. Árnadóttir, "On the atomic structure of Pt(111)/ $\gamma\text{-Al}_2\text{O}_3$ (111) interfaces and the changes in their interfacial energy with temperature and oxygen pressure," *Appl. Surf. Sci.*, vol. 542, p. 148594, 2021/03/15/2021, doi: <https://doi.org/10.1016/j.apsusc.2020.148594>.
- [48] C. Ophus, J. Ciston, and C. T. Nelson, "Correcting nonlinear drift distortion of scanning probe and scanning transmission electron microscopies from image pairs with orthogonal scan directions," *Ultramicroscopy*, vol. 162, pp. 1-9, 2016, doi: 10.1016/j.ultramic.2015.12.002.
- [49] C. Ophus, "A fast image simulation algorithm for scanning transmission electron microscopy," *Advanced Structural and Chemical Imaging*, vol. 3, no. 1, 2017, doi: 10.1186/s40679-017-0046-1.
- [50] A. Pryor, C. Ophus, and J. Miao, "A streaming multi-GPU implementation of image simulation algorithms for scanning transmission electron microscopy," *Advanced Structural and Chemical Imaging*, vol. 3, no. 1, 2017, doi: 10.1186/s40679-017-0048-z.
- [51] M. Nord, P. E. Vullum, I. MacLaren, T. Tybell, and R. Holmestad, "Atomap: a new software tool for the automated analysis of atomic resolution images using two-dimensional Gaussian fitting," *Adv Struct Chem Imaging*, vol. 3, no. 1, p. 9, 2017, doi: 10.1186/s40679-017-0042-5.
- [52] W. P. Davey, "Precision Measurements of the Lattice Constants of Twelve Common Metals," *Physical Review*, vol. 25, no. 6, pp. 753-761, 1925, doi: 10.1103/PhysRev.25.753.
- [53] C. Ophus, M. K. Santala, M. Asta, and V. Radmilovic, "Structure and phase transitions at the interface between  $\alpha\text{-Al}_2\text{O}_3$  and Pt," *J Phys Condens Matter*, vol. 25, no. 23, p. 232202, Jun 12 2013, doi: 10.1088/0953-8984/25/23/232202.

## 5. Structure of interfaces of Pt nanoparticles in $\theta$ -alumina

(in preparation for submission to the *Journal of Physical Chemistry C*)

Arielle L. Clauser,<sup>1</sup> Kofi Oware Sarfo,<sup>2</sup> Jim Ciston,<sup>3</sup> Colin Ophus,<sup>3</sup> Raquel Giulian, Líney Árnadóttir,<sup>2</sup> and Melissa K. Santala<sup>1</sup>

<sup>1</sup>*School of Mechanical, Industrial, and Manufacturing Engineering, Oregon State University, Corvallis, OR, USA*

<sup>2</sup>*School of Chemical, Biological, and Environmental Engineering, Oregon State University, Corvallis, OR, USA*

<sup>3</sup>*National Center for Electron Microscopy Facility, Molecular Foundry, Lawrence Berkeley National Laboratory, Berkeley, CA, USA*

<sup>4</sup>*Institute of Physics, Federal University of Rio Grande do Sul, Porto Alegre, Brasil*

### Abstract

The interfaces between Pt and the  $\theta$ -Al<sub>2</sub>O<sub>3</sub> were studied using atomic resolution electron microscopy. A model experimental system of Pt nanoprecipitates in  $\theta$ -Al<sub>2</sub>O<sub>3</sub> were formed in sapphire substrates via high-energy ion implantation of Pt followed by thermal annealing at 1000°C in air. The precipitates took the form of faceted tetrahedra and truncated tetrahedra primarily bound by {111}<sub>Pt</sub>. The structure and chemical bonding at the Pt/ $\theta$ -alumina interfaces were evaluated by comparing aberration-corrected scanning transmission electron microscopy (STEM) images of the interfaces to image simulations of density functional theory based models of the interface with five different chemical terminations of the  $\theta$ -alumina. The O-terminated  $\theta$ -Al<sub>2</sub>O<sub>3</sub> interface that had octahedral Al adjacent provided the best match to the experimental images.

## 5.1. Introduction

Platinum nanoparticles supported on transition phases of  $\text{Al}_2\text{O}_3$  have been the subject of numerous studies [1-6] because of their extensive use in catalysis. It has been observed that the presence of Pt in sol-gel-derived  $\text{Al}_2\text{O}_3$  films appears to stabilize transitional forms relative to films with no Pt up to  $1100^\circ\text{C}$  [1]. Although  $\alpha\text{-Al}_2\text{O}_3$  is the only thermodynamically stable form of  $\text{Al}_2\text{O}_3$  at atmospheric pressure, many metastable, transitional polymorphs of  $\text{Al}_2\text{O}_3$  exist. Transition  $\text{Al}_2\text{O}_3$  may be formed by heating hydroxides of Al [7], in the formation of thin films formed by sol-gel methods [1], and by recrystallization of sapphire substrates partially amorphized by ion implantation damage during thermal annealing [8-11]. Upon heating, a transition  $\text{Al}_2\text{O}_3$  may go through a sequence of several polymorphs before conversion to  $\alpha\text{-Al}_2\text{O}_3$ . In the transition series  $\gamma \rightarrow \delta \rightarrow \theta \rightarrow \alpha\text{-alumina}$ , the early phases begin with a face-centered (fcc) cubic O-sublattice with Al atoms being in primarily octahedral locations. As the phases evolve, more of the Al diffuse to tetrahedral sites,  $\text{Al}_t$ . The transformation to  $\theta\text{-alumina}$  has been studied and the main mechanisms of this transformation has been identified as resulting from Al migration in the sublattice to tetrahedral positions. This results in the shift of the unit cell, thus what starts as cubic  $\gamma\text{-alumina}$  with an  $Fd\bar{3}m$  crystal structure becomes distorted and evolves into monoclinic  $\theta\text{-alumina}$ , before ultimately crystallizing with a hexagonal close packed O-sublattice and all aluminum in octahedral sites,  $\text{Al}_o$ , in the  $\alpha$  phase [12]. The  $\theta\text{-Al}_2\text{O}_3$  phase, in the  $C2/m$  space group, is the terminal transition form that develops before conversion to  $\alpha\text{-Al}_2\text{O}_3$  at slightly over  $1000^\circ\text{C}$ ; as such it is sometimes called a “high-temperature” transition  $\text{Al}_2\text{O}_3$ . Although it is monoclinic, the structure of  $\theta\text{-Al}_2\text{O}_3$  can be more simply described as a distorted cubic structure, similar to the cubic polymorphs with a 50/50 distribution of Al on octahedral and tetrahedral sites [13].

Supported Pt nanoparticles are of critical importance in heterocatalyst systems and this study of a model system  $\theta$ -alumina with embedded Pt nanoparticles, yields highly detailed information on the atomic-level structure of the interfaces which is complimentary to the information derived from the study of supported metal nanoparticles. In this study, the atomic-level structure and chemistry at the interfaces of Pt/ $\theta$ -Al<sub>2</sub>O<sub>3</sub> is studied experimentally using a model system of Pt nanoparticles embedded in the alumina phase. Pt precipitates were formed by ion implantation of sapphire with Pt<sup>+</sup> followed by thermal annealing. The  $\theta$ -Al<sub>2</sub>O<sub>3</sub> forms by recrystallization of the sapphire amorphized during ion implantation allowing for a detailed study of metal precipitates in this transition phase of Al<sub>2</sub>O<sub>3</sub>. Orientation relationships for Pt formed in  $\theta$ -Al<sub>2</sub>O<sub>3</sub> by precipitation after ion implantation and annealing has been reported as  $(\bar{2}01)_{\theta} \parallel (111)_{Pt}$  with  $[132]_q \parallel [1\bar{1}0]_{Pt}$  or  $[1\bar{3}2]_{\theta} \parallel [1\bar{1}0]_{Pt}$  [14]. The  $(\bar{2}01)_{\theta} \parallel (111)_{Pt}$ ;  $[132]_q \parallel [1\bar{1}0]_{Pt}$  has parallel or near parallel alignment of the  $\{111\}_{Pt}$  with the close-packed planes in the alumina; if  $\theta$ -Al<sub>2</sub>O<sub>3</sub> were considered pseudo-cubic, this would be a parallel alignment of the cubic structures.

## 5.2. Methods

### 5.2.1. Experimental methods

An optical grade (0001) sapphire (Crystal Systems, Inc. Salem, MA) was implanted with Pt at 600keV, an energy anticipated to produce a peak Pt concentration 94 nm below the surface based on SRIM/TRIM [15] simulations. The sapphire was implanted 7° from the surface normal to prevent channeling and the dose was confirmed by RBS performed on a 5mm × 5mm piece of the sapphire. From the RBS spectrum (Figure 22) the dose was calculated to be  $6.0 \times 10^{16} \text{ cm}^{-2}$  with an uncertainty of ±5%. The Pt distribution as a function of depth (inset) shows the peak concentration matches the SRIM/TRIM simulation. Thermal annealing in air was used to induce Pt precipitation and growth. Pieces of implanted sapphire, 3mm wide, were annealed for 1h and

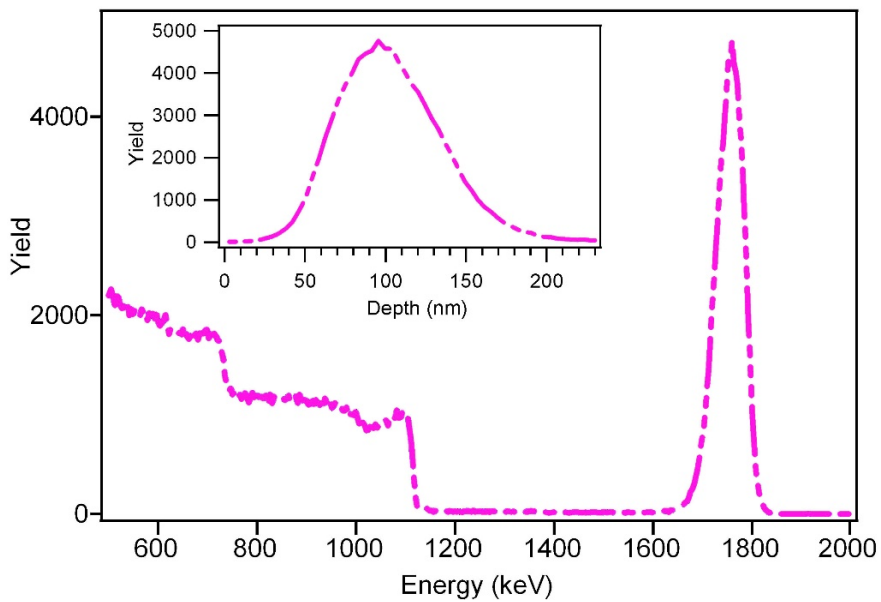


Figure 22 RBS data of implanted wafers. The inset gives the Pt distribution as a function of depth from the sapphire surface.

250 h at 1000°C. As-implanted and annealed sapphire specimens were characterized by XRD using Cu K<sub>a</sub> radiation in  $\theta$ -2 $\theta$  scans. After XRD, the specimens were prepared in cross-section electron transparent foils for transmission electron microscopy (TEM) characterization. Conventional TEM imaging and diffraction was carried out using a JEOL 200CX operated at 200 keV. High-angle annular dark-field scanning transmission electron microscopy (HAADF STEM) performed with an FEI F20 UT Tecnai microscope.

Atomic resolution scanning transmission electron microscopy was performed with the TEAM 1 double aberration corrected TEM at the National Center for Electron Microscopy at Lawrence Berkeley National Laboratory operated at 300keV. A double tilt holder was used to collect images of the implanted  $\theta$ -alumina. Orthogonal high-angle annular darkfield (HAADF) and bright field (BF) image pairs were collected and MATLAB code was used to perform non-linear drift correction [16].

Gaussian fitting to the intensity in the experimental images was performed using Atomap a Python library designed for STEM image analysis [17]. After drift correction, a set of interfaces was selected, Pt atoms in the precipitate were first identified, then the oxygen sublattice was identified. The Pt and O intensities were subtracted from the image. The remaining intensities were marked and compiled to the Al sublattice. All the identified atomic columns were then fit using 2-D Gaussian functions and had major symmetry axes identified.

### 5.2.2. Image simulation

Density function theory (DFT) based models calculated were used to simulate STEM images using Prismatic [18]. Five different chemical terminations for atomically-flat, faceted Pt/ $\theta$ -alumina interfaces with the interfacial relationship  $(\bar{2}01)_\theta \parallel (111)_{Pt}; [132]_\theta \parallel [1\bar{1}0]_{Pt}$  were calculated using DFT. Two of the interfaces were O-terminated and the other three interfaces were terminated with Al. The O-terminated interfaces have Pt-O bonds at the interface, but differ in the next layer of atoms, one having a layer of Al<sub>o</sub> adjacent (O-Al<sub>o</sub>) and the other having an Al<sub>t</sub> layer adjacent (O-Al<sub>t</sub>). The three different Al terminations are comprised of one terminated with a layer of octahedral Al (Al<sub>o</sub>), one with the full double layer of Al<sub>t</sub> (Al<sub>2t</sub>), and one with a single Al<sub>t</sub> layer (Al<sub>1t</sub>), which is half of the Al<sub>t</sub> between O layers in the bulk.

The DFT models were simulated using five different virtual imaging detector parameters to simulate a variety of imaging conditions (0 to 20 mrad to simulate BF, 18 to 36 mrad for annular BF (ABF), 30 to 80 mrad for annular DF (ADF), 60 to 98 mrad for HAADF, and 80 to 98 mrad for HAADF with no thermal diffuse scattering). The simulations were performed for 300 keV electrons and a probe semi-angle of 30 mrad. The ABF simulations showed the best contrast and are presented in the results, but not the only ones used in analysis. DFT cells were tiled using

Vesta, then rotated using exported .pdb files using Python such that the  $(\bar{2}01)_\theta \parallel (111)_{\text{Pt}}$  interfaces were perpendicular to the z-axis and four unit cells thick. The rotated files were then simulated using Prismatic.

### 5.3. Results and Discussion

Figure 23 (a) has peaks consistent with  $111_{\text{Pt}}$  and  $222_{\text{Pt}}$  and which are also consistent with several transition aluminas, such as  $\gamma$ -,  $\delta$ -, or  $\theta$ - $\text{Al}_2\text{O}_3$ . The substrate annealed at  $1000^\circ\text{C}$  Figure 23 (b), has a series of peaks from  $\theta$ - $\text{Al}_2\text{O}_3$ . The presence of the peak labeled  $\bar{6}03_\theta$  helps differentiate  $\theta$ - $\text{Al}_2\text{O}_3$  from  $\lambda$ - or  $\delta$ - $\text{Al}_2\text{O}_3$ , which have a similar structure, but which are not expected to have a peak at this location. The  $\bar{4}02_\theta$  and  $\bar{8}04_\theta$  peaks again coincide with Pt peaks. This shows a prevalent in-plane orientation between the phases of  $(0001)_a \parallel (\bar{2}01)_\theta \parallel (111)_{\text{Pt}}$ , which has been previously reported [11].

The microstructural changes that occur in the implanted sapphire during annealing at  $1000^\circ\text{C}$  are shown in TEM images of substrate cross sections (Figure 24a-c). In the as-implanted substrate (Figure 24a), an  $\sim 100\text{nm}$  layer of the matrix around the peak Pt concentration is amorphized and contains small precipitates. At this magnification, the precipitates appear as a slightly darker region near the area of expected peak Pt density. High-resolution TEM (not shown) reveals they are randomly oriented and  $\sim 2\text{ nm}$  in diameter. After 1h at  $1000^\circ\text{C}$ , the amorphized  $\text{Al}_2\text{O}_3$  has recrystallized as  $\theta$ - $\text{Al}_2\text{O}_3$  with 2 to 5 nm Pt precipitates distributed throughout the  $\theta$ - $\text{Al}_2\text{O}_3$  and with a distinct planar boundary that is decorated with larger Pt particles 20 nm above the original position of the lower amorphous-crystalline boundary. After 250h at  $1000^\circ\text{C}$ , the sapphire has not grown further into the  $\theta$ - $\text{Al}_2\text{O}_3$ . Some Pt particles at the

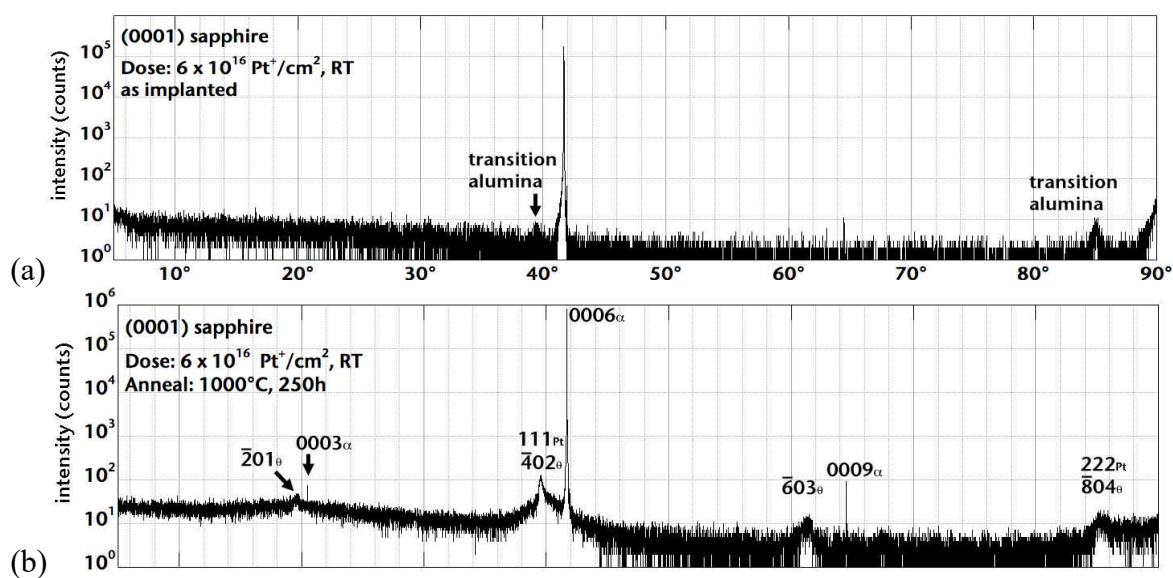


Figure 23 XRD data for (a) as-implanted sapphire and after (b) 250h at 1000°C in air. *The presence of transition  $Al_2O_3$  in different stages of processing is indicated in the XRD data.*

interface and at boundaries between columnar  $\theta$ -Al<sub>2</sub>O<sub>3</sub> grains have grown to be tens of nanometers across, but the Pt particles within the  $\theta$ -Al<sub>2</sub>O<sub>3</sub> grains have not coarsened appreciably with most remaining in the 2 to 5 nm range. The distribution of precipitates is clearer in the DF (Figure 24d) pair from the sapphire annealed for 250h at 1000°C. The dark field image shows that the precipitates have an in-plane orientation with  $(111)_{Pt} \parallel (\bar{2}01)_{\theta} \parallel (0001)_a$ .

The orientation of Pt and  $\theta$ -Al<sub>2</sub>O<sub>3</sub> within the sapphire substrate is  $(0001)_{\alpha} \parallel (\bar{2}01)_{\theta} \parallel (111)_{Pt}$  with  $[10\bar{1}0]_{\alpha} \parallel [132]_{\theta} \parallel [1\bar{1}0]_{Pt}$ , as determined by zone axis diffraction patterns. This is the same orientation as found for sapphire implanted with a lower dose ( $1 \times 10^{16} \text{ cm}^{-2}$ ) with liquid nitrogen cooling also causing amorphization of the alumina during implantation [11]. In that study, which only used indexing the conventional zone-axis diffraction patterns to determine the orientation relationship between the Pt and  $\theta$ -alumina, reported that Pt nanoparticles with  $(\bar{2}01)_{\theta} \parallel (111)_{Pt}$  and  $[1\bar{3}2]_{\theta} \parallel [1\bar{1}0]_{Pt}$  or  $[132]_{\theta} \parallel [1\bar{1}0]_{Pt}$  could both be present; however analysis of the high resolution STEM images (Figure 25), shows there to be just one orientation:  $(\bar{2}01)_{\theta} \parallel (111)_{Pt}$ ;  $[132]_{\theta} \parallel [1\bar{1}0]_{Pt}$ .

The HAADF STEM in Figure 24 shows an overview of the whole  $\theta$ -Al<sub>2</sub>O<sub>3</sub> layer therefore demonstrating the distribution of the Pt more clearly than the TEM images. The Pt precipitates stand out against the nearly black Al<sub>2</sub>O<sub>3</sub> matrix, because of the large difference in the atomic number between Pt and Al and O. The three-dimension precipitate morphology may be inferred from the HAADF images Figure 24 and Figure 25 because the Pt contributes most significantly to the intensity than the alumina matrix and within the Pt nanoparticles the intensity of each atomic column increases with the number of the Pt atoms in each column. High intensity in one corner of the triangular cross section tapering off

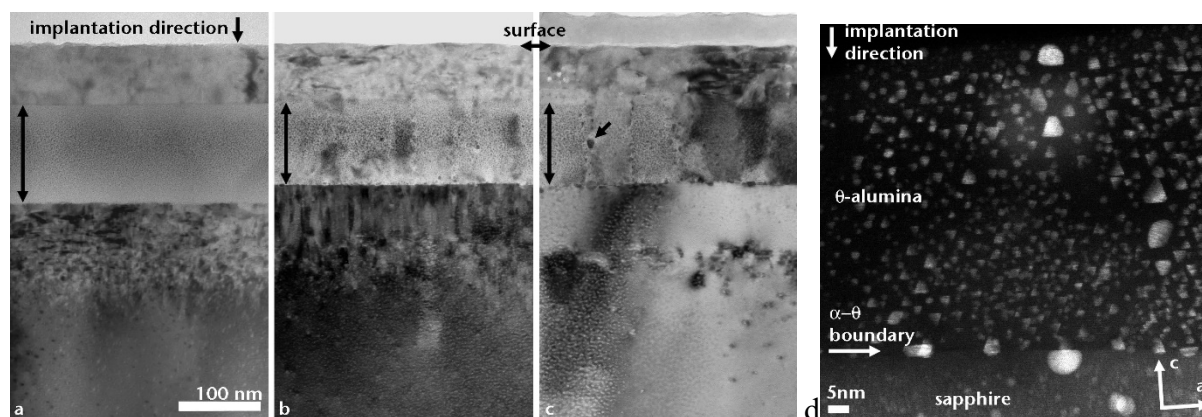


Figure 24 Bright field TEM images of the sapphire in cross-section

(a) as-implanted, (b) after 1h at 1000°C, and (c) after 250h at 1000°C in air. HAADF STEM (b) showing tetrahedral Pt precipitates in  $q\text{-Al}_2\text{O}_3$ .

toward the opposite edge is consistent with a tetrahedron with  $\{111\}_{\text{Pt}}$  faces when viewed along the  $[1\bar{1}0]_{\text{Pt}}$  direction. Smaller ( $<5$  nm) precipitates conform more nearly to the tetrahedral morphology whereas larger precipitates are generally truncated tetrahedra often with rough corners. Figure 25 shows a drift-corrected atomic-resolution HAADF and BF STEM image pair of tetrahedral Pt nanoparticles in  $\theta$ -alumina. The nanoparticles in this image are bound by two  $(111)_{\text{Pt}}$  facets and taper off parallel to the  $(002)_{\text{Pt}}$  planes. All the particles are in a single grain of alumina and have facets that are aligned in the  $\theta$ -alumina such that the  $(111)_{\text{Pt}}$  facet is parallel to bands of  $(\bar{2}01)_{\theta}$ . The contrast at the interface of these nanoparticle in the HAADF image is composed of three bright spots followed by a dark line associated with a less occupied  $(201)_{\theta}$  plane. This structure is consistent in the BF image where sets of three of low intensity spots are present and align with the columns of Pt atoms. The sample has increased thickness on the left-hand side of the image that makes the area harder to interpret, but it appears to have the same kind of structure as the thinner center areas.

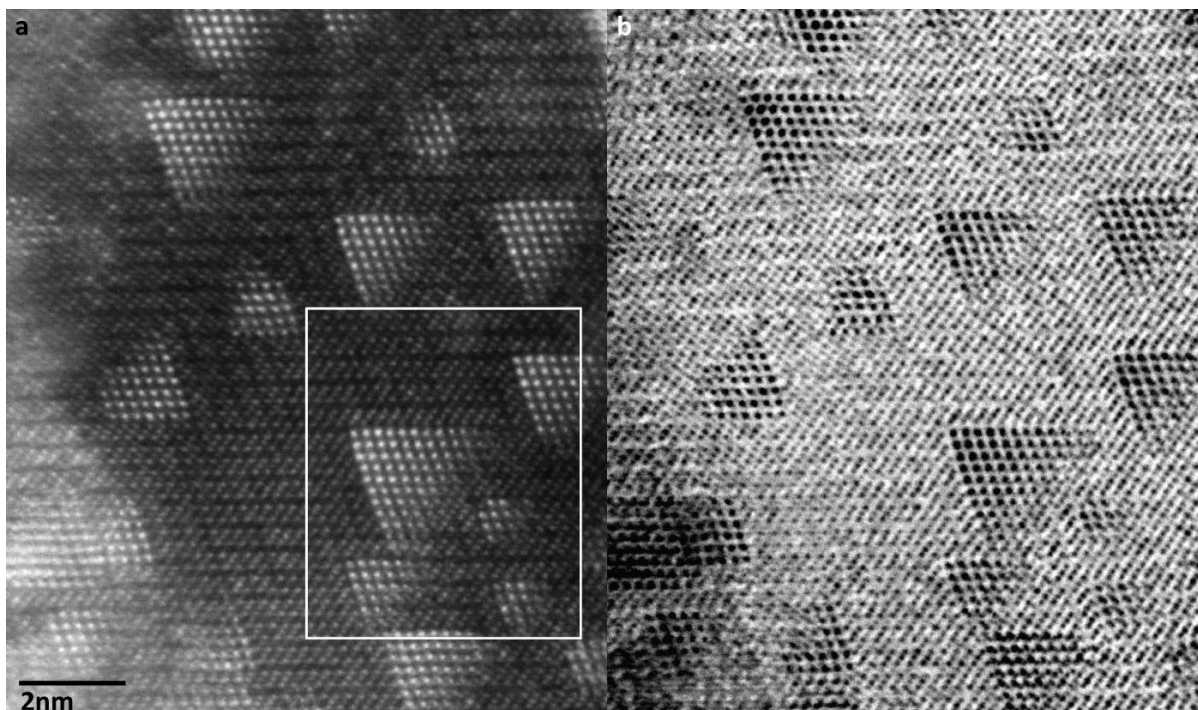


Figure 25 Drift-corrected STEM (a) HAADF and (b) BF image pair of Pt NPs in  $\theta$ -alumina show a high degree of order and uniformity in the  $\theta$ -alumina both at the interfaces and in the bulk.

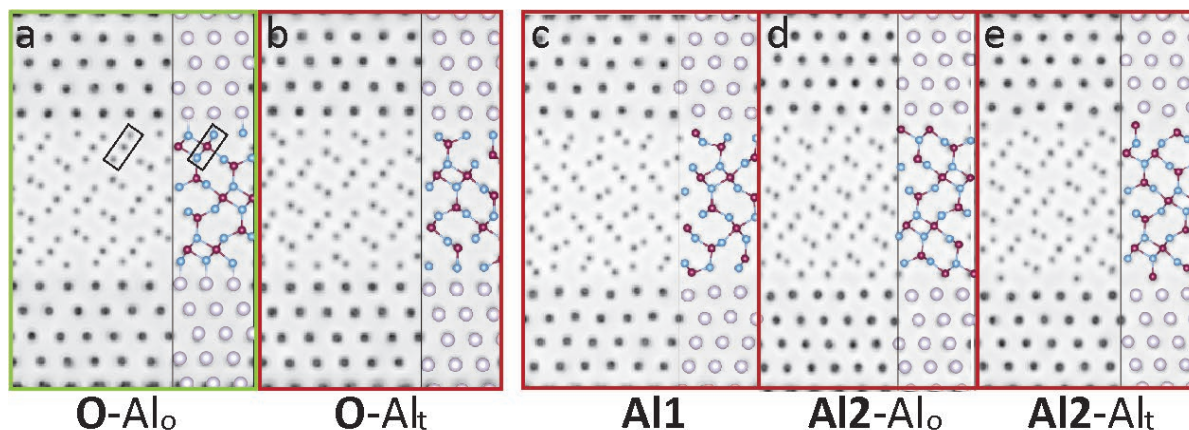


Figure 26 Simulated BF STEM images of the Pt- $\theta$  interface with overlaid DFT models the (a) O-terminated over Al<sub>o</sub> interface (b) O-terminated over Al<sub>t</sub> interface (c) Al<sub>1</sub> interface (d) Al<sub>2,o</sub> interface and (e) Al<sub>2,t</sub> interface. Platinum atoms in the model are white, Al are burgundy, and O are light blue. The box in (a) highlights a O-Al<sub>o</sub>-O structure that matches intensity variation observed at an near the Pt/ $\theta$ -alumina interfaces in the experimental images.

Figure 26 shows the DFT interfacial models and corresponding simulated BF STEM images. These simulations help in the interpretation of the contrast seen at the interfaces of the embedded nanoparticles. The Pt has far lower intensity (more prominent dark spots) in the BF image simulations than the Al or O columns. The Al and O columns have similar relative intensities in the simulations, thus their position within the alumina structure, rather than just their relative intensities are used to identify the positions of each species within the experimental image. The black box in Figure 26a identifies an O-Al<sub>o</sub>-O structural unit that has the most similar contrast to the experimental interface shown in Figure 25. A white box in Figure 25 (a) identifies the detail used for image analysis reproduced in Figure 27. In Figure 27 (a), five separate Pt nanoparticles are present and all of them have a similar contrast in the alumina at the interface. Figure 27b shows the Gaussian fit of the atomic columns identified using Atomap. In this image the red dots are Pt and the blue dots are the O sublattice in  $\theta$ -Al<sub>2</sub>O<sub>3</sub>. This inference can be confirmed by the

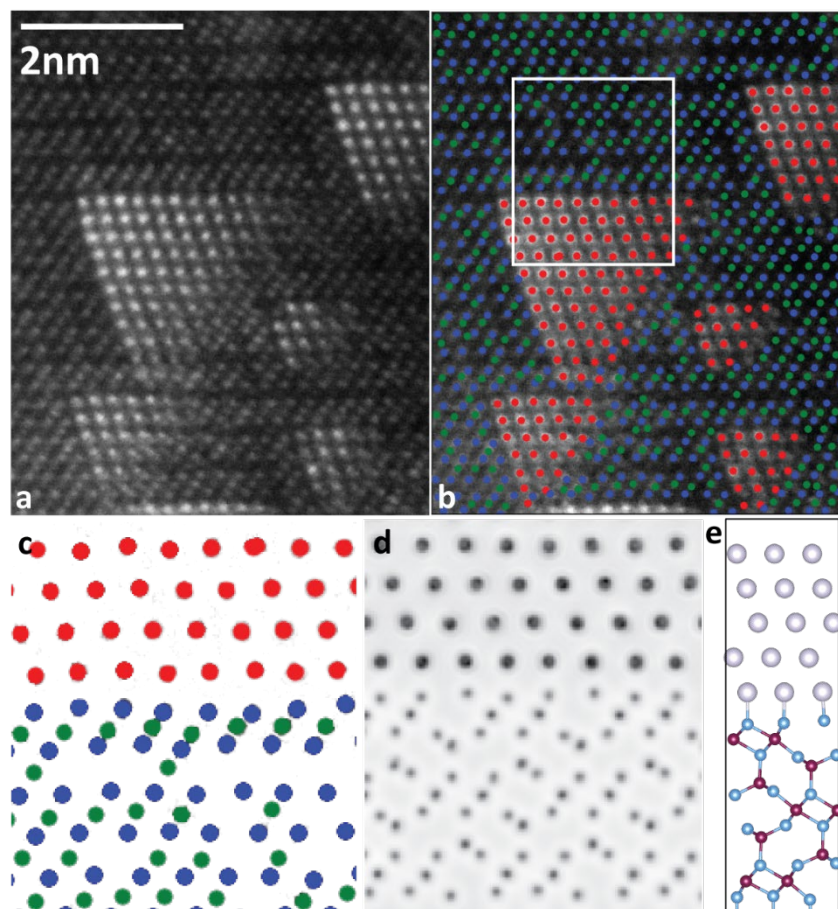


Figure 27 Detail from the Figure 25 HAADF image with analysis and DFT simulations  
 (a) Detail from the Figure 25 HAADF image, shown in (b) with Atomap fitting of the atomic position in the image, where red dots are Pt, blue dots are the O sublattice and green dots are Al atoms, (c) simulated BF STEM image of the octahedral O-terminated DFT interface, (d) atom positions of the interface in the white box of (b) to compare the detail of and fit of the interface with the (e) best fit model: O-Alo model.

complete occupation and well-ordered character of the sublattice created by the blue dots. The green dot sublattice is then identified as Al atomic columns and most likely represents contrast associated with Al<sub>o</sub>. This can be ascertained using the simulation in Figure 27d where tetrahedral columns are located perpendicularly oriented to rows of O-Al<sub>o</sub>-O. Results of the 2D Gaussian fit shown in Figure 27(d) show that the intensity between these structural units tended to be coplanar rather than perpendicular to the O-Al<sub>o</sub>-O units. Using this fitting one can see that the first three atomic layers at the interface of these atomic columns are always filled and corresponding to O-Al<sub>o</sub>-O layers. It is also important to notice the absence of atoms following these first three rows adjacent to the Pt interface. In the O-Al<sub>o</sub> interface simulation in Figure 27(c) this row of atoms is occupied by tetrahedral Al that are out of plane with the O-Al<sub>o</sub>-O structural unit, but in the experimental image there is no comparable intensity. Atomic columns associated with Al<sub>t</sub> do not have contrast that can be easily identified even using computational image analysis of the HAADF image although in the BF image some atomic columns have a slightly smeared out intensity in the bulk that could be a result of Al occupation of tetrahedral sites.

The O-terminated Al<sub>o</sub> interface in Figure 27(c) shows an Al<sub>o</sub> absence at the interface that is not present in the experimental images, although further into the bulk alumina the pattern of vacancies matches the  $\theta$ -alumina much better which suggests that the Pt nanoparticles may impart a preferred chemical interface that causes the alumina to deviate from the bulk structure near nanoparticle facets. For a quantitative comparison of the DFT models and the experimental images of the interface, the distance between the terminating layer of Pt and the layer of O closest to the interface was measured. This measure was chosen for comparison because the positions of the O atomic columns presumed O-Al<sub>o</sub>-O structural units in the experimental images

are relatively easy to identify, especially in comparison to the Al<sub>t</sub> columns. The closest Pt-O interface spacings are summarized in Table 4. The O-terminated model interfaces have a much smaller Pt-O spacing than the Al-terminated structures, as expected. The largest spacing was

Table 4 *Measured distance between the terminating layer of Pt and the layer of O closest to the interface for the five DFT models and the experimental images*

<b>Interface</b>	<b>Pt-O distance (nm)</b>
O-Al <sub>o</sub> terminated (DFT)	0.1972
O-Al <sub>t</sub> terminated (DFT)	0.1964
Al <sub>1t</sub> terminated (DFT)	0.2531
Al <sub>o</sub> terminated (DFT)	0.3473
Al <sub>2t</sub> (DFT)	0.3644
Experimental	0.189 ± 0.019

associated with Al<sub>2</sub> terminations. The experimentally measured mean distance between Pt-O was 0.189 nm with a standard deviation of 0.0103 nm, based on ten different measurements across the largest Pt nanoparticle in the white box in Figure 25a. The smallest DFT distance was the O-Al<sub>o</sub> termination at 1.972Å seen in Figure 26a. Figure 26(b-e) show the other simulated interfaces from smallest Pt-O distance to largest Pt-O distance. The O-terminated interfaces provide the closest Pt-O distances when compared to the measured experimental interface distances. Based on comparison of the experiment to the STEM BF simulations, the O-Al<sub>t</sub> terminated interface was eliminated because of the poorer structural match when compared to the O-Al<sub>o</sub> terminated interface. However, the structural match is imperfect. The DFT O-Al<sub>o</sub> interface shows empty octahedral interstitial sites at the interface between every two O-Al<sub>o</sub>-O units. The observed experimental interface appears to have a full occupation of the Al<sub>o</sub> sites next to the oxygen terminated Al<sub>2</sub>O<sub>3</sub> adjacent to the nanoparticle. The experimental interfaces tend to have a low occupancy row beyond the O-Al<sub>o</sub>-O unit at the interface, although this next row of positions is not completely empty in the models.

A question remains regarding why the Pt nanoparticles take on tetrahedral shapes rather than octahedral shapes, which would have a lower surface-to-volume ratio and have the same interfacial orientations. This may be due to the significance of edge energy contributions to the total interfacial energy contributions of the precipitates. It has been calculated for fcc structures that edge energies can cause deviations from the size independent Wulff shape for particle <20nm by a broken bond model [19]. Through this simple model, it was shown that for particles restricted to  $\{111\}$  and  $\{100\}$  faces, it is energetically favorable for particles less than a few nm across, to have only  $\{111\}$  facets. By a similar approach it can be shown that in the same size range (2 to 4 nm) particles with only  $\{111\}_{Pt}$  facets will have tetrahedral shapes stabilized over octahedral shapes due to edge energy contributions.

#### 5.4. Conclusions

Pt nanoparticles in  $\theta$ -alumina that have been processed using thermal annealing of ion implanted and amorphized alumina precipitate into faceted tetrahedral nanoparticles with the orientation relationship of  $(\bar{2}01)_{\theta} \parallel (111)_{Pt}$ ;  $[132]_q \parallel [1\bar{1}0]_{Pt}$ . DFT-based models of five different chemical terminations of  $(\bar{2}01)_{\theta} \parallel (111)_{Pt}$  interfaces associated with this orientation relationship were used to generate Prismatic image simulations to aid in interpretation of atomic-resolution STEM images. The best fitting DFT interfacial model is the O-terminated model with octahedral Al in the second layer from the interface.

## Chapter 5 References

- [1] M. R. Othman, N. N. N. Mustafa, and A. L. Ahmad, "Effect of thermal treatment on the microstructure of sol-gel derived porous alumina modified platinum," *Microporous Mesoporous Mat.*, Article vol. 91, no. 1-3, pp. 268-275, Apr 2006. [Online]. Available: <Go to ISI>://000236656400038
- [2] K. Reszka, "Nanocomposites alumina/Pt produced by PVD and thermal oxidation methods used in catalytic applications," *Vacuum*, Proceedings Paper vol. 81, no. 10, pp. 1202-1206, Jun 2007. [Online]. Available: <Go to ISI>://000248201100021
- [3] J. W. Yoo, D. J. Hathcock, and M. A. El-Sayed, "Propene hydrogenation over truncated octahedral Pt nanoparticles supported on alumina," *Journal of Catalysis*, Article vol. 214, no. 1, pp. 1-7, Feb 2003. [Online]. Available: <Go to ISI>://000182615700001
- [4] J. Libuda, M. Baumer, and H. J. Freund, "Structural Characterization of Platinum Deposits Supported on Ordered Alumina Films," *J. Vac. Sci. Technol. A-Vac. Surf. Films*, Article vol. 12, no. 4, pp. 2259-2264, Jul-Aug 1994. [Online]. Available: <Go to ISI>://A1994NZ03200085
- [5] M. Vaarkamp, J. T. Miller, F. S. Modica, and D. C. Koningsberger, "On the relation between particle morphology, structure of the metal-support interface, and catalytic properties of Pt/ $\gamma$ -Al<sub>2</sub>O<sub>3</sub>," *Journal of Catalysis*, vol. 163, no. 2, pp. 294-305, Oct 1996, doi: 10.1006/jcat.1996.0330.
- [6] J. E. Stulga, P. Wynblatt, and J. K. Tien, "Particle Splitting And Redispersion Phenomena In Model Alumina-Supported Platinum Catalysts," *Journal Of Catalysis*, vol. 62, no. 1, pp. 59-69, 1980. [Online]. Available: <Go to ISI>://A1980JM62600007
- [7] K. Wefers and C. Misra, "Oxides and Hydroxides of Aluminum: Alcoa Technical Paper No. 19, Revised " Alcoa Laboratories, 19, 1987.
- [8] C. W. White *et al.*, "Ion implantation and annealing of crystalline oxides," in *Defect Properties and Processing of High-Technology Nonmetallic Materials Symposium. Boston, MA*, Y. Chen, W. D. Kingery, and R. J. Stokes, Eds., 2-4 Dec. 1986.
- [9] S. Yanagiya and M. Ishida, "Optical and electrical properties of Al<sub>2</sub>O<sub>3</sub> films containing silicon nanocrystals," *Journal of Electronic Materials*, Article vol. 28, no. 5, pp. 496-502, May 1999. [Online]. Available: <Go to ISI>://000080269700016
- [10] A. L. Clauser *et al.*, "Orientation and morphology of Pt nanoparticles in  $\gamma$ -alumina processed via ion implantation and thermal annealing," *Scr. Mater.*, vol. 188, pp. 44-49, 2020.
- [11] M. K. Santala, V. Radmilovic, R. Giulian, M. C. Ridgway, A. M. Glaeser, and R. Gronsky, "Precipitate orientation relationships in Pt-implanted sapphire," *Scripta Materialia*, vol. 62, no. 4, pp. 187-190, 2010, doi: 10.1016/j.scriptamat.2009.10.023.
- [12] S.-H. Cai, S. N. Rashkeev, S. T. Pantelides, and K. Sohlberg, "Phase transformation mechanism between  $\gamma$ - and  $\theta$ -alumina," *Physical Review B*, vol. 67, no. 22, 2003, doi: 10.1103/physrevb.67.224104.
- [13] R. S. Zhou and R. L. Snyder, "Structures and transformation mechanisms of the eta, gamma and theta transition aluminas," *Acta Crystallographica Section B-Structural Science*, Article vol. 47, pp. 617-630, Oct 1991. [Online]. Available: <Go to ISI>://A1991GL01200006
- [14] M. K. Santala, "On Orientation Relationships and Morphologies of Platinum Precipitates in Sapphire," Ph.D., Materials Science and Engineering, University of California, Berkeley, 2009.
- [15] *SRIM/TRIM*. (2003). <http://www.srim.org/>. [Online]. Available: <http://www.srim.org/>

- [16] C. Ophus, J. Ciston, and C. T. Nelson, "Correcting nonlinear drift distortion of scanning probe and scanning transmission electron microscopies from image pairs with orthogonal scan directions," *Ultramicroscopy*, vol. 162, pp. 1-9, 2016, doi: 10.1016/j.ultramic.2015.12.002.
- [17] M. Nord, P. E. Vullum, I. MacLaren, T. Tybell, and R. Holmestad, "Atomap: a new software tool for the automated analysis of atomic resolution images using two-dimensional Gaussian fitting," *Adv Struct Chem Imaging*, vol. 3, no. 1, p. 9, 2017, doi: 10.1186/s40679-017-0042-5.
- [18] C. Ophus, "A fast image simulation algorithm for scanning transmission electron microscopy," *Advanced Structural and Chemical Imaging*, vol. 3, no. 1, 2017, doi: 10.1186/s40679-017-0046-1.
- [19] L. D. Marks, "Particle-Size Effects on Wulff Constructions," *Surface Science*, Article vol. 150, no. 2, pp. 358-366, 1985. [Online]. Available: [Go to ISI://A1985ADW0900007](https://doi.org/10.1016/0029-6455(85)90007-7)

## 6. Concluding Remarks

In this work, a combination of experimental, computational and analytical steps were used to completely characterize the interfacial structure of Pt nanoparticles that have been precipitated in transition alumina through high energy ion implantation and annealing. DFT models were used to create HRSTEM image simulations these were used to validate observational interfacial relationships in aberration corrected TEM images. Both qualitative and quantitative comparisons of the interfacial structures were used to confirm the chemical termination of the observed orientation relationships. Quantitative analysis included measurements of diffraction patterns, directly interpretable images, and computational image analysis.

### 6.1. Viability of the Processing Method

Four separate implantations were done, ranging from a self-implanted sample with no amorphizing Pt to a densely Pt implanted sample with an implantation dose of  $1 \times 10^{17} \text{ cm}^{-2}$ . These implantations were performed to create an amorphized layer of  $\text{Al}_2\text{O}_3$  in a single crystal  $\alpha$ - $\text{Al}_2\text{O}_3$  wafer. Different phases of transition alumina were crystallized depending on the annealing temperature they were processed at. At annealing temperatures of  $800^\circ\text{C}$  a cubic alumina phase developed that was characterized as  $\gamma$ - $\text{Al}_2\text{O}_3$ . Annealing temperatures of  $850^\circ\text{C}$  and greater generated phases with diffraction peaks that can be indexed to either  $\delta$ - $\text{Al}_2\text{O}_3$  or  $\theta$ - $\text{Al}_2\text{O}_3$ . Annealing temperature of  $1000^\circ\text{C}$  were used to generate Pt implanted  $\theta$ - $\text{Al}_2\text{O}_3$ . The result was that the glassy alumina layer recrystallized with a topotaxial relationship to the underlying  $\alpha$ -alumina. This processing method proved that a level of controllability with respect to phase of alumina was achievable using  $\alpha$ - $\text{Al}_2\text{O}_3$  wafers that had been amorphized through implantation.

## 6.2. Platinum Nanoparticles in $\gamma$ -Alumina

Two popular models for bulk  $\gamma$ -alumina were simulated as well as three different chemically terminated interfacial models of the  $(111)_{Pt}(111)_{\gamma}$ ;  $[1\bar{1}0]_{Pt}[1\bar{1}0]_{\gamma}$  orientation relationship. This orientation relationship was first observed using conventional TEM, which then in turn allowed for the development of an oxygen terminated  $(111)_{Pt}(111)_{\gamma}$ ;  $[1\bar{1}0]_{Pt}[1\bar{1}0]_{\gamma}$  DFT interface and two Al terminated DFT interfaces. The developed  $\gamma$ -alumina layer crystalized such that the close packed  $(111)_{\gamma}$ -planes made of layers of oxygen were parallel to the underlying  $\alpha$ -alumina close packed plane  $(0001)_{\alpha}$ . The o-terminated interfacial model provided a good match at the interface of the Pt nanoparticle three atomic planes away from the facet. The nanoparticles observed in the  $\gamma$ -alumina had similar contrast at the facets; using DFT simulations it was confirmed this contrast was likely due to O-Al<sub>o</sub>-O structural units. The Zhou and Smrčok bulk  $\gamma$ -alumina structures were then simulated to gain a better assessment of the bulk atomic structure observed. The simulated O-terminated structure has Pt located directly on top of the terminating O position.

The Smrčok model was a better fit to the experimentally observed  $\gamma$ -alumina in the bulk, this model predicted non-spinel tetrahedral and octahedral Al, which showed a better simulated match to experiments than the Zhou model which proposed atoms in “quasi” octahedral positions.

## 6.3. Platinum Nanoparticles in $\theta$ -Alumina

Pt nanoparticles in  $\theta$ -alumina that have been processed using thermal annealing of ion implanted and amorphized alumina precipitate into faceted tetrahedral nanoparticles with the orientation relationship of  $(\bar{2}01)_{\theta}|| (111)_{Pt}$ ;  $[132]_{\theta}|| [1\bar{1}0]_{Pt}$ . DFT-based models of five different chemical terminations of  $(\bar{2}01)_{\theta}|| (111)_{Pt}$  interfaces associated with this orientation relationship

were used to generate Prismatic image simulations to aid in interpretation of atomic-resolution STEM images. The best fitting DFT interfacial model is the O-terminated model with octahedral Al in the second layer from the interface. There is some variance between the DFT model simulations and the experimental images, but these are likely due to some structural disorder imparted by the presence of Pt nanoparticles with the  $\theta$ -alumina crystal lattice. All the nanoparticles observed in the  $\theta$ -alumina had similar contrast at the facets using DFT simulations it was confirmed this contrast was likely due to O-Al<sub>o</sub>-O structural units

## **Common Bibliography**

- [1] M. A. Alabdullah *et al.*, "A Viewpoint on the Refinery of the Future: Catalyst and Process Challenges," *ACS Catalysis*, vol. 10, no. 15, pp. 8131-8140, 2020, doi: 10.1021/acscatal.0c02209.
- [2] H. Albetran and I. M. Low, "Effect of indium ion implantation on crystallization kinetics and phase transformation of anodized titania nanotubes using in-situ high-temperature radiation diffraction," *Journal of Materials Research*, vol. 31, no. 11, pp. 1588-1595, 2016, doi: 10.1557/jmr.2016.83.
- [3] E. Alves, R. C. da Silva, O. Conde, M. F. da Silva, and J. C. Soares, "Formation of coherent precipitates of platinum in sapphire," *Nucl. Instrum. Methods Phys. Res. Sect. B-Beam Interact. Mater. Atoms*, Article vol. 148, no. 1-4, pp. 1049-1053, Jan 1999. [Online]. Available: [Go to ISI://000078575700196](https://doi.org/10.1016/0168-5822(99)00007-8)
- [4] M. Arai, "Particle size effect and structure sensitivity in catalysis by supported metal catalysts," *JOURNAL OF CHEMICAL ENGINEERING OF JAPAN*, vol. 30, no. 6, pp. 1123-1125, 1997, doi: 10.1252/jcej.30.1123.
- [5] M. Arenz *et al.*, "The Effect of the Particle Size on the Kinetics of CO Electrooxidation on High Surface Area Pt Catalysts," *Journal of the American Chemical Society*, vol. 127, no. 18, pp. 6819-6829, 2005, doi: 10.1021/ja043602h.
- [6] S. M. Augustine and W. M. H. Sachtler, "Variation of catalytic activity over platinum-rhenium/.gamma.-alumina," vol. 91, no. 23, pp. 5953-5956, 1987, doi: 10.1021/j100307a028.
- [7] H. O. Ayoola *et al.*, "Probing the Local Bonding at the Pt/ $\gamma$ -Al<sub>2</sub>O<sub>3</sub> Interface," *The Journal of Physical Chemistry C*, vol. 124, no. 18, pp. 9876-9885, 2020, doi: 10.1021/acs.jpcc.9b12029.
- [8] H. O. Ayoola, S. D. House, C. S. Bonifacio, K. Kisslinger, W. A. Saidi, and J. C. Yang, "Evaluating the accuracy of common  $\gamma$ -Al<sub>2</sub>O<sub>3</sub> structure models by selected area electron diffraction from high-quality crystalline  $\gamma$ -Al<sub>2</sub>O<sub>3</sub>," *Acta Materialia*, vol. 182, pp. 257-266, 2020, doi: 10.1016/j.actamat.2019.10.027.
- [9] V. Balzani, G. Pacchioni, M. Prato, and A. Zecchina, "Solar-driven chemistry: towards new catalytic solutions for a sustainable world," *Rendiconti Lincei. Scienze Fisiche e Naturali*, vol. 30, no. 3, pp. 443-452, 2019, doi: 10.1007/s12210-019-00836-2.
- [10] N. P. Barradas *et al.*, "International Atomic Energy Agency intercomparison of ion beam analysis software," *Nuclear Instruments & Methods in Physics Research Section B-Beam Interactions with Materials and Atoms*, vol. 262, no. 2, pp. 281-303, Sep 2007, doi: 10.1016/j.nimb.2007.05.018.
- [11] J. J. Berzelius, "Årsberöttelsen om framsteg i fysik och kemi," *Royal Swedish Academy of Sciences*, 1835.
- [12] D. W. Blakely and G. A. Somorjai, "The stability and structure of high miller index platinum crystal surfaces in vacuum and in the presence of adsorbed carbon and oxygen," *Surface Science*, vol. 65, no. 2, pp. 419-442, 1977, doi: 10.1016/0039-6028(77)90457-5.
- [13] J. D. Budai, C. W. White, S. P. Withrow, M. F. Chisholm, J. Zhu, and R. A. Zuhr, "Controlling the size, structure and orientation of semiconductor nanocrystals using metastable phase recrystallization," *Nature*, vol. 390, no. 6658, pp. 384-386, 1997, doi: 10.1038/37079.

- [14] S.-H. Cai, S. N. Rashkeev, S. T. Pantelides, and K. Sohlberg, "Phase transformation mechanism between  $\gamma$ - and  $\theta$ -alumina," *Phys. Rev. B*, vol. 67, no. 22, 2003, doi: 10.1103/physrevb.67.224104.
- [15] J. Choi and S. J. An, "Effects of arsenic implantation and rapid thermal annealing on ZnO nanorods for p-type doping," *Journal of Vacuum Science & Technology B*, vol. 38, no. 5, 2020, doi: 10.1116/6.0000041.
- [16] A. L. Clauser *et al.*, "Orientation and morphology of Pt nanoparticles in  $\gamma$ -alumina processed via ion implantation and thermal annealing," *Scripta Materialia*, vol. 188, pp. 44-49, 2020.
- [17] H. Cong and J. A. Porco, "Chemical Synthesis of Complex Molecules Using Nanoparticle Catalysis," *ACS Catalysis*, vol. 2, no. 1, pp. 65-70, 2012, doi: 10.1021/cs200495s.
- [18] D. Coster, A. L. Blumenfeld, and J. J. Fripiat, "Lewis Acid Sites and Surface Aluminum in Aluminas and Zeolites: A High-Resolution NMR Study," *The Journal of Physical Chemistry*, vol. 98, no. 24, pp. 6201-6211, 1994, doi: 10.1021/j100075a024.
- [19] J. M. Cowley and A. F. Moodie, "The Scattering of Electrons by Atoms and Crystals. I. A New Theoretical Approach," *Acta Cryst.*, vol. 10, pp. 609-619, 1957, doi: 10.1107/s0365110x57002194
- [20] U. Dahmen, S. Q. Xiao, S. Paciornik, E. Johnson, and A. Johansen, "Magic-size equilibrium shapes of nanoscale Pb inclusions in Al," *Phys. Rev. Lett.*, Article vol. 78, no. 3, pp. 471-474, Jan 1997. [Online]. Available: <Go to ISI>://A1997WC79800019
- [21] A. Dandapat, D. Jana, and G. De, "Synthesis of Thick Mesoporous  $\gamma$ -Alumina Films, Loading of Pt Nanoparticles, and Use of the Composite Film as a Reusable Catalyst," *ACS Applied Materials & Interfaces*, vol. 1, no. 4, pp. 833-840, 2009, doi: 10.1021/am800241x.
- [22] N. A. Deskins, D. H. Mei, and M. Dupuis, "Adsorption and diffusion of a single Pt atom on  $\gamma$ -Al<sub>2</sub>O<sub>3</sub> surfaces," *Surface Science*, vol. 603, no. 17, pp. 2793-2807, Sep 2009, doi: 10.1016/j.susc.2009.07.021.
- [23] M. Digne, P. Sautet, P. Raybaud, P. Euzen, and H. Toulhoat, "Hydroxyl Groups on  $\gamma$ -Alumina Surfaces: A DFT Study," *Journal of Catalysis*, vol. 211, no. 1, pp. 1-5, 2002, doi: 10.1006/jcat.2002.3741.
- [24] M. Digne, P. Sautet, P. Raybaud, P. Euzen, and H. Toulhoat, "Use of DFT to achieve a rational understanding of acid-basic properties of  $\gamma$ -alumina surfaces," *Journal of Catalysis*, vol. 226, no. 1, pp. 54-68, Aug 2004, doi: 10.1016/j.jcat.2004.04.020.
- [25] L. R. Doolittle, "Algorithms for the Rapid Simulation of Rutherford Backscattering Spectra," *Nuclear Instruments and Methods in Physics Research*, vol. 9, no. 3, B, pp. 344-351, June 1984, doi: 10.1016/0168-583X(85)90762-1.
- [26] P. Eklund, M. Sridharan, G. Singh, and J. Bøttiger, "Thermal Stability and Phase Transformations of  $\gamma$ -Amorphous-Al<sub>2</sub>O<sub>3</sub> Thin Films," *Plasma Processes and Polymers*, vol. 6, no. S1, pp. S907-S911, 2009, doi: 10.1002/ppap.200932301.
- [27] G. Ertl, H. Knözinger, and J. Weitkamp, *The Handbook of Heterogeneous Catalysis*. Weinheim: Wiley-VCH, 1997.
- [28] G. C. Farlow, P. S. Sklad, C. W. White, C. J. McHargue, and B. R. Appleton, "The Formation and Annealing of Amorphous Layers of Al<sub>2</sub>O<sub>3</sub>," in *Materials Research Symposium*, 1985, vol. 60, doi: 10.1557/proc-60-387

- [29] M. Gandman, M. Ridgway, R. Gronsky, and A. M. Glaeser, "Microstructural evolution in Pt-implanted polycrystalline Al<sub>2</sub>O<sub>3</sub>," *Acta Materialia*, vol. 83, pp. 169-179, Jan 2015, doi: 10.1016/j.actamat.2014.09.045.
- [30] F. Gao and D. W. Goodman, "Model Catalysts: Simulating the Complexities of Heterogeneous Catalysts," *Annual Review of Physical Chemistry*, vol. 63, no. 1, pp. 265-286, 2012, doi: 10.1146/annurev-physchem-032511-143722.
- [31] H. Ginsberg, W. Huttig, and G. Strunk-Lichtenberg, "Über den Einfluß des Ausgangsmaterials auf die beim thermischen Abbau bzw. Umbau von Aluminiumhydroxyden entstehenden kristallinen Formen. I. Die kristallinen Formen des Thermischen Abbaues der  $\gamma$ -Aluminiumhydroxyde," *Zeitschrift für Anorganische Chemie*, vol. 293, no. 1-2, pp. 33-46, 1957.
- [32] K. A. Goulas, A. V. Mironenko, G. R. Jenness, T. Mazal, and D. G. Vlachos, "Fundamentals of C–O bond activation on metal oxide catalysts," *Nature Catalysis*, vol. 2, no. 3, pp. 269-276, 2019, doi: 10.1038/s41929-019-0234-6.
- [33] L. He, Y. Fan, L. Luo, J. Bellettre, and J. Yue, "Preparation of Pt/ $\gamma$ -Al<sub>2</sub>O<sub>3</sub> catalyst coating in microreactors for catalytic methane combustion," *Chemical Engineering Journal*, vol. 380, p. 122424, 2020, doi: 10.1016/j.cej.2019.122424.
- [34] C. R. Henry, "Surface studies of supported model catalysts," *Surface Science Reports*, vol. 31, no. 7-8, pp. 231-325, 1998, doi: 10.1016/s0167-5729(98)00002-8.
- [35] X.-M. Hu and K. Daasbjerg, "Molecular catalyst converts carbon dioxide to methanol," *Nature*, vol. 575, no. 7784, pp. 598-599, 2019, doi: 10.1038/d41586-019-03563-8.
- [36] A. Ionescu, A. Allouche, J. P. Aycard, M. Rajzmann, and F. Hutschka, "Study of gamma-alumina surface reactivity: Adsorption of water and hydrogen sulfide on octahedral aluminum sites," *Journal of Physical Chemistry B*, vol. 106, no. 36, pp. 9359-9366, Sep 2002, doi: 10.1021/jp020145n.
- [37] K. Ishizuka, "A practical approach for STEM image simulation based on the FFT multislice method," *Ultramicroscopy*, vol. 90, no. 2-3, pp. 71-83, 2002, doi: 10.1016/s0304-3991(01)00145-0.
- [38] Y. Iwasawa, R. Mason, M. Textor, and G. A. Somorjai, "The reactions of carbon monoxide at coordinatively unsaturated sites on a platinum surface," *Chemical Physics Letters*, vol. 44, no. 3, pp. 486-470, 1976, doi: 10.1016/0009-2614(76)80706-3.
- [39] J. Jefferson, "Swords to Plowshares - A Short History of ORNL," S. Wyatt, Ed., ed. Oak Ridge TN: Oak Ridge Office of Public Affairs, 1993.
- [40] G. R. Jenness, M. A. Christiansen, S. Caratzoulas, D. G. Vlachos, and R. J. Gorte, "Site-Dependent Lewis Acidity of  $\gamma$ -Al<sub>2</sub>O<sub>3</sub> and Its Impact on Ethanol Dehydration and Etherification," *The Journal of Physical Chemistry C*, vol. 118, no. 24, pp. 12899-12907, 2014, doi: 10.1021/jp5028349.
- [41] Y. Jin, H. Xu, and A. K. Datye, "Electron energy loss spectroscopy (EELS) of iron Fischer-Tropsch catalysts," *Microsc Microanal*, vol. 12, no. 2, pp. 124-34, Apr 2006, doi: 10.1017/S1431927606060144.
- [42] Y. Kanda, T. Kobayashi, Y. Uemichi, and M. Sugioka, "Catalytic Performance of Noble Metals Supported on Alumina-modified Silica Gel for Hydrodesulfurization Reaction," *Journal of Japan Petroleum Institute*, vol. 2, pp. 49-56, 2006.
- [43] J. Kašpar, P. Fornasiero, and N. Hickey, "Automotive catalytic converters: current status and some perspectives," *Catalysis Today*, vol. 77, no. 4, pp. 419-449, 2003, doi: 10.1016/s0920-5861(02)00384-x.

- [44] T. G. Kaufmann, A. Kaldor, G. F. Stuntz, M. C. Kerby, and L. L. Ansell, "Catalysis science and technology for cleaner transportation fuels," *Catalysis Today*, vol. 62, no. 1, pp. 77-90, 2000, doi: 10.1016/s0920-5861(00)00410-7.
- [45] K. J. Kirkby and R. P. Webb, "Ion Implanted Nanostructures," in *Encyclopedia of Nanoscience and Nanotechnology* vol. 4, H. S. Nalwa, Ed., ed. University of Surrey, Guildford, Surrey, United Kingdom, 2004, pp. 1-11.
- [46] H. Knozinger, "Acid and Basic Properties of Aluminas in relation to their properties as catalysts and supports," *Catalysis by Acids and Bases*, pp. 111-125, 1985.
- [47] Konstantin Khivantsev, †,\* Nicholas R. Jaegers,<sup>1,2</sup> † Ja-Hun Kwak,<sup>3,\*</sup> Janos Szanyi,<sup>1,\*</sup> and Libor Kovarik<sup>1,†,\*</sup>, "Precise identification and characterization of catalytically active sites on the surface of  $\gamma$ -alumina."
- [48] N. Kornienko, J. Z. Zhang, K. K. Sakimoto, P. Yang, and E. Reisner, "Interfacing nature's catalytic machinery with synthetic materials for semi-artificial photosynthesis," *Nature Nanotechnology*, vol. 13, no. 10, pp. 890-899, 2018, doi: 10.1038/s41565-018-0251-7.
- [49] L. Kovarik, M. Bowden, A. Genc, J. Szanyi, C. H. F. Peden, and J. H. Kwak, "Structure of  $\delta$ -Alumina: Toward the Atomic Level Understanding of Transition Alumina Phases," *The Journal of Physical Chemistry C*, vol. 118, no. 31, pp. 18051-18058, 2014, doi: 10.1021/jp500051j.
- [50] L. Kovarik *et al.*, "Unraveling the Origin of Structural Disorder in High Temperature Transition  $\text{Al}_2\text{O}_3$ : Structure of theta- $\text{Al}_2\text{O}_3$ ," *Chemistry of Materials*, vol. 27, no. 20, pp. 7042-7049, Oct 2015, doi: 10.1021/acs.chemmater.5b02523.
- [51] L. Kovarik *et al.*, "Tomography and High-Resolution Electron Microscopy Study of Surfaces and Porosity in a Plate-like gamma- $\text{Al}_2\text{O}_3$ ," *Journal of Physical Chemistry C*, vol. 117, no. 1, pp. 179-186, Jan 2013, doi: 10.1021/jp306800h.
- [52] X. Krokidis, P. Raybaud, A.-E. Gobichon, B. Rebours, P. Euzen, and H. Toulhoat, "Theoretical Study of the Dehydration Process of Boehmite to  $\gamma$ -Alumina," *The Journal of Physical Chemistry B*, vol. 105, no. 22, pp. 5121-5130, 2001, doi: 10.1021/jp0038310.
- [53] J. H. Kwak *et al.*, "Coordinatively Unsaturated  $\text{Al}^{3+}$  Centers as Binding Sites for Active Catalyst Phases of Platinum on  $\gamma$ - $\text{Al}_2\text{O}_3$ ," *Science*, vol. 325, 2009.
- [54] S. Lamouri *et al.*, "Control of the  $\gamma$ -alumina to  $\alpha$ -alumina phase transformation for an optimized alumina densification," *Boletín de la Sociedad Española de Cerámica y Vidrio*, vol. 56, no. 2, pp. 47-54, 2017, doi: 10.1016/j.bsecv.2016.10.001.
- [55] S. Lan, N. Guo, L. Liu, X. Wu, L. Li, and S. Gan, "Facile preparation of hierarchical hollow structure gamma alumina and a study of its adsorption capacity," *Applied Surface Science*, vol. 283, pp. 1032-1040, 2013, doi: 10.1016/j.apsusc.2013.07.064.
- [56] J. M. Lebeau, S. D. Findlay, L. J. Allen, and S. Stemmer, "Standardless Atom Counting in Scanning Transmission Electron Microscopy," *Nano Letters*, vol. 10, no. 11, pp. 4405-4408, 2010, doi: 10.1021/nl102025s.
- [57] T. Letcher, *Comprehensive Renewable Energy*. London, UNITED KINGDOM: Elsevier, 2012.
- [58] I. Levin and D. Brandon, "Metastable alumina polymorphs: Crystal structures and transition sequences," *Journal of the American Ceramic Society*, vol. 81, no. 8, pp. 1995-2012, Aug 1998. [Online]. Available: <Go to ISI>://WOS:000075368600002.

- [59] I. Levin, T. Gemming, and D. G. Brandon, "Some metastable polymorphs and transient stages of transformation in alumina," *Phys. Status Solidi A-Appl. Res.*, Article vol. 166, no. 1, pp. 197-218, Mar 1998. [Online]. Available: <Go to ISI>://000072976500019
- [60] J. Libuda, M. Baumer, and H. J. Freund, "Structural Characterization of Platinum Deposits Supported on Ordered Alumina Films," *J. Vac. Sci. Technol. A-Vac. Surf. Films*, Article vol. 12, no. 4, pp. 2259-2264, Jul-Aug 1994. [Online]. Available: <Go to ISI>://A1994NZ03200085
- [61] M. K. Linnarsson, A. Hallén, and L. Vines, "Influence of a thin amorphous surface layer on de-channeling during aluminum implantation at different temperatures into 4H-SiC," *Applied Physics A*, vol. 125, no. 12, 2019, doi: 10.1007/s00339-019-3144-1.
- [62] B. C. Lippens and J. H. De Boer, "Study of phase transformations during calcination of aluminum hydroxides by selected area electron diffraction," *Acta Cryst.*, vol. 17, p. 1312, 1964, doi: 10.1107/S0365110X64003267.
- [63] Y. Liu *et al.*, "Hydrothermal synthesis of microscale boehmite and gamma nanoleaves alumina," *Materials Letters*, vol. 62, no. 8-9, pp. 1297-1301, 2008, doi: 10.1016/j.matlet.2007.08.067.
- [64] E. Lodyga-Chruscinska, A. Sykula-Zajac, and D. Olejnik, "Determination of nickel in Polish brands of margarines," *Food Addit Contam Part B Surveill*, vol. 5, no. 4, pp. 251-4, 2012, doi: 10.1080/19393210.2012.702287.
- [65] C. Mager-Maury, G. Bonnard, C. Chizallet, P. Sautet, and P. Raybaud, "H-2-Induced Reconstruction of Supported Pt Clusters: Metal-Support Interaction versus Surface Hydride," *Chemcatchem*, vol. 3, no. 1, pp. 200-207, Jan 2011, doi: 10.1002/cctc.201000324.
- [66] C. Mager-Maury, C. Chizallet, P. Sautet, and P. Raybaud, "Platinum Nanoclusters Stabilized on  $\gamma$ -Alumina by Chlorine Used As a Capping Surface Ligand: A Density Functional Theory Study," *ACS Catalysis*, vol. 2, no. 7, pp. 1346-1357, 2012, doi: 10.1021/cs300178y.
- [67] L. D. Marks, "Particle-Size Effects on Wulff Constructions," *Surface Science*, Article vol. 150, no. 2, pp. 358-366, 1985. [Online]. Available: <Go to ISI>://A1985ADW0900007
- [68] L. D. Marks, "Experimental studies of small-particle structures," *Reports on Progress in Physics*, vol. 57, no. 6, pp. 603-649, Jun 1994, doi: 10.1088/0034-4885/57/6/002.
- [69] A. Meldrum, R. F. Haglund, L. A. Boatner, and C. W. White, "Nanocomposite materials formed by ion implantation," *Advanced Materials*, vol. 13, no. 19, pp. 1431-1444, Oct 2001, doi: 10.1002/1521-4095(200110)13:19<1431::Aid-adma1431>3.0.Co;2-z.
- [70] K. J. Morrissey, K. K. Czanderna, R. P. Merrill, and C. B. Carter, "Transition alumina structures studied using HREM," (in English), *Ultramicroscopy*, Article vol. 18, no. 1-4, pp. 379-385, 1985, doi: 10.1016/0304-3991(85)90156-1.
- [71] L. Nguyen, F. F. Tao, Y. Tang, J. Dou, and X. J. Bao, "Understanding Catalyst Surfaces during Catalysis through Near Ambient Pressure X-ray Photoelectron Spectroscopy," *Chem Rev*, vol. 119, no. 12, pp. 6822-6905, Jun 26 2019, doi: 10.1021/acs.chemrev.8b00114.
- [72] M. Nord, P. E. Vullum, I. MacLaren, T. Tybell, and R. Holmestad, "Atomap: a new software tool for the automated analysis of atomic resolution images using two-dimensional Gaussian fitting," *Adv Struct Chem Imaging*, vol. 3, no. 1, p. 9, 2017, doi: 10.1186/s40679-017-0042-5.

- [73] P. Normand *et al.*, "Nanocrystals manufacturing by ultra-low-energy ion-beam-synthesis for non-volatile memory applications," *Nuclear Instruments & Methods in Physics Research Section B-Beam Interactions with Materials and Atoms*, vol. 216, pp. 228-238, Feb 2004, doi: 10.1016/j.nimb.2003.11.039.
- [74] C. Ophus, "A fast image simulation algorithm for scanning transmission electron microscopy," *Advanced Structural and Chemical Imaging*, vol. 3, no. 1, 2017, doi: 10.1186/s40679-017-0046-1.
- [75] C. Ophus, J. Ciston, and C. T. Nelson, "Correcting nonlinear drift distortion of scanning probe and scanning transmission electron microscopies from image pairs with orthogonal scan directions," *Ultramicroscopy*, vol. 162, pp. 1-9, 2016, doi: 10.1016/j.ultramic.2015.12.002.
- [76] C. Ophus, M. K. Santala, M. Asta, and V. Radmilovic, "Structure and phase transitions at the interface between alpha-Al<sub>2</sub>O<sub>3</sub> and Pt," *J Phys Condens Matter*, vol. 25, no. 23, p. 232202, Jun 12 2013, doi: 10.1088/0953-8984/25/23/232202.
- [77] M. R. Othman, N. N. N. Mustafa, and A. L. Ahmad, "Effect of thermal treatment on the microstructure of sol-gel derived porous alumina modified platinum," *Microporous Mesoporous Mat.*, Article vol. 91, no. 1-3, pp. 268-275, Apr 2006. [Online]. Available: <Go to ISI>://000236656400038
- [78] K. Oware Sarfo, A. L. Clauser, M. K. Santala, and L. Árnadóttir, "On the atomic structure of Pt(1 1 1)/ $\gamma$ -Al<sub>2</sub>O<sub>3</sub>(1 1 1) interfaces and the changes in their interfacial energy with temperature and oxygen pressure," *Applied Surface Science*, vol. 542, 2021, doi: 10.1016/j.apsusc.2020.148594.
- [79] K. Oware Sarfo, A. L. Clauser, M. K. Santala, and L. Árnadóttir, "Ab initio study of the stability and electronic structure of Pt/ $\gamma$ -Al<sub>2</sub>O<sub>3</sub> interfaces using density functional theory," *Applied Surface Science*, submitted 2020, in review.
- [80] G. Paglia *et al.*, "Boehmite Derived  $\gamma$ -Alumina System. 1. Structural Evolution with Temperature, with the Identification and Structural Determination of a New Transition Phase,  $\gamma'$ -Alumina," *Chem. Materia.*, vol. 16, pp. 220-236, 2004, doi: 10.1021/cm034917j.
- [81] G. Paglia *et al.*, "Tetragonal structure model for boehmite-derived gamma-alumina," *Phys. Rev. B*, vol. 68, no. 14, Oct 2003, Art no. 144110, doi: 10.1103/PhysRevB.68.144110.
- [82] G. Paglia, A. L. Rohl, C. E. Buckley, and J. D. Gale, "Determination of the structure of gamma-alumina from interatomic potential and first-principles calculations: The requirement of significant numbers of nonspinel positions to achieve an accurate structural model," *Phys. Rev. B*, vol. 71, no. 22, Jun 2005, Art no. 224115, doi: 10.1103/PhysRevB.71.224115.
- [83] V. P. Pakharukova, I. Y. Pakharukov, V. I. Bukhtiyarov, and V. N. Parmon, "Alumina-supported platinum catalysts: Local atomic structure and catalytic activity for complete methane oxidation," *Applied Catalysis A: General*, vol. 486, pp. 12-18, 2014, doi: 10.1016/j.apcata.2014.08.014.
- [84] L. Pauling and S. B. Hendricks, "The Crystal Structures of Hematite and Corundum," *Journal of the American Chemical Society*, vol. 47, no. 3, pp. 781-790, 1925, doi: 10.1021/ja01680a027.
- [85] C. Pecharrroman, I. Sobrados, J. E. Iglesias, T. Gonzalez-Carreno, and J. Sanz, "Thermal evolution of transitional aluminas followed by NMR and IR spectroscopies," *Journal of*

- Physical Chemistry B*, vol. 103, no. 30, pp. 6160-6170, Jul 29 1999, doi: 10.1021/jp983316q.
- [86] H. Pines and W. O. Haag, "Alumina: Catalyst and Support. I. Alumina, its Intrinsic Acidity and Catalytic Activity 1," vol. 82, no. 10, pp. 2471-2483, 1960, doi: 10.1021/ja01495a021.
- [87] H. P. Pinto, R. M. Nieminen, and S. D. Elliott, "Ab initio study of  $\gamma$ -Al<sub>2</sub>O<sub>3</sub> surfaces," vol. 70, no. 12, 2004, doi: 10.1103/physrevb.70.125402.
- [88] A. Pryor, C. Ophus, and J. Miao, "A streaming multi-GPU implementation of image simulation algorithms for scanning transmission electron microscopy," *Advanced Structural and Chemical Imaging*, vol. 3, no. 1, 2017, doi: 10.1186/s40679-017-0048-z.
- [89] P. Raybaud, C. Chizallet, C. Mager-Maury, M. Digne, H. Toulhoat, and P. Sautet, "From  $\gamma$ -alumina to supported platinum nanoclusters in reforming conditions: 10years of DFT modeling and beyond," *Journal of Catalysis*, vol. 308, pp. 328-340, 2013, doi: 10.1016/j.jcat.2013.08.015.
- [90] K. Reszka, "Nanocomposites alumina/Pt produced by PVD and thermal oxidation methods used in catalytic applications," *Vacuum*, Proceedings Paper vol. 81, no. 10, pp. 1202-1206, Jun 2007. [Online]. Available: <Go to ISI>://000248201100021
- [91] W. G. Rothschild, H. C. Yao, and H. K. Plummer, "Surface interaction in the platinum- $\gamma$ -alumina system. V. Effects of atmosphere and fractal topology on the sintering of platinum," *Langmuir*, vol. 2, no. 5, pp. 588-593, 1986, doi: 10.1021/la00071a010.
- [92] L. Samain *et al.*, "Structural analysis of highly porous  $\gamma$ -Al<sub>2</sub>O<sub>3</sub>," *Journal of Solid State Chemistry*, vol. 217, pp. 1-8, 2014, doi: 10.1016/j.jssc.2014.05.004.
- [93] M. K. Santala, "On Orientation Relationships and Morphologies of Platinum Precipitates in Sapphire," Ph.D., Materials Science and Engineering, University of California, Berkeley, 2009.
- [94] M. K. Santala, V. Radmilovic, R. Giulian, M. C. Ridgway, A. M. Glaeser, and R. Gronsky, "Precipitate orientation relationships in Pt-implanted sapphire," vol. 62, no. 4, pp. 187-190, 2010, doi: 10.1016/j.scriptamat.2009.10.023.
- [95] M. K. Santala, V. Radmilovic, R. Giulian, M. C. Ridgway, R. Gronsky, and A. M. Glaeser, "The orientation and morphology of platinum precipitates in sapphire," vol. 59, no. 12, pp. 4761-4774, 2011, doi: 10.1016/j.actamat.2011.04.012.
- [96] P. Santiago, L. Rendon, C. Reza-San German, and U. Pal, "HAADF imaging: an effective technique for the study of nonhomogeneous nanostructures," *J Nanosci Nanotechnol*, vol. 5, no. 7, pp. 1172-6, Jul 2005, doi: 10.1166/jnn.2005.139.
- [97] B. K. Singh, S. Lee, and K. Na, "An overview on metal-related catalysts: metal oxides, nanoporous metals and supported metal nanoparticles on metal organic frameworks and zeolites," *Rare Metals*, vol. 39, no. 7, pp. 751-766, 2019, doi: 10.1007/s12598-019-01205-6.
- [98] W. Sinkler, S. Bradley, U. Ziese, and K. D. Jong, "3D-TEM Study of Gamma Alumina Catalyst Supports," *Microscopy and Microanalysis*, vol. 12, no. S02, pp. 52-53, 2006, doi: 10.1017/s1431927606067869.
- [99] M. W. Small, S. I. Sanchez, L. D. Menard, J. H. Kang, A. I. Frenkel, and R. G. Nuzzo, "The atomic structural dynamics of gamma-Al<sub>2</sub>O<sub>3</sub> supported Ir-Pt nanocluster catalysts prepared from a bimetallic molecular precursor: a study using aberration-corrected electron microscopy and X-ray absorption spectroscopy," *J Am Chem Soc*, vol. 133, no. 10, pp. 3582-91, Mar 16 2011, doi: 10.1021/ja110033g.

- [100] L. Smrcok, V. Langer, and J. Krestan, "Gamma-alumina: a single-crystal X-ray diffraction study," *Acta Crystallogr C*, vol. 62, no. Pt 9, pp. i83-4, Sep 2006, doi: 10.1107/S0108270106026850.
- [101] J. E. Stulga, P. Wynblatt, and J. K. Tien, "Particle Splitting And Redispersion Phenomena In Model Alumina-Supported Platinum Catalysts," *Journal Of Catalysis*, vol. 62, no. 1, pp. 59-69, 1980. [Online]. Available: <Go to ISI>://A1980JM62600007
- [102] H. C. Stumpf, A. S. Russell, J. W. Newsome, and C. M. Tucker, "Thermal Transformations of Aluminas and Alumina Hydrates - Reaction with 44% Technical Acid," *Industrial & Engineering Chemistry*, vol. 42, no. 7, pp. 1398-1403, 1950, doi: 10.1021/ie50487a039.
- [103] S. J. Tauster and S. C. Fung, "Strong Metal-Support Interactions: Occurrence among the binary oxides of group IIA-VB," *Journal of Catalysis*, vol. 55, pp. 29-35, 1978.
- [104] S. J. Tauster, S. C. Fung, and R. L. Garten, "Strong Metal-Support Interactions. Group 8 Noble Metals Supported on TiO<sub>2</sub>," *Journal of the American Chemical Society*, vol. 100, pp. 170-175, 1978.
- [105] M. E. Thompson, C. S. Su, and P. W. Voorhees, "The Equilibrium Shape of a Misfitting Precipitate," *Acta Metallurgica Et Materialia*, vol. 42, no. 6, pp. 2107-2122, Jun 1994. [Online]. Available: <Go to ISI>://A1994NM40100034
- [106] M. Trueba and S. P. Trasatti, "Gamma-alumina as a support for catalysts: A review of fundamental aspects," *European Journal of Inorganic Chemistry*, no. 17, pp. 3393-3403, Sep 2005, doi: 10.1002/ejic.200500348.
- [107] M. Vaarkamp, J. T. Miller, F. S. Modica, and D. C. Koningsberger, "On the relation between particle morphology, structure of the metal-support interface, and catalytic properties of Pt/gamma-Al<sub>2</sub>O<sub>3</sub>," *Journal of Catalysis*, vol. 163, no. 2, pp. 294-305, Oct 1996, doi: 10.1006/jcat.1996.0330.
- [108] J. C. Vedrine, "Heterogeneous Catalysis on Metal Oxides," *Catalysts*, vol. 7, no. 11, Nov 2017, Art no. 341, doi: 10.3390/catal7110341.
- [109] K. Wefers and C. Misra, "Oxides and Hydroxides of Aluminum," *Alcoa Technical Paper*, vol. 19, 1987.
- [110] K. Wefers and C. Misra, "Oxides and Hydroxides of Aluminum: Alcoa Technical Paper No. 19, Revised " Alcoa Laboratories, 19, 1987.
- [111] C. W. White *et al.*, "Ion Implantation and Annealing of Oxides," *Nuclear Instruments and Methods in Physics Research*, no. B32, pp. 11-22, 1987.
- [112] C. W. White *et al.*, "Ion-Implantation and Annealing of Crystalline Oxides and Ceramic Materials," *Nuclear Instruments & Methods in Physics Research Section B-Beam Interactions with Materials and Atoms*, vol. 32, no. 1-4, pp. 11-22, May 1988. [Online]. Available: <Go to ISI>://A1988N937400003
- [113] C. W. White, C. J. McHargue, P. S. Sklad, L. A. Boatner, and G. C. Farlow, "Ion implantation and annealing of crystalline oxides," *Material Science Reports*, vol. 4, no. 2-3, pp. 41-146, July 1989, doi: 10.1016/s0920-2307(89)80005-2.
- [114] C. W. White *et al.*, "Ion implantation and annealing of crystalline oxides," in *Defect Properties and Processing of High-Technology Nonmetallic Materials Symposium. Boston, MA*, Y. Chen, W. D. Kingery, and R. J. Stokes, Eds., 2-4 Dec. 1986.
- [115] C. W. White *et al.*, "Ferromagnetic FePt nanoparticles formed in Al<sub>2</sub>O<sub>3</sub> by ion implantation," *Nucl. Instrum. Methods Phys. Res. Sect. B-Beam Interact. Mater. Atoms*,

- Article vol. 191, pp. 437-441, May 2002. [Online]. Available: [Go to ISI://000176692300085](http://www.isinet.com/000176692300085)
- [116] C. W. White *et al.*, "Oriented ferromagnetic Fe-Pt alloy nanoparticles produced in Al<sub>2</sub>O<sub>3</sub> by ion-beam synthesis," *Journal of Applied Physics*, vol. 93, no. 9, pp. 5656-5669, 2003, doi: 10.1063/1.1565691.
- [117] D. B. Williams and C. B. Carter, 2, Ed. *Transmission Electron Microscopy*. Springer, 2009.
- [118] S. J. Wilson, "Dehydration Of Boehmite, Gamma-AlOOH, To Gamma-Al<sub>2</sub>O<sub>3</sub>," (in English), *Journal of Solid State Chemistry*, Article vol. 30, no. 2, pp. 247-255, 1979, doi: 10.1016/0022-4596(79)90106-3.
- [119] J. Wisniak, "The History of Catalysis. From the Beginning to Nobel Prizes," *Educación Química*, vol. 21, no. 1, pp. 60-69, 2010, doi: 10.1016/s0187-893x(18)30074-0.
- [120] C. Wolverton and K. C. Hass, "Phase stability and structure of spinel-based transition aluminas," vol. 63, no. 2, 2000, doi: 10.1103/physrevb.63.024102.
- [121] C. Wolverton and K. C. Hass, "Phase stability and structure of spinel-based transition aluminas," *Phys. Rev. B*, Article vol. 6302, no. 2, p. 024102, Jan 2001. [Online]. Available: [Go to ISI://000166382200013](http://www.isinet.com/000166382200013)
- [122] P. Wynblatt and D. Chatain, "Two-dimensional versus three-dimensional constraints in hetero-epitaxy/orientation relationships," *Journal of Materials Science*, vol. 52, no. 16, pp. 9630-9639, Aug 2017, doi: 10.1007/s10853-017-1145-z.
- [123] S. Yanagiya and M. Ishida, "Optical and electrical properties of Al<sub>2</sub>O<sub>3</sub> films containing silicon nanocrystals," *J. Electron. Mater.*, Article vol. 28, no. 5, pp. 496-502, May 1999. [Online]. Available: [Go to ISI://000080269700016](http://www.isinet.com/000080269700016)
- [124] E. Yang *et al.*, "Acidic effect of porous alumina as supports for Pt nanoparticle catalysts in n-hexane reforming," *Catalysis Science & Technology*, vol. 8, no. 13, pp. 3295-3303, 2018, doi: 10.1039/c8cy00776d.
- [125] J. C. Yang, E. Schumann, I. Levin, and M. Ruhle, "Transient oxidation of NiAl," *Acta Materialia*, vol. 46, no. 6, pp. 2195-2201, Mar 23 1998, doi: 10.1016/s1359-6454(97)00378-9.
- [126] J.-H. Yi, Y.-Y. Sun, J.-F. Gao, and C.-Y. Xu, "Synthesis of crystalline  $\gamma$ -Al<sub>2</sub>O<sub>3</sub> with high purity," *Transactions of Nonferrous Metals Society of China*, vol. 19, no. 5, pp. 1237-1242, 2009, doi: 10.1016/s1003-6326(08)60435-5.
- [127] J. W. Yoo, D. J. Hathcock, and M. A. El-Sayed, "Propene hydrogenation over truncated octahedral Pt nanoparticles supported on alumina," *Journal of Catalysis*, Article vol. 214, no. 1, pp. 1-7, Feb 2003. [Online]. Available: [Go to ISI://000182615700001](http://www.isinet.com/000182615700001)
- [128] N. Yu, P. C. McIntyre, M. Nastasi, and K. E. Sickafus, "High-quality epitaxial growth of  $\gamma$  -alumina films on  $\alpha$  -alumina sapphire induced by ion-beam bombardment," vol. 52, no. 24, pp. 17518-17522, 1995, doi: 10.1103/physrevb.52.17518.
- [129] L. Zhang, A. M. Karim, M. H. Engelhard, Z. Wei, D. L. King, and Y. Wang, "Correlation of Pt-Re surface properties with reaction pathways for the aqueous-phase reforming of glycerol," *Journal of Catalysis*, vol. 287, pp. 37-43, 2012, doi: 10.1016/j.jcat.2011.11.015.
- [130] Z. Zhang, L. Li, and J. C. Yang, "Adhesion of Pt Nanoparticles Supported on gamma-Al<sub>2</sub>O<sub>3</sub> Single Crystal," *Journal of Physical Chemistry C*, vol. 117, no. 41, pp. 21407-21412, Oct 17 2013, doi: 10.1021/jp407798b.

- [131] Z. Zhang, L. Li, and J. C. Yang, "Adhesion of Pt Nanoparticles Supported on  $\gamma$ -Al<sub>2</sub>O<sub>3</sub> Single Crystal," vol. 117, no. 41, pp. 21407-21412, 2013, doi: 10.1021/jp407798b.
- [132] R.-S. Zhou and R. L. Snyder, "Structures and transformation mechanisms of the eta, gamma, and theta transitions aluminas," *Acta Cryst.*, vol. B47, pp. 617-630, 1991.
- [133] R. S. Zhou and R. L. Snyder, "Structures and transformation mechanisms of the eta, gamma and theta transition aluminas," *Acta Crystallogr. Sect. B-Struct. Commun.*, Article vol. 47, pp. 617-630, Oct 1991. [Online]. Available: <Go to ISI>://A1991GL01200006
- [134] *SRIM/TRIM*. (2003). <http://www.srim.org/>. [Online]. Available: <http://www.srim.org/>
- [135] J. F. Ziegler, M. D. Ziegler, and J. P. Biersack, "SRIM – The stopping and range of ions in matter (2010)," *Nuclear Instruments and Methods in Physics Research Section B: Beam Interactions with Materials and Atoms*, vol. 268, no. 11-12, pp. 1818-1823, 2010, doi: 10.1016/j.nimb.2010.02.091.
- [136] R. V. Zucker, D. Chatain, U. Dahmen, S. Hagege, and W. C. Carter, "New software tools for the calculation and display of isolated and attached interfacial-energy minimizing particle shapes," *Journal of Materials Science*, vol. 47, no. 24, pp. 8290-8302, Dec 2012, doi: 10.1007/s10853-012-6739-x.

**A. Appendix**

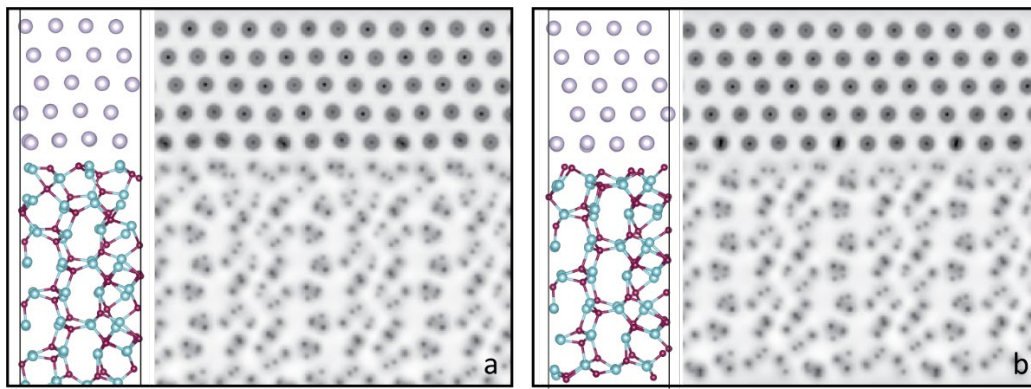


**Figure S1** DFT interfaces and BF image simulations of (a)  $Al_1$  (single Al-terminated) and  $\gamma$ -alumina (b)  $Al_2$  (double terminated)  $\gamma$ -alumina at the interface with Pt.